
Graduate Theses, Dissertations, and Problem Reports

2001

Optical gradation for crushed limestone aggregates

Ken Cheng
West Virginia University

Follow this and additional works at: <https://researchrepository.wvu.edu/etd>

Recommended Citation

Cheng, Ken, "Optical gradation for crushed limestone aggregates" (2001). *Graduate Theses, Dissertations, and Problem Reports*. 2318.

<https://researchrepository.wvu.edu/etd/2318>

This Dissertation is protected by copyright and/or related rights. It has been brought to you by the The Research Repository @ WVU with permission from the rights-holder(s). You are free to use this Dissertation in any way that is permitted by the copyright and related rights legislation that applies to your use. For other uses you must obtain permission from the rights-holder(s) directly, unless additional rights are indicated by a Creative Commons license in the record and/ or on the work itself. This Dissertation has been accepted for inclusion in WVU Graduate Theses, Dissertations, and Problem Reports collection by an authorized administrator of The Research Repository @ WVU. For more information, please contact researchrepository@mail.wvu.edu.

**Optical Gradation for Crushed
Limestone Aggregates**

Ken Cheng

Dissertation submitted to the
of
West Virginia University
in partial fulfillment of the requirements
for the degree of

Doctor of Philosophy
in
Mechanical Engineering

Larry E. Banta, Ph.D., Chair
John P. Zaniewski, , Ph.D.
Nigel Clark, Ph.D.
Mark Jerabek, Ph.D.
James Smith, Ph.D.

Department of Mechanical and Aerospace Engineering

Morgantown, West Virginia
2000

Keywords: Aggregates gradation, Machine vision, Image processing, Sieving, Limestone

ABSTRACT

Optical Gradation for Crushed Limestone Aggregates

Ken Cheng

The strength and durability of asphalt pavement is directly affected by the characteristics of its main ingredient, mineral aggregate. Besides material strength, research has shown that mixture properties such as particle shape and mixture gradation have a significant affect on the quality of the asphalt concrete. A standard called "Superpave" has been developed which sets forth specifications for material selection and methods for measurement of aggregate properties. These standards require monitoring of aggregate properties, particularly gradation. In this dissertation, the feasibility of developing an optically based method for determining aggregate gradation was explored. The physical system primarily consists of a standard monochrome CCD video camera and a computer with a frame grabber board. Software was developed to separate touching or overlapping particles in the image, and to detect the size and shape of each particle. Correlation to estimate each particle's mass and to predict the sieving behavior for crushed limestone aggregates was developed and tested. Laboratory testing demonstrated the ability to measure gradation over a range of particle sizes from 4.75 *mm* to 25 *mm* with an accuracy of ± 3 in terms of percent-passing residual when compared with mechanical sieving.

TABLE OF CONTENTS

TITLE PAGE	i
ABSTRACT	ii
TABLE OF CONTENT	iii
LIST OF FIGURES	vii
LIST OF TABLES	x
1. INTRODUCTION	1
1.1 Historical Background	1
1.2 Problem Identification	3
1.3 Research Objectives	4
1.4 What is Superpave	5
1.4.1 Aggregate Size	6
1.4.2 Aggregate Shape	8
2. LITERATURE REVIEW	9
2.1 Introduction	9
2.2 Existing Technology	9
2.3 Separation of Overlapping Image Objects	13
2.4 Particle Passage Probability in Sieving	14
2.5 Object Shape	15
2.6 Object Size	18
3. LABORATORY SET-UP AND MEASUREMENT CALIBRATION	20
3.1 Introduction	20
3.2 Hardware Set-up and Operating Condition	21
3.3 Image Acquisition	23
3.4 Image Measurement Calibration	25

3.4.1	Sample for Calibration	26
3.4.2	Finding Pixel Number	26
3.4.3	Area Correction	28
4.	IMAGE PROCESSING AND ANALYSIS	32
4.1	Introduction	32
4.2	General Description	33
4.3	Binary Image Conversion	36
4.4	Object Detection and Seeding	37
4.5	Edge Detection, Region Growing and Particle Projected Area	39
4.6	Centroid Location	41
4.7	Major and Minor Diameter Computation	46
4.8	Particle Shape Characterization	50
5.	SEPARATION OF TOUCHING AND OVERLAPPING PARTICLES.....	57
5.1	Introduction	57
5.2	Binary Erosion	57
5.3	Sequential Erosion	58
5.4	Separating Location	63
5.5	Detection of Saddle Point by Filtering	67
5.5.1	Filter Design	67
5.5.2	Saddle Point Conditions	69
5.6	Testing on a Real Image	72
6.	VOLUMETRIC MODELING	77
6.1	Introduction	77
6.2	Modeling Sample Preparation	77
6.3	Model Selection	81
6.4	Particle Geometric Assumptions and Definition	83
6.5	MLR Model Building	85
6.6	Overall Modeling Effect	89

6.7 Model Adequacy	92
6.7.1 The Coefficient of Multiple Determination	92
6.7.2 Error Normality	93
6.8 Model Testing	95
6.8.1 Preparation of Testing Sample Population	96
6.8.2 Testing Results	97
7. SIEVING CORRELATION	103
7.1 Introduction	103
7.2 Identified Sieving Problems	103
7.3 Analytical Discussion	105
7.4 Sieving Probability Analysis	109
7.5 Sieving Phase Analysis	112
7.5.1 Size Modification for Triangular Shapes	112
7.5.2 Sieve Series and Sieving Phase	114
7.6 Benchmark	119
7.7 Sieving Calibration Factor	123
7.8 Vision Sieving Result	125
8. SYSTEM PERFORMANCE	136
8.1 Introduction	136
8.2 Sample Preparation and Discussion	136
8.3 Sample Benchmark	140
8.4 Results Comparison	143
9. CONCLUSION AND FUTURE RESEARCH	146
9.1 Conclusion	146
9.2 Future Research	146

BIBLIOGRAPHY	149
APPENDIX I: Modeling Sample Statistics	154
APPENDIX II: Histogram of Model Testing Samples	162
APPENDIX III: Benchmark of Samples	171
APPENDIX IV: Images of Samples for Testing System Performance	175
VITA	179

TABLE OF FIGURES

Figure 1.1 : Aggregate	2
Figure 1.2 : Proportional Calipers	3
Figure 1.3 : Graphical Basis for 0.45 Power Chart	7
Figure 1.4 : Graphical Basis for Actual Size Chart	7
Figure 2.1 : Aggregate Size by Superpave	19
Figure 3.1 : Photo of Lab	21
Figure 3.2 : Lab Equipment Lay-out	22
Figure 3.3 : Image Capturing with Backlighting	24
Figure 3.4 : Image Acquisition and Processing System	25
Figure 3.5 : Samples for Calibration	26
Figure 3.6 : Maximum Pixel Number	27
Figure 3.7 : Data Curve Fitting	27
Figure 3.8 : Measured and Actual Area	28
Figure 3.9 : Curve Fitting for Measured Area	29
Figure 3.10: Improvement of Measured Area	30
Figure 3.11: Percent Error Improvement	31
Figure 4.1 : Simulated Particles with Centroid, Edge and Interior Points Labeled	33
Figure 4.2 : Shapes and Corresponding Signatures	35
Figure 4.3 : Binary Image Conversion	36
Figure 4.4 : Object Detected and Seeded	38
Figure 4.5 : Four Simulated Objects	39
Figure 4.6 : Sequence of Multi-object Detection and Seeding	39
Figure 4.7 : Region Growing	40
Figure 4.8 : Edge Traverse Recording	41
Figure 4.9 : Eight Particles Imaged	43
Figure 4.10: Centroid of Profile Shape	44
Figure 4.11: Aggregate Processing	46
Figure 4.12: Major and Minor Diameter	47
Figure 4.13: Major and Minor Diameter	50

Figure 4.14: Signature	51
Figure 4.15: Characterizing a Shape	52
Figure 4.16: Curve-fitting and Shape Characterization	56
Figure 5.1 : Typical Erosion as Shrinking	58
Figure 5.2 : Sequential Erosion	60
Figure 5.3 : Sequential Erosion on Simulated Image	61
Figure 5.4 : Saddle and Saddle Point	64
Figure 5.5 : Dissecting Plans for Finding Saddle Point	66
Figure 5.6 : Gray Level Attitude in Plan <i>A</i> and <i>B</i>	67
Figure 5.7 : A Filter of Size 5×5	68
Figure 5.8 : Rotation of a Filter	69
Figure 5.9 : Separation by Filtering	72
Figure 5.10: Separation Process	76
Figure 6.1 : Sample Photos	79
Figure 6.2 : Sample Data Observations	80
Figure 6.3 : Geometric Perspective of Particle	84
Figure 6.4 : Interpretation of Model Variables	87
Figure 6.5 : Data Transformation	88
Figure 6.6 : Volume Comparison	91
Figure 6.7 : Modeling Effect Observation	92
Figure 6.8 : Model Error vs. Particle Sequence	94
Figure 6.9 : Histogram of Standardized Residuals	95
Figure 6.10: Model Testing for Mass	98
Figure 6.11: A Random Combination of Sample Batches	100
Figure 6.12: Modeling Result for 100 Combinations	101
Figure 6.13: Percent Error for 100 Combinations	102
Figure 7.1 : Particle Cross Section Shape	104
Figure 7.2 : Particle Passing Mechanism	105
Figure 7.3 : Modeled Particle Cross Section	106
Figure 7.4 : Critical Position	107
Figure 7.5 : Scatter Diagram of Sample Flatness	109

Figure 7.6 : Sample Flatness Histogram	110
Figure 7.7 : Sample Flatness Distribution	111
Figure 7.8 : Triangle Shaped Particles	113
Figure 7.9 : Physical Sieve Cascade	115
Figure 7.10: Overview of Sieving Phase Analysis	116
Figure 7.11: Percent Retained and Percent Passing for Sample Batch #4	121
Figure 7.12: Mass Change in Sieving Process	122
Figure 7.13: Benchmark for Sample Batch #4	123
Figure 7.14: Benchmark for Combined Sample Batches	125
Figure 7.15: A Random Combination of Sample Batches	127
Figure 7.16: Sieving Correlation Testing #1	130
Figure 7.17: Sieving Correlation Testing #2	131
Figure 7.18: Sieving Correlation Testing #3	132
Figure 7.19: Sieving Correlation Testing #4	133
Figure 7.20: Sieving Correlation Testing #5	134
Figure 8.1 : Particles of Sample Group #2	137
Figure 8.2 : Histogram of Measured Diameter	138
Figure 8.3 : Histogram of Estimated Flatness	139
Figure 8.4 : Histogram of Estimated Volume	139
Figure 8.5 : Percent Retained Benchmark	141
Figure 8.6 : Percent Passing Benchmark	142
Figure 8.7 : Percent Retained Correlation	144
Figure 8.8 : Percent Passing Correlation	145

LIST OF TABLES

Table 3.1 : Operating Condition	23
Table 5.1 : Pseudocode of Sequential Erosion	62
Table 5.2 : Pseudocode of Separation	72
Table 6.1 : Sample Measurement Statistics	96
Table 7.1 : Pseudocode of Sieving Procedure	119
Table 7.2 : Benchmark Values for Combined Sample Batches	125
Table 7.3 : Testing Residuals	135
Table 8.1 : Statistics of the Benchmark (Sieving of 10 times)	142
Table 8.2 : Percent Retained Result Comparison	143
Table 8.3 : Percent Passing Result Comparison	144

1. INTRODUCTION

1.1 Historical Background

Hot-mix asphalt concrete is widely used to build modern highways. The strength and durability of asphalt concrete pavements are profoundly affected by the characteristics of the aggregates. Beyond the obvious dependence on aggregate's properties such as the strength and durability, characteristics such as particle shape, and gradation (i.e., size distribution) are extremely important. Research performed as part of the Strategic Highway Research Program provided a standard for asphalt concrete mix design called "Superpave" [1], which specifies limits for aggregate gradation, particle angularity, and percentage of thin and elongated particles.

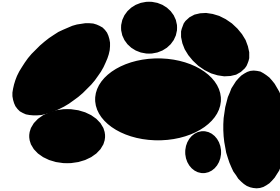
The particle size distribution in the mixed asphalt plays a vitally important role in the quality control for the highway building. For instance, pavements constructed with too high a percentage of fine particles such as natural sand will display unallowable levels of permanent deformation when loaded by traffic. On the other hand, too many large particles in the mixed asphalt can produce a large amount of voids. As a result, the strength and durability of the pavement will be compromised. The quality of pavement demands the appropriate mixture of various sizes of particles, and the size distribution of the mixture is presented by the gradation curve.

Particle shape is also important because rough or angular aggregates provide more strength than rounded, smooth-textured aggregates as shown in Fig. 1.1. Even though a jagged piece and a rounded piece of aggregate may possess the same material strength, angular aggregate particles tend to lock together resulting in a stronger mass of material. On the other hand, rounded aggregate particles tend to slide by each other. Flat and

elongated aggregates tend to break during handling, construction and under traffic load, changing the design gradation and compromising strength.



(a) Angular aggregates tend to lock



(b) Rounded aggregates tend to slide

Figure 1.1 Aggregate

Traditional methods for evaluating size, shape and texture of aggregates are time-consuming and labor intensive. Until very recently, some of aggregate evaluation for pavements was done manually. Individual coarse aggregate particles are visually examined to determine the number of fractured faces per particle. For determination of a particle's flatness and elongation, a proportional device is used, as illustrated in Fig. 1.2. The aggregate particle is first placed with its largest dimension between the swinging arm and fixed post at position *A*. The swinging arm is locked in position, the same aggregate is placed between the swinging arm and post at position *B*. If the aggregate passes this gap, then it is counted as a flat or elongated particle. Procedures such as these are time-consuming and are limited to a small sample sizes. There is no possibility of using these methods to provide real-time feedback for process control.

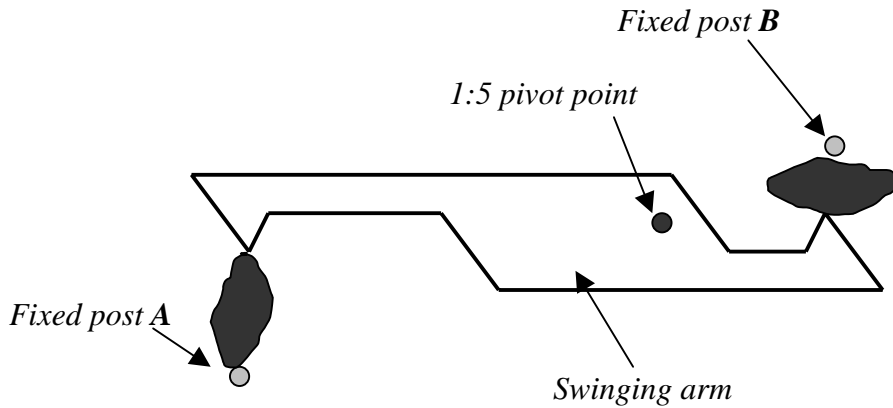


Figure 1.2 Proportional Calipers

Some of drawbacks existing in the traditional method can be overcome by taking advantage of modern machine vision techniques. It is believed that through processing and analyzing the aggregate images captured by machine vision system (a video camera, a frame grabber, and a PC), the size distribution, shape and angularity of aggregates can be determined. Instead of the mechanical sieving, “vision sieving” may be used to achieve results close to those obtained mechanically. Vision sieving offers two potential improvements over the traditional methods: reduced level of manual involvement and potential for automated gradation control.

1.2 Problem Identification

This work investigates the feasibility of using non-contact optical methods to provide information generally obtained by mechanical methods. Three particularly difficult problems arise within using machine vision for aggregate evaluation:

- 1) Particles are usually touching, overlapping, or even entirely occluded. Rapid discrimination of one particle from another is both necessary and difficult.

- 2) Standards for classifying particles by size are generally based on mechanical sieving and the process results depend on a combination of both size and 3-dimensional shape of particles. It is desirable to avoid the complexity and expense of explicitly measuring the 3rd dimension of each particle.
- 3) Sieving standards are also set up to report particle gradation on a “percent passing” basis, where the fraction is based on mass. So in addition to extrapolation of the interaction between a particle’s 2-D features and the sieving process, it is necessary to develop a means to extrapolate the relationship between a particle’s 2-D features and its volume. These extrapolations will be dependent on general size and shape properties that vary from particle to particle. For example spherical particles will have different sieving and volume transformation than cylindrical, cubic, or triangular particles.

The fundamental question is then, “Can we extract a set of features from the 2-D image which will provide adequate information to accurately predict volume characteristics, elongation, angularity, and the sieving behavior from the particles’ 2-D video image?”

1.3 Research Objectives

The work can be broken into three major tasks as follows:

- 1) To effectively describe the sieving characteristics of 3-D aggregates based on 2-D geometric size and shape of the particles.

- 2) To develop a functional relationship between a particle's plan features and its corresponding volume. In other words, inferring volume information of the 3-D particle under consideration by means of measurements obtained from 2-D image. This will be the main theme of this research.
- 3) To develop a simple and efficient method that can separate the touching and overlapping particles in the scene.

1.4 What is Superpave?

From 1987 through 1992, the Strategic Highway Research Program (SHRP) conducted a research effort to develop new ways to specify, test, and design asphalt materials. After 1992, the Federal Highway Administration (FHWA) assumed a leadership role in the implementation of SHRP research. An essential part of FHWA's implementation strategy was educating agency and industry personnel in the proper use and application of the final SHRP asphalt products, collectively referred to as Superpave [1].

Definitions for properties of aggregate such as size, shape and texture may vary from standard to standard, depending on the agencies involved. However, because this research is a project aimed at improving methods of aggregate gradation and shape identification, size, shape and other related definitions given in the Superpave guide book have become the guidelines in terms of comprehending the aggregate's characteristics.

1.4.1 Aggregate Size

Many technical reports in the field of mineral aggregate property studies explicitly or implicitly regard the area of the particle in a 2-D plane as particle size [3, 4, 5, 6]. In Superpave [1], the aggregate size is considered as being the dimension of a square sieve opening through which the particle falls by its own gravity. Let a sieve size be a square of $D_i \times D_i$, where D_i takes a discrete value of a sequence with $D_N > D_{N-1} > D_{N-2} \dots > D_1$. The aggregate size d is then a value that satisfies

$$D_{i-1} < d \leq D_i \quad (1.1)$$

Superpave prefers to use the 0.45 power gradation chart to define an allowable gradation limits. This chart uses a unique graphing technique to judge the cumulative particle size distribution of a blend of aggregates. The ordinate of the chart is percent passing, the abscissa is an arithmetic scale of sieve size in millimeters, raised to 0.45 power. Fig. 1.3 illustrates how the abscissa is scaled. In this example, the 4.75 mm sieve is plotted as 2.02 units to the right of the origin.

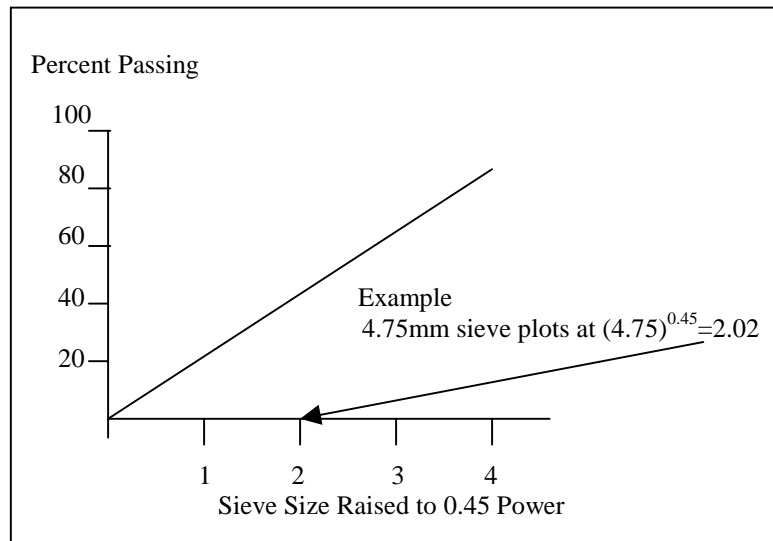


Figure 1.3 Graphical Basis for 0.45 Power Chart

For the sake of convenience, in this work an alternative way of construction of percent passing curve is used: the ordinate of the chart is still percent passing, but the abscissa indicates the actual sieve size in millimeters, as shown in Fig. 1.4.

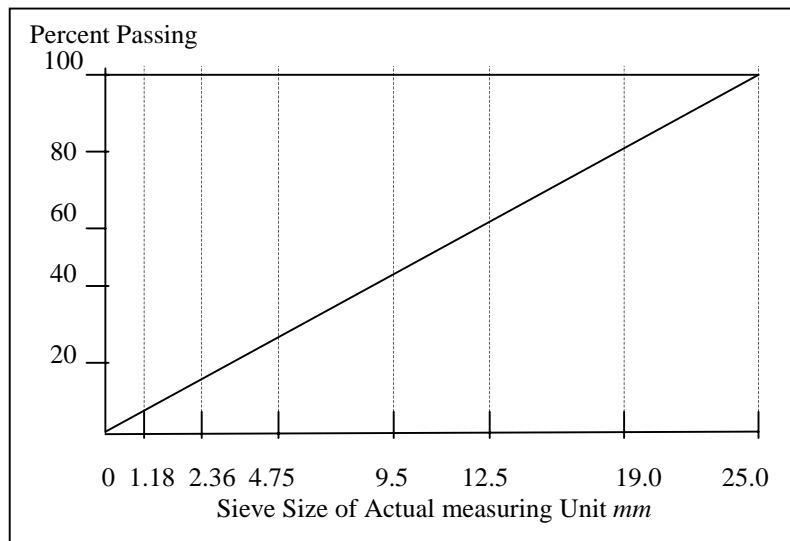


Figure 1.4 Graphical Basis for Actual Sieve Size Chart

1.4.2 Aggregate Shape

The Superpave manual [1] describes the particle shape as:

- Flat and elongated: The ratio of a maximum to minimum dimension is greater than 5.

The aspect ratio of the particle can be used for detection of elongated shape. Aspect ratio is defined as the ratio of the maximum diameter to the orthogonal minimum diameter of the shape silhouette.

In Superpave, shape identification is performed by obtaining the percentage by mass of coarse aggregates that are elongated. Elongated particles are undesirable because they have a tendency to break during construction and under traffic.

2. LITERATURE REVIEW

2.1 Introduction

This research is associated with many aspects in the fields of image processing, image analysis and statistics. Related work in image processing mainly involves image segmentation, more specifically, separation of touching and overlapping shapes, and object size and shape characterization. To optically “sieve” the particles, it needs to predict the particle mass based on 2-D image measurements.

There are many publications on image edge detection, image size and shape analysis. Many techniques in shape characterization such as Fourier analysis and template matching have been reported in literature. Some novel methods such as polygonal harmonics are also attracting attention. By comparison, fewer articles regarding separation of the touching and overlapping imaged shapes exist. There are some reports about inferring the objects’ 3-D information (volume) from their 2-D measurements. Some insights into optical sieving may be shared from the reports on existing technology, and several video graders using these technologies have been marketed commercially.

2.2 Existing Technology

In searching for the work related to this research project, only three commercial products that perform the functions desired for Superpave quality control were discovered. There are some helpful descriptions of these three commercially available systems given by H. Kim, *et al* [33].

The EMACO corporation of Montreal, Canada markets a device called the VDG 40TM, which uses optical methods to perform particle sieving. The VDG 40 employs a line-scan camera and approximates particle boundaries by drawing successive chords across the particles falling off the vibrating feeder. Although there has been some debate about its accuracy by some independent testers [32], this system is claimed to perform the following functions:

- Produce gradation curves for particles whose sizes range from 1 to 50 *mm*.
- Calculate mean elongation coefficient.
- Estimate the “flattening coefficient”.
- Uncertainty less than 1.7% for samples with enough particles in each class.

Based upon the assumption that the thickness of the particle is the same as its width, the volume is computed using an ellipsoid of revolution [32]. No clear information about how to separate the touching and overlapping is provided even though the falling particles may be overlapped when viewed in any direction. A description of the on-going effort on testing and improving VDG 40 is summarized by R.L. Weingart, *et al* [31].

Several products are marketed by the WipWare Company in Bonfield, Ontario, Canada [35, 39]. WipFragTM performs optical gradation on bulk materials on the ground or on moving conveyor belts. The WipFrag system is based on area scan video cameras. Some case studies using the Wipfrag image analysis system were presented by Maerz [40]. Another product, WipShape, uses a conveyor and two video cameras to image one particle at a time and compute the percentage of flat, elongated particles [35, 37].

N.H. Maerz used stereology and object geometric probability to explore the possible solution of the problem of inferring the true size distribution of a body of particles, given the observed profile distribution on an imaged scene [27]. The process is known in stereology as “unfolding” a distribution. The problem is: can one reconstruct a block size distribution of a pile of blast fragmented rock from a measurement made on the surface of that pile? Maerz found that if one applies the stereological theory developed by previous researchers to this problem, many of the assumptions made for the existing theory are violated. Therefore, Maerz suggested a new method of unfolding the distribution.

This new method is based on analyzing fragmentation using image analysis, and first assuming all particles to be spherical for a quick solution. The distribution from the image can be calculated. Maerz states that the observed distribution should be further divided into a number of classes, in each of which the particles have a similar diameter. A calibration function was added to account for numerous effects to improve algorithm’s accuracy. This makes the equation become “semi-empirical”. The calibration function is determined by back calculation from a known size distribution.

An experimental system is under development by Rao, *et al* at the University of Illinois [32]. Rao developed an experimental device that uses three cameras to capture orthogonal images of a single particle at a time. Rao’s objective is to improve the detection of flat, elongated particles, and it was claimed that the system performs more accurately than either the VDG 40 or the WipFrag system [32]. The tests have demonstrated volume measurement errors ranging from 5% to more than 10%, but errors in detection of flat, elongated particles were within approximately 1-2%. Rao’s device is

quite slow, however. A processing time for 1037 particles of 70 minutes was reported. The volume errors are also relatively high ($\approx 10\%$) when compared with the published claims of commercially available systems [31].

The method of calculating aggregate volume is straight forward. Three video cameras are mounted from three orthogonal directions: front, side, and top. The images acquired from these three views provide some capability to reconstruct the 3-D shape of the particle needed for volume computation. The particle is confined in the smallest box whose sides are found to be the smallest rectangle that includes the particle projected area in that viewing direction. Those pixels, called *solid pixels*, can be found readily which belong to the particle body from all three viewing directions. All the cubes made up of the solid pixel are summed up, and calibrated to cubic millimeters. Hence, the volume of the particle under study is obtained. However, it is fairly easy to envision shapes for which even three orthogonal views are taken would not be sufficient to accurately evaluate particle volume [33]. The particle touching and overlapping problem is avoided because all particles fall one at a time onto a belt that is in motion. Though the system performance is expected to give improved accuracy, it is more time consuming since the particle is processed individually on a conveying belt.

The Micrometrics Corporation sells a device similar in design to the VDG 40. The Optisizer PSDATM uses a vibrating feeder and a CCD camera to capture a 2-D image of particles from 40 micrometers to “greater than 10 *mm*” [36]. This device is more suited to pharmaceutical environments than construction work, however. No mention of particle shape analysis is provided, nor are statistics on the sieving accuracy of the machine.

In addition to these devices, articles related to optical sieving or particle size and shape evaluation have been published in the technical literature by a variety of authors. Parkin, *et al* published a proposal for a laser based aggregate scanning device in 1995, but no further references to their system have been found [4].

2.3 Separation of Overlapping Image Objects

Bennamoun and Bouashash [3] introduced a segmentation method based on the successful completion of robust edge detection. The segmentation algorithm begins with extracting the *convex dominant points* (CDP), then use these CDP's for the part segmentation by simultaneously moving each of them normal to the edge contour until one CDP touches another point. Next the initial locations of CDP's are joined to the touched points. This process is repeated until the whole object has been segmented into constituent parts. The segmented parts are then isolated and modeled by superquadratics with varying parameters for recognition purposes.

A templating approach for separating the touching and overlapping spots is introduced by Noordmans and Smeulders [14]. The technique consists of two phases: detection phase and characterization phase. In the detection phase, all image positions are matched to a spot model with predefined parameter vector and coordinate. The optimal match is given by the specific value of parameter vector that results in a minimal match error. Following the detection phase is the characterization phase. The primary purpose of this phase is to further reduce the match error. Detecting two overlapping spots is based first on the observation of two major match errors, then extracting the local image. After removing one neighboring spot, the first spot is optimally matched with the

model using numerical minimization procedure. By the same method, the second spot can be detected and characterized. This way, two overlapping spots are thus detected and characterized independently.

In morphological image processing, the *watershed* detection approach proves to be an efficient way of segmenting gray scale images or binary images. Vincent [28] provides a faster, more efficient algorithm than those introduced previously to detect the watershed for a gray toned image. The basic principle behind this technique is that the whole gray scale image under study is considered as a *topographic surface*. This surface is made up of basins (valleys) and mountains. The watershed algorithm computes the dividing lines between the different “catchment basins”, which become regions or objects in the image. In the case of a binary image, the effect is to separate touching or overlapping particles. A modification of this approach was developed for use in this research.

2.4 Particle Passage Probability in Sieving

Most probabilistic studies of particle-passage through a sieve relate the probability of passage to sieve aperture size and particle shape. Bocoum [41] reviewed some probability theory in sieving. In summary, the particle-passing probability through a screen depends on the following aspects:

- 1) Three dimensional shape of the screen, and
- 2) Its relative size to the size of the particle
- 3) The percentage of open area on the screen surface.
- 4) Screen surface roughness.

5) The speed of the particle upon impact.

The primary studies of particle-passing probability were developed for particles of three geometric shapes: spheres, ellipsoids, and cylinders. For these three shapes, the theoretic passing probability was reviewed in Bocoum's paper. However, no conclusive information was presented for the irregularly shaped particles passing through the square sieve aperture.

2.5 Object Shape

Particle shape is an important factor in particle handling and product quality control. Since the particle shape influences how particles flow, react, sinter, break, agglomerate, and fluidize, numerous shape characterization techniques have been demonstrated over the last decades [8].

Particle shape analysis can be divided into two broad categories: behavior analysis and image analysis [9]. Most image analysis techniques rely on examining a two-dimensional image silhouette of the particle shape. Analysis of particle image can be conducted in either a microscopic or macroscopic manner. The microscopic method is used to describe the particle's relatively subtle change on the surface such as angularity and roughness. The macroscopic method, on the other hand, is more general in the sense of describing particle shape. This approach usually provides information in 2-D image about particle characterized shape such as triangle, four-sided, etc.

In a microscopic shape study, Clark made some explorations of fractal analysis [7]. Fractal analysis originates from the fact that the perimeter of the silhouette edge is dependent on the step length with which it is measured. The small detailed features on

edge can be taken into account with step length small enough, while taking large step length will ignore some delicate characteristics of the edge. The measured perimeter is increased if the step length used is decreased, yielding the notion of “fractal dimension” that can be used to describe particle ruggedness over a range of scale. A logarithmic plot of perimeter against step length produces a curve with negative slope. Steepness of the curve slope is used as a descriptor indicating the extent of the ruggedness of that particle silhouette. Fractal dimension shows the general degree of particle ruggedness, but does not provide general geometric shape information.

In a more macroscopic approach, Clark, and Reilly introduced a novel approach called *polygonal harmonics* to describe the particle shape [9, 10]. A starting point is selected on the edge of the particle, then a pair of dividers is set at some distance and used to find another point on the curve. Sequential points on the edge are found in the same manner by marching along the edge of the particle. The procedure is similar in this regard to a structured walk to find fractal dimension as mentioned previously. The walk continues past the first starting point, traversing the silhouette edge over and over again. Eventually a polygon is formed with a fixed dividing step length within the shape. Different step lengths produce different polygons for the same particle shape. Harmonic persistence is defined as the ratio of the largest step length to the smallest step length yielding that particular polygon. High harmonic persistence is an indicator of general particle shape.

This approach has shown some satisfactory results. However, in general it does not guarantee that a particular polygon exists for a given shape silhouette. Repetition of computation using different step lengths to find harmonics persistence is needed for each

particle [10]. Moreover, the persistences are not unique to each analytical shape, nor can the shape be reconstructed using the persistences [12].

Fitting approaches have been found in a variety of literature. In the papers by Bennamoun and Bosshash [3], Rosin and West [6], object shapes are described by fitting the object edge silhouette with superellipses. Each superellipse is described by three parameters: major and minor axis, and shape factor. One superellipse can be found to be the best fit to the shape in question by minimizing the Eucidean distance between the point on the superellipse and the point on the edge silhouette. Using the three identified parameters of this particular superellipse, the shape can thus described. The advantage of this technique is that a superellipse can represent a wide variety of shapes. with a small number of parameters.

Another template matching is to fit the object edge silhouette with a square instead of a superellipse. The side length of the square is used as the descriptor for the shape to show how square-like or rhombic-like that particle is. The best fitting square is found by minimizing the area error between the square and the particle of interest. The merit of this technique is that only a few parameters are necessary for describing the shape in question. However, neither the superellipse nor the square fitting approach can accurately represent shapes with odd numbers of sides. For instance, a triangle shaped particle can never be fitted well by either the superellipse or square. Moreover, both techniques are computationally intensive. Algorithm convergence is not always guaranteed. This disadvantage is even more severe when applied to a large number of particles in a single image.

A set of descriptors called “invariant moments” was studied [2]. Invariant moments are derived using the central moments of the image shape. Because of the relation of central moments with the regular moments, and the uniqueness of these regular moments relating to a certain image function, the chance that different shapes have the same or even close invariant moments is small. Therefore, invariant moments can be utilized to describe the shape features.

All the above shape descriptors share the same merit: they are translation-invariant, rotation-invariant, and scale change invariant. These attributes are necessary for shape feature classification in a multi-object situation. The negative aspect about using the above techniques is the computational intensity.

Fourier analysis has long successfully employed on smooth, rounded particles. In Fourier analysis, the edge is described by expressing the radius from the centroid of the shape as a function of the swept angle, using a Fourier series. For instance, the second coefficient gives an implication of aspect ratio, and the third coefficient indicates triangularity, and so on. Particle shapes can be compared in a n-dimensional space composed of the n orthogonal Fourier coefficients [13]. The well-known weakness of Fourier analysis lies in the fact that it does not deal efficiently with highly reentrant shapes.

2.6 Object Size

Size and shape issues are usually intertwined in image processing problems. Various specifications for object size description have been found in technical reports: for objects of regular shapes such as squares and circles, side length and diameter are used

respectively to define sizes. For irregularly shaped objects, major and minor dimensions are well-defined measures, although they do not guarantee uniqueness of shape description. Size, defined by the object's projected area, can be found explicitly and implicitly described in various papers. In Rosin and West [6], it can be inferred that the size is defined by the parameters of the superellipses, and is also represented by its area.

Size definition is problem-oriented. In the Superpave manual [1], the size of aggregate is measured by its sieve size. Fig. 2.1 illustrates how a particle's minor diameter corresponds to the square sieve opening size.

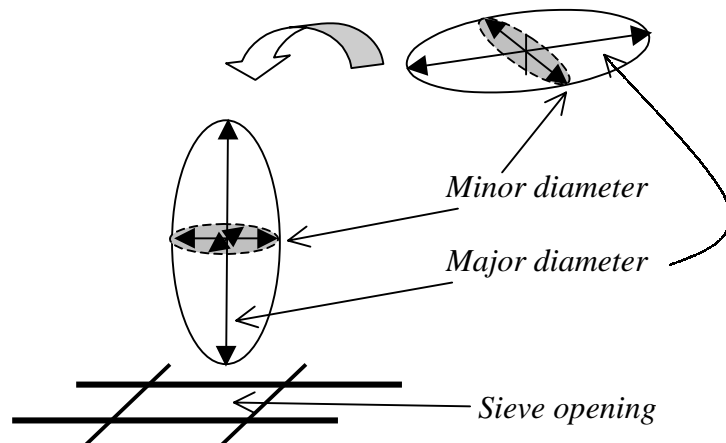


Figure 2.1 Aggregate Size by Superpave

The correlation between a particle's minor diameter and the sieve opening size is rather complex, sensitive to the actual size, particle shape, surface roughness, orientation and the interaction with all the touching particles at the moment it is about to pass the opening, and very sensitive to the amplitude and waveform of vibration. It becomes more complicated to quantitatively analyze and simulate the mechanical sieving process.

3. LABORATORY SET-UP AND MEASUREMENT CALIBRATION

3.1 Introduction

A video camera translates light levels focused on the image plane into electronic signals which can be transmitted and reproduced on a monitor set. The most common type of video camera uses a charge coupled device (CCD) chip to translate the light into electrical signals. The CCD chip is actually a grid of tiny individual light measuring devices which break the scene up into individual picture elements, or pixels. The camera used for this research breaks each scene into an array of 512 pixels wide and 484 pixels high.

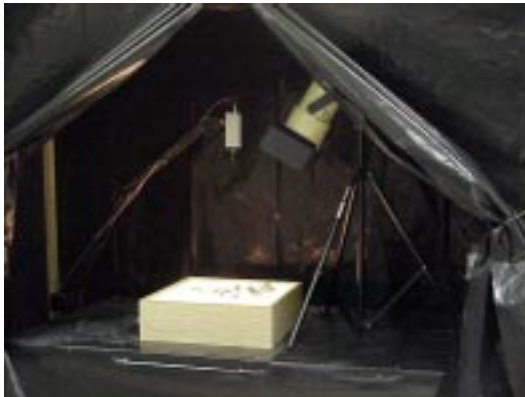
To process these signals using a computer, the light level represented by the video signal must be digitized by translating the signals into a series of numbers that the computer can manipulate. This is implemented by a frame grabber board, which performs very fast analog-to-digital conversion on the electronic signal for the camera. As a result, a grid (matrix) of numbers ranging from 0 to 255, with one number for each pixel, is formed. Low numbers represent dark parts of the image and high numbers represent bright parts of the image.

To optically sieve the particles, it is necessary to translate the pixel measurements into standard dimensions of millimeters. Pixels are in general not square, and so a unit of one pixel represents a different length in the x direction than it does in the y direction. In addition, the object is projected optically onto a CCD array. This causes the size of the image to depend not only on the size of the object but also on its distance from the camera, and on the focal length of the lens used to project the image onto the CCD

sensor. Therefore, a scale of $mm / pixel$ needs to be determined before any useful image analysis takes place.

3.2 Hardware Set-up and Operating Condition

The laboratory consists of a video camera housed in a curtained enclosure to allow control of the lighting conditions, a computer with a frame grabber card, a box with translucent cover to backlight the aggregates, and miscellaneous equipment for scene illumination, positioning the camera, measuring the light level, etc. The photo in Fig. 3.1 demonstrates the actual lay-out of the hardware components. The interior of the wall was painted black to reduce light reflection. All the components involved are numbered and illustrated in Fig. 3.2. Other associated devices, such as mechanical sieves, laboratory balance, were used in the Asphalt Pavement Laboratory in the Civil and Environment Engineering Department at West Virginia University.

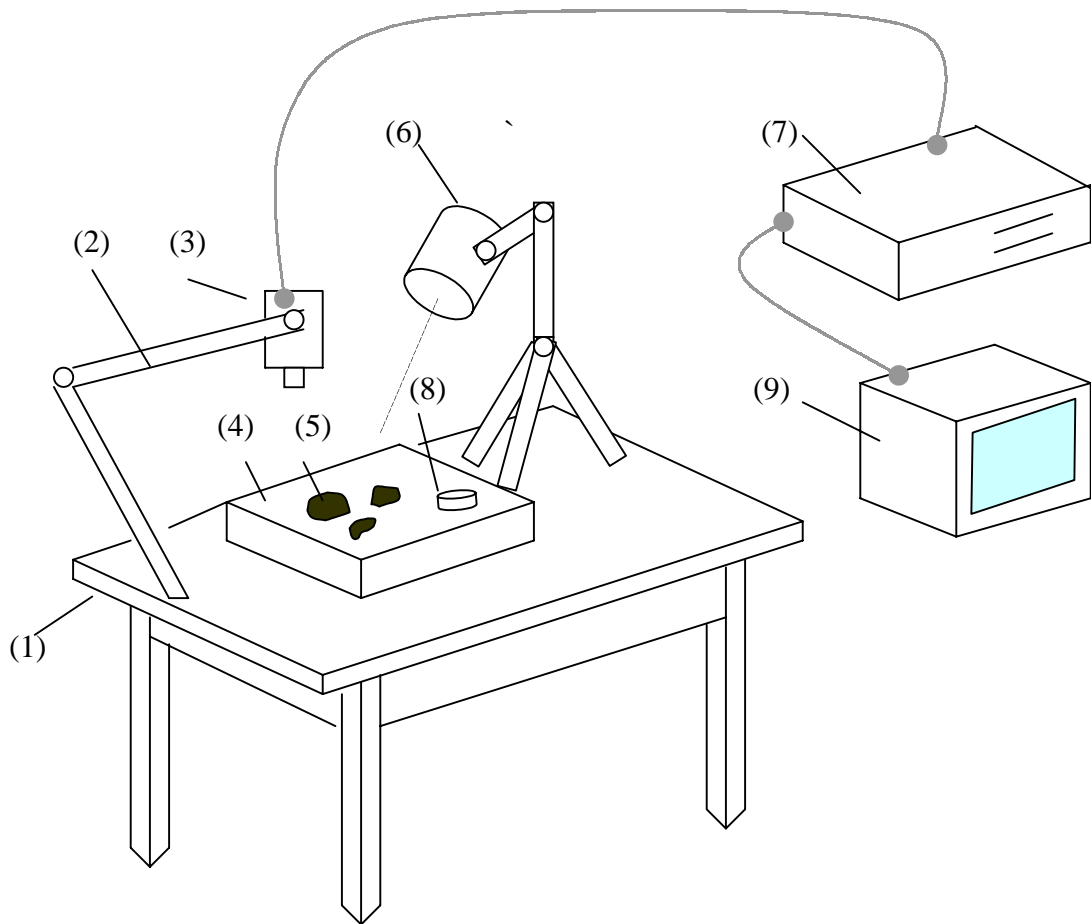


(a) Image capturing set



(b) Image processing set

Figure 3.1 Photo of Lab



3.2 Lab Equipment Lay-out

Referring to Fig. 3.2, the representation of the numbered item is as follows:

- (1) Stationary table.
- (2) Pan-tilt device with 6-degrees of freedom.
- (3) Video camera.
- (4) High contrast lighting box.
- (5) Aggregate particles.
- (6) Photographic strobe light for oblique lighting.

- (7) Personal computer with frame grabber.
- (8) Light intensity meter.
- (9) Monitor.

The operating specifications for image capturing using the lighting box are given in the table below:

Table 3.1 Operating Condition

Camera Distance from background	20 inches	Camera aperture	6
Camera Focus	20 inches	Ambient lighting intensity	12 LUX
Camera Shutter speed	1/125 Sec		

3.3 Image Acquisition

In order to properly “sieve” the aggregates, it is necessary to distinguish one particle from another in the video image. The gray scale video images that are most commonly seen, seem simple to the human observer to see where object boundaries are, while the information presented to the computer from these images is nothing more than a large grid of numbers. To detect these boundaries, most approaches involve some sort of gradient detection - looking for places in the image where there are rapid changes from light to dark or vice versa. Some of the object boundaries are clearly defined by contrast between the background and the existence of object shadows. But if imaged objects such as mineral particles overlap, the contrast between two particles may not be so distinct. In addition, the existence of ridges or corners on the particles can produce high-contrast edges which are not true particle boundaries in the 2-D sense.

Various edge-finding algorithms and lighting angles were explored to find a method that would reliably detect the boundary of each particle. The simplest and most common edge detectors are first-order high-pass filters based on the Sobel Operator or variants thereof [2]. These filters are highly sensitive to noise and directional in nature, performing best on edges that are either vertical or horizontal. Sobel filters combined with top lighting are also prone to including unwanted edges, such as those resulting from corners or shadows on the top surface of the particle.

To eliminate interior edges, a small light table was constructed for backlighting the aggregates. This lighting method produces extremely high contrast images with well-defined edges. In the phase of obtaining image data, objects are backlit to obtain sharply distinctive edges from black images on a white background, as illustrated in Fig. 3.3. Once the image has been captured under the operating conditions specified previously, each image is stored as a set of x - y points. Image processing and analysis are performed on these sets.

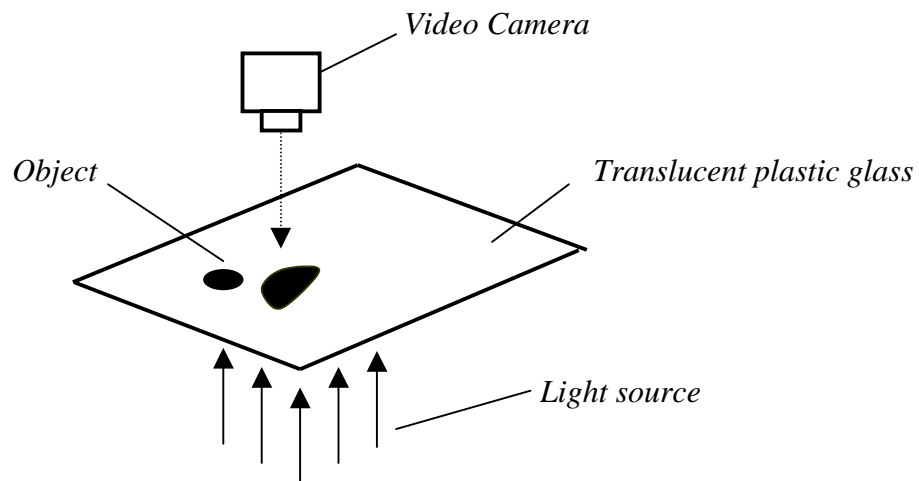


Figure 3.3 Image Capturing with Backlighting

Fig. 3.4 illustrates the procedure related to image analysis and processing..

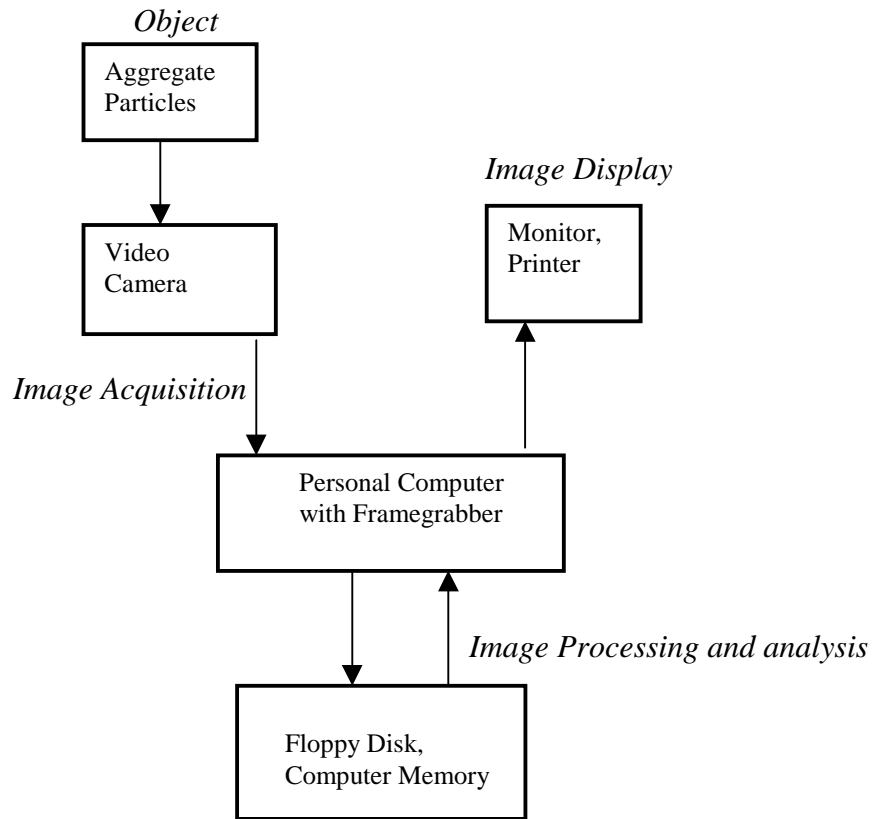


Figure 3.4 Image Acquisition and Processing System

3.4 Image Measurement Calibration

The measuring unit for the image is the number of pixels. For example, the image area for a given particle might be 100 pixels, and the circumference length might be 50 pixels, etc. The actual measuring unit is millimeters, thus a conversion from pixels to millimeters is required. In other words, the scale of *mm/pixel* needs being determined.

3.4.1 Sample for Calibration

Three types of sample circles were found using penny, nickel, and quarter. Their diameters are 19.05mm, 21.12 mm, 24.20 mm, respectively. The corresponding areas are 285.02 mm², 350.33 mm², and 459.96 mm². The distance between the camera and the imaging background is 20 inches, set constant for all images. The parameters of the camera such as shutter speed and aperture were unchanged during the imaging process. Fig. 3.5 shows the samples used for calibration.

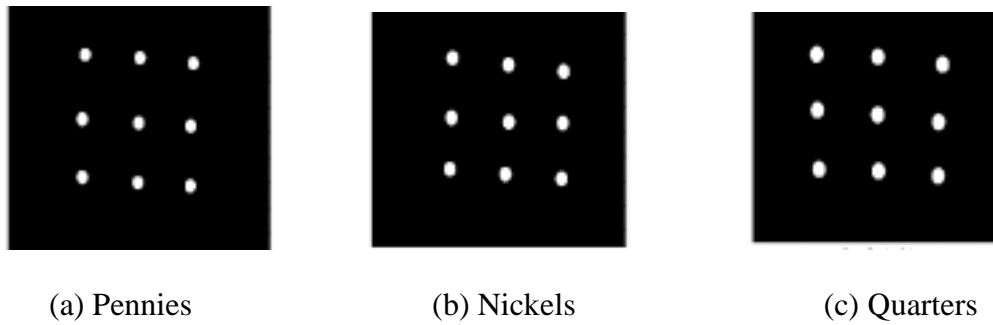


Figure 3.5 Samples for Calibration

3.4.2 Finding Pixel Number

Fig. 3.6 shows the pixel number for the diameter of the three sample circles. Note that the horizontal and vertical numbers are different. They are obtained by scanning the image in two orthogonal directions. Note also that although 9 coins are used for each type of circle, the plot shows that some resultant pixel numbers are coincident with each other.

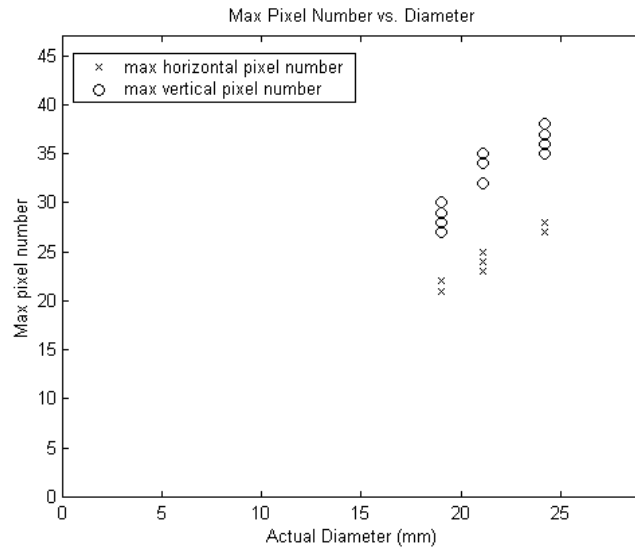


Figure 3.6 Maximum Pixel Number

Using least squares curve fitting, both the horizontal and vertical pixel data points can be fitted with a straight line, which is forced to go through the origin. Fig. 3.7 illustrates the result.

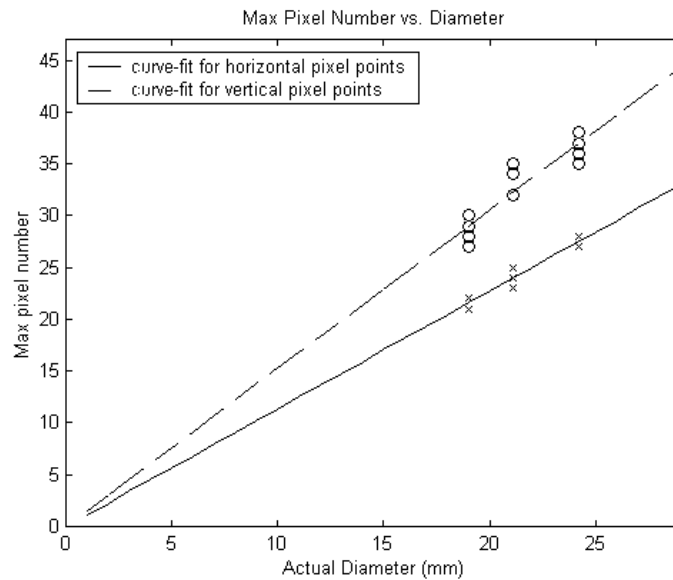


Figure 3.7 Data Curve Fitting

The reciprocal of the slope of each straight line is taken as the desired scaling factor of $mm / pixel$. The results are: $0.8802 mm/pixel$ in the horizontal direction, and $0.6551 mm/pixel$ in the vertical direction.

3.4.3 Area Correction

Prior to calibration, the object area is measured in number of pixels. Using the scale factors obtained previously, the measured area in terms of square millimeters can be acquired. Fig. 3.8 shows the plot of the findings against the corresponding actual areas.

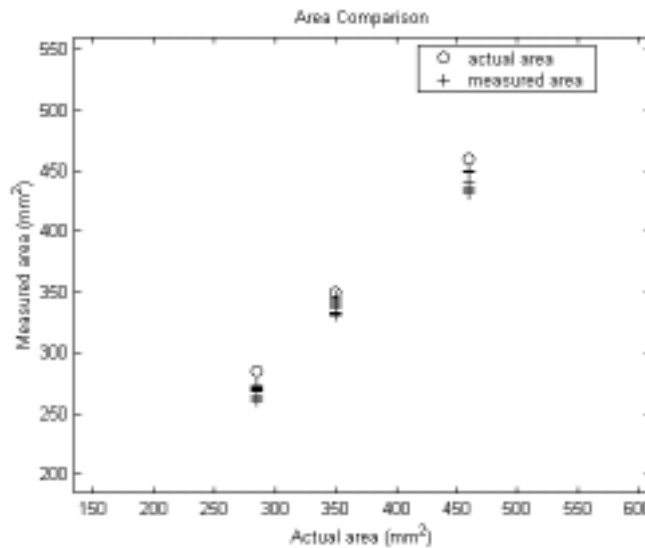


Figure 3.8 Measured and Actual Area

The measured area data points are curve fitted by a straight line using least square method, as shown in Fig. 3.9. Note that the value on the abscissa is actual area, and this leads to the relation between the actual area and the measured area. This function was found to be

$$A_t = \frac{(A_m + 7.9335)}{0.9742} \quad (3.1)$$

Where

A_t : actual area (mm^2).

A_m : measured area (mm^2).

The above transformation is necessary because there are “dead areas” in the image between pixels, so simply multiplying the two scaling factors leads to incorrect results.

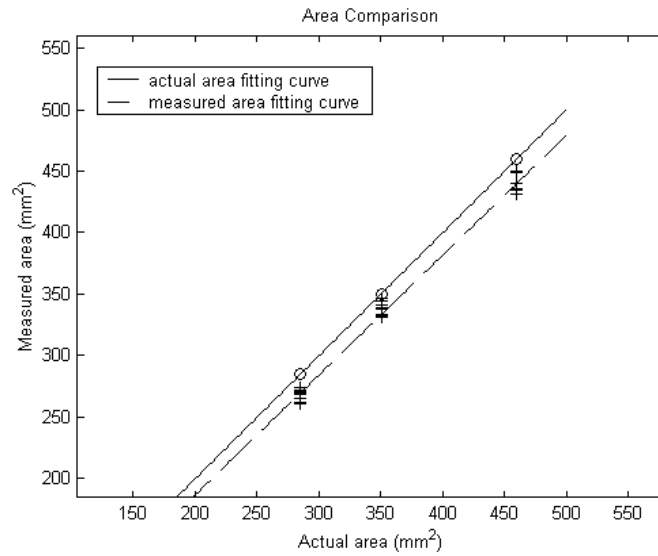


Figure 3.9 Curve Fitting for Measured Area

As illustrated in Fig. 3.10, the measured areas are much closer to the corresponding actual areas. As a result, the accuracy of the measured areas is improved.

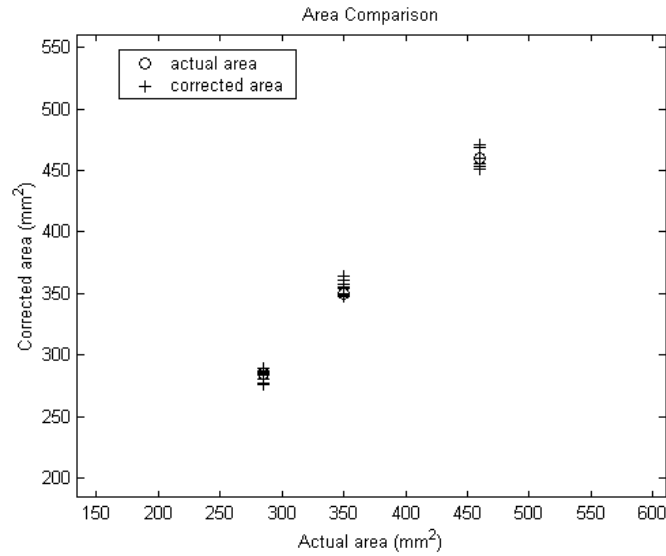
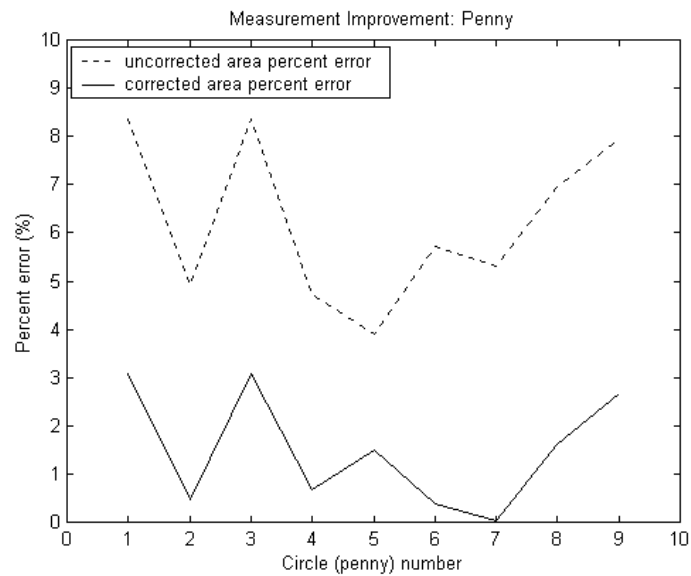
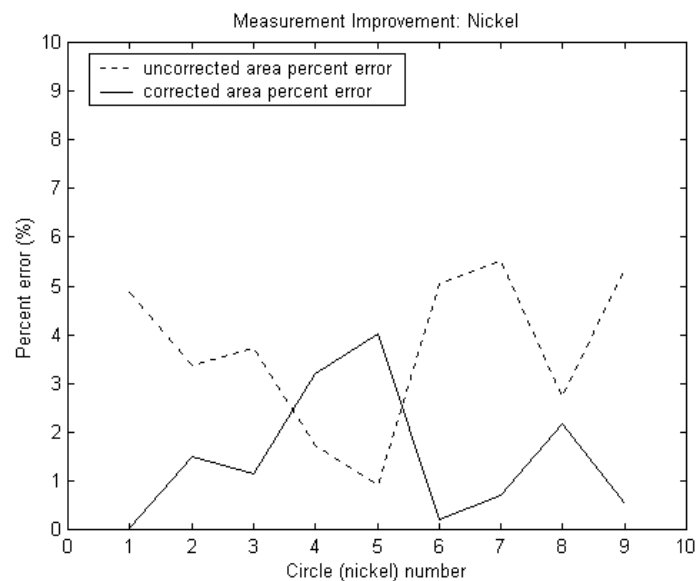


Figure 3.10 Improvement of Measured Area

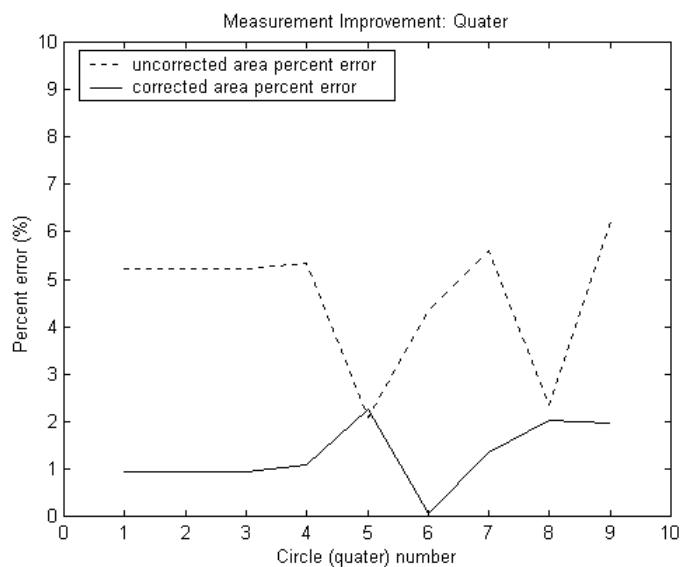
The improvement in the measured areas can be demonstrated by observing their absolute percent error before and after using Eqn. (3.1). The absolute percent error for three circle samples are shown in Fig. 3.11.



(a) absolute percent error for pennies



(b) absolute percent error for nickels



(c) absolute percent error for quarters

Figure 3.11 Absolute Percent Error Improvement

4. IMAGE PROCESSING AND ANALYSIS

4.1 Introduction

For each imaged object, that is, a non-touching-overlapping particle, the size and shape as well as some other parameters must be computed for the particle volume estimation and optical sieving purposes. Based upon the binary images – all particles are white and background is black, the area, size, shape, and some other related statistics are calculated. Image preprocessing includes binary conversion, edge detection, and separation of the touching and overlapping particle shapes. By image analysis herein, it means finding the particle shape centroid, area, major and minor diameters, identifying shapes, and computing all the needed statistics of the particle in question.

Solution for finding above measurements is summarized in actual research sequence as follows:

- 1) Binary image conversion.
- 2) Image capturing and seeding
- 3) Edge detection, region growing and particle projected area calculation.
- 4) Centroid location.
- 5) Major and minor diameter computation.
- 6) Particle profile shape characterization.

Successful completion of the image preprocessing and analysis paves the way to establishing a mathematical model to estimate the volume of particle, and ultimately, to obtain the particle size distribution through a sieving correlation process.

4.2 General Description

Fig. 4.1 shows images of four simulated particles. Sub-figure (a) simulates the binary image that is the result of image processing, while (b) shows the completion of the analysis to it. Once the particles have been converted to binary images and separated, analysis starts with horizontal scanning and tracking the edge of each particle. During the edge following, edge points (or pixels) are stored in an ordered list, and the interior points are counted to compute the projected area of the particle. Calibrated scaling factors are used to transform pixel numbers into dimensional measurements. The centroid of the particle is calculated during the scanning process, and the pixels belonging to the particle under consideration are labeled so they can be eliminated from future scans.

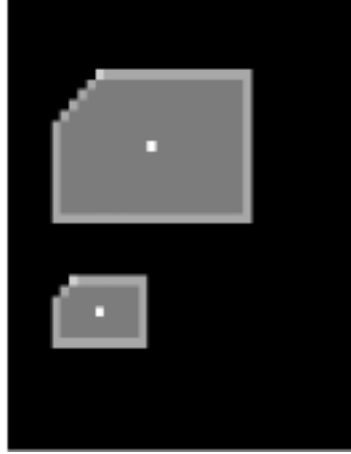


Figure 4.1 Simulated Particles with Centroid, Edges and Interior Points Labeled

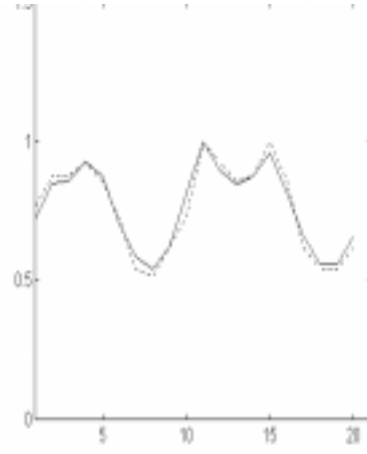
Once this process is done, the list of edge points is sampled and the Euclidean distance from the centroid to each of the edge points is computed. Because particle sizes vary significantly, the sampling algorithm may be set up to choose an adequate number of points from the edge to yield a good description of the particle silhouette in order to

minimize the amount of computation required per particle. In this research, each edge point is sampled. This sampling method results in samples at uneven intervals of the polar angle θ from the centroid, but avoids the time-consuming search for points satisfying the angle interval criterion and the repeated calculation of the inverse tangent function.

To characterize the particle's profile shape, the "edge signature" is constructed. A signature gives the distance between each edge point and the centroid, or, the radius at each edge point, so the information about the particle's shape can be stored in the signature function. To eliminate the noise, the signature function is fitted by a polynomial. Since the order of the polynomial is lower than the number of signature points, significant smoothing of the curve occurs, yet the polynomial is complex enough to track even relatively jagged particle boundaries accurately. The maxima and minima of the polynomial can be computed, as can the sum of squared errors between the actual signature points and the fitted curve. In general, maxima of the polynomial correspond to the vertices of the particle, and the "significant" minima are often created by flat faces, as demonstrated in Fig. 4.2.



(a) two similar shapes



(b) normalized signatures

Figure 4.2 Shapes and Corresponding Signatures

One important further use of the edge points is made. To correlate particle size to sieve size, it is critical to measure a particle's dimension. For spherical particles the correlation is easy, but for crushed aggregates it becomes very difficult. The solution is to compute a covariance matrix from the edge points, and then to use the two eigenvectors of that matrix to compute the “major” and “minor” diameters of the particle. These dimensions are usually close to but not always coincident with the actual maximum and minimum dimensions of the particle shape. Major and minor diameters are used to compute the elongation of a particle. Note that the relationship between actual particle dimension and sieve size is very complex, involving quantization effects and sensitivity to particle shape and orientation. In this work, the minor diameter is used to correlate the sieve size.

4.3 Binary Image Conversion

Edge detection can be carried out much more easily on a binary image than a gray scaled one. Computations involved in finding particle projected area, locating the centroid, characterizing profile shape are all originated from edge detection.

A high contrast image can be obtained using the backlighting box to silhouette aggregates spread on its surface. In Fig. 4.3 (a), two pieces of aggregate were placed in the scene and digitized on a 484x512 image matrix. Note that the shadow is present because backlighting is not used. To make the problem clear and simple, the two rocks were separated. Fig. 4.3 (b) shows the image captured using the backlighting box. In order to efficiently extract geometric information from the image, thresholding is taken to reduce unnecessary gray-scale variation, thus a binary image is obtained, as depicted in Fig. 4.3 (c) and (d).

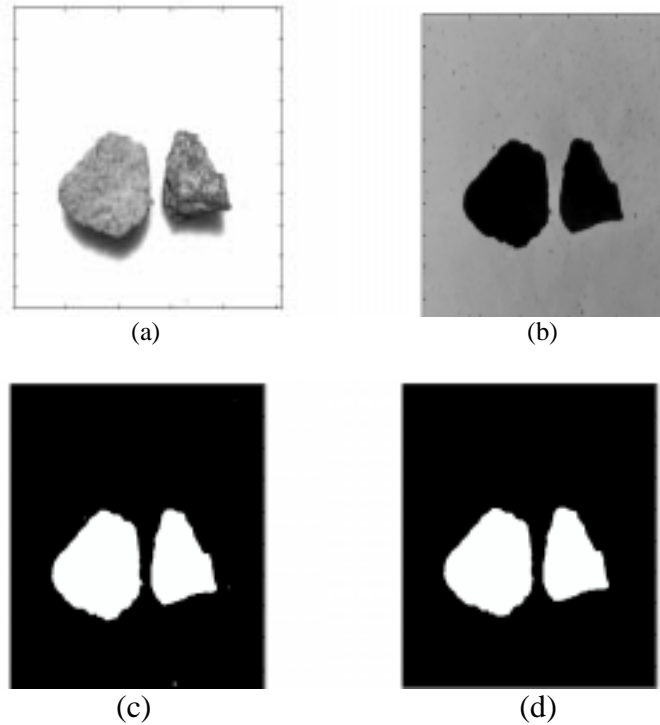


Figure 4.3 Binary Image Conversion

Fig. (a): Image captured without using lighting box. Particle edges can be difficult to distinguish from shadows.

Fig. (b): Image captured using lighting box. Conversion to binary image is carried out on this image.

Fig. (c) (d): binary image obtained, before and after removal of small speckle noise. The speckle noises can be caused by both insignificant tiny particles and unclean camera lens. Checking the spot size experimentally can remove them.

4.3 Object Detection and Seeding

The whole object detection and seeding procedure is featured by “piecewise” processing in terms of particle number order. The object of interest is processed by the algorithm designed for acquiring all the needed measurements.

Particle detection is performed by taking advantage of horizontal scanning over the binary image. An object is detected when the first edge point belonging to that specific object is encountered by the scan moving point (SMP), which is travelling horizontally from left to right within the object. This first encountered point works also as a seeding point, or simply seed. A seed is always located at the top-most-then-left-most (TMLM) position on the detected Object. Object detection and seeding is completed simultaneously. The seed is used as the starting point from which the region growing will take place. In Fig. 4.4, the brightest point on the object indicates that the object is detected and seeded. Note that for demonstration purposes, the image presented here is not a binary one, but rather an intensity one with gray scale 64. This is for

showing up the seed location. In fact, pixel labeling is imbedded throughout the algorithm for various processing purposes.



Figure 4.4 Object Detected and Seeded

In the multi-object case, an object whose TMLM edge point is also in the top-most and left-most position in the image matrix, will be detected and seeded first, since the SMP is traveling rightward, and the scan line is moving downward. Once the object's last pixel has been encountered by SMP, this object is isolated from all other objects, processed and would-be-processed alike, in order to avoid being re-encountered by the SMP. The detail about isolation is given in the later section. The processed object can also be considered as having been converted to the background, and it will be ignored by the SMP. The next candidate object to be detected and seeded is the one whose TMLM edge point satisfies the position conditions for detection priority. Fig. 4.5 shows four simulated overlapped but separated objects. Fig. 4.6 illustrates the sequence of detection and seeding for these four objects.



Figure 4.5 Four Simulated Objects

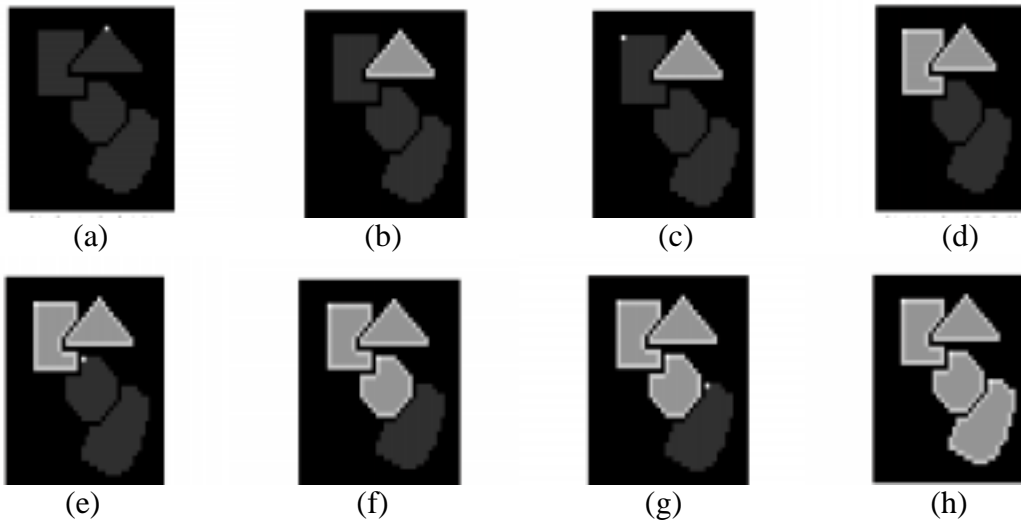


Figure 4.6 Sequence of Multi-object Detection and Seeding

4.5 Edge Detection, Region Growing and Particle Projected Area

The edge following point (EFP) traverses counter-clockwise along the edge of the detected object from the seed. Fig. 4.7 (a) illustrates a simulated object. During the edge traverse, the object interior points are scanned row by row, and counted before the

EFP moves to the next edge position below, as shown in Fig. 4.7 (b). Logic tests keep the algorithm from double-counting areas or missing parts of irregular objects. The scanning ends at the point where the original seed is reached again, as shown in Fig. 4.7 (c). At the end of the scanning, the particle edge and all of its interior points have been labeled and counted, and each edge point is stored in an ordered list.

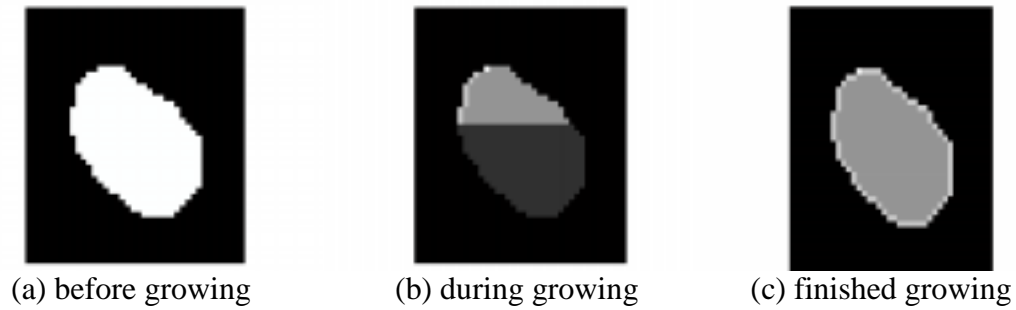


Figure 4.7 Region Growing

Fig. 4.8 demonstrates the edge traverse recording. The solid curve shows the vertical moving trajectory of the EFP, while dashed curve shows its horizontal moving trajectory. Note that both curves start at the same point, i.e., seed, and also end at that point. This shows that the full edge following has been completed.

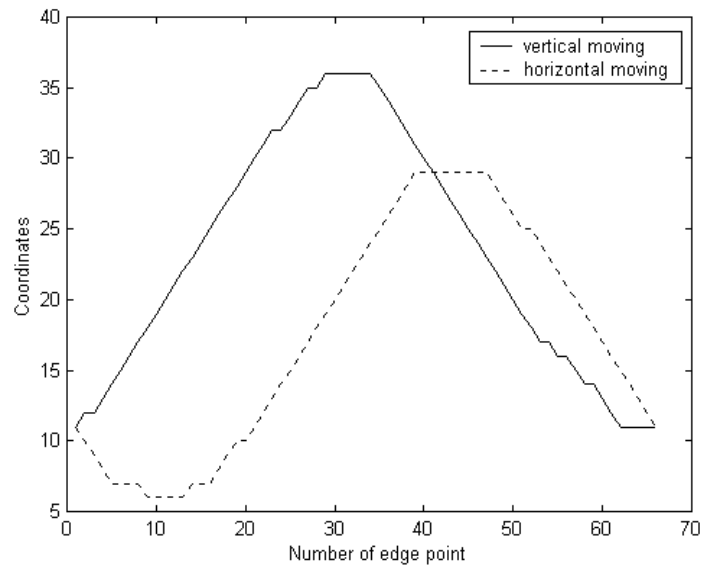


Figure 4.8 Edge Traverse Recording

When the edge following is completed, the total number of pixels on that object is known. Each pixel's area in terms of square millimeters is calculated using the $mm/pixel$ scale factors and Eqn. (3.1) obtained in the calibration described in Chapter 3. The summation of all the individual pixel areas equals the projected area of that object in question.

4.6 Centroid Location

When the region growing process is finished, the total number of edge points of that object is also available. This is accomplished by bookkeeping the number of new points on the edge while traversing is in progress.

In image processing problems, locating the centroid of an object in the 2-D plane is of great importance in shape description and object recognition. In many cases, the

centroid is used as a reference point to which the position of other points in question can be determined.

For a function $f(x,y)$, the moment of order $(p+q)$ is defined as m_{pq} , and the centroid coordinates can be found at

$$\bar{x} = \frac{m_{10}}{m_{00}} \quad (4.1)$$

$$\bar{y} = \frac{m_{01}}{m_{00}} \quad (4.2)$$

where, for a digital image,

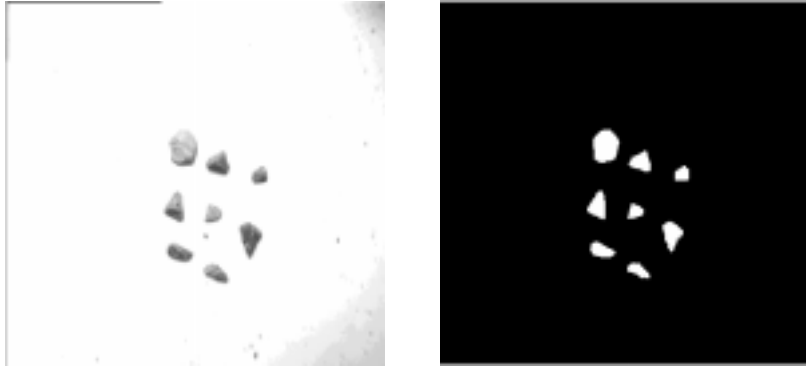
$$m_{00} = \sum_{x=0}^{m-1} \sum_{y=0}^{n-1} f(x, y) \quad (4.3)$$

$$m_{10} = \sum_{y=0}^{m-1} \sum_{x=0}^{n-1} xf(x, y) \quad (4.4)$$

$$m_{01} = \sum_{x=0}^{m-1} \sum_{y=0}^{n-1} yf(x, y) \quad (4.5)$$

where x and y indicate the coordinates of the image matrix.

Emdedding Eqn. (4.1) ~ (4.5) in the algorithm, the position of the centroid for each individual shape in the image is located. The centroid finding procedure now is applied to the real image as shown in Fig. 4.9.

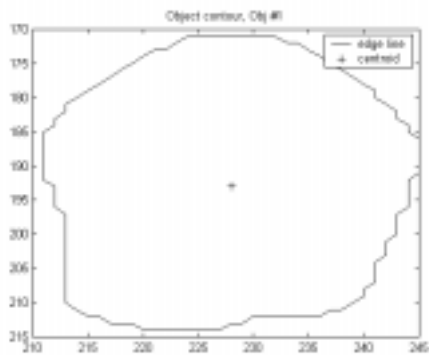


(a)

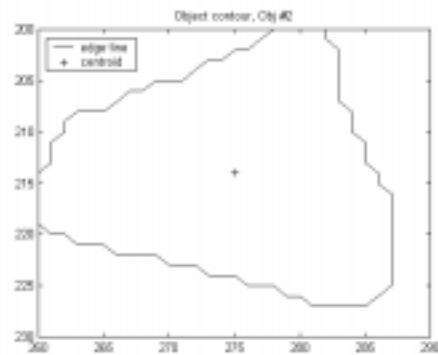
(b)

Figure 4.9 Eight Particles Imaged

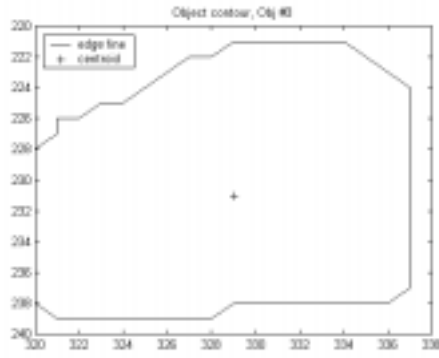
Fig. 4.10 shows the centroids found in the eight aggregate particles marked by the cross. Note that in each figure the values on x and y axis are the coordinates which enclose the particle shape in question. In other words, particle's edge is entirely included by the figure border.



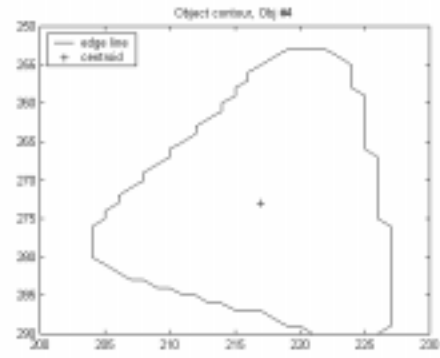
(a) 1st particle



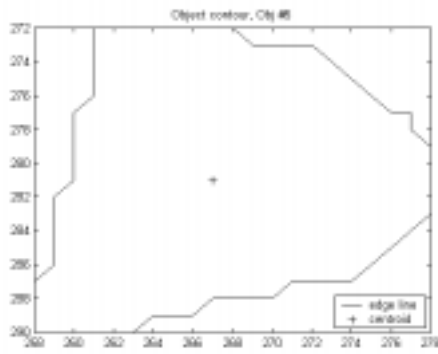
(b) 2nd particle



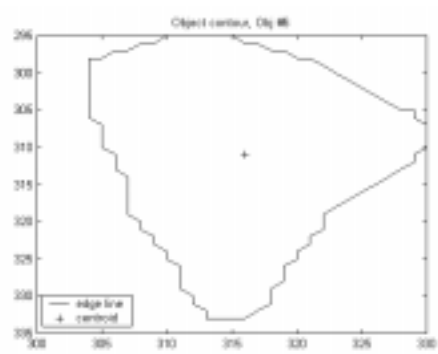
(c) 3rd particle



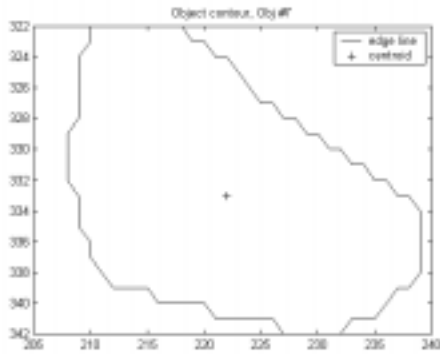
(d) 4th particle



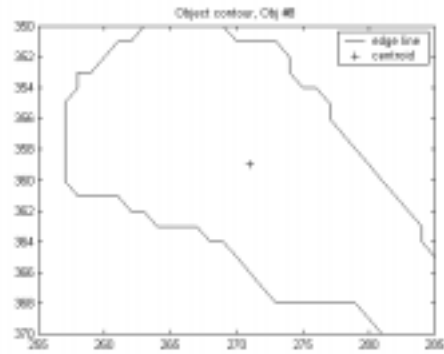
(e) 5th particle



(f) 6th particle



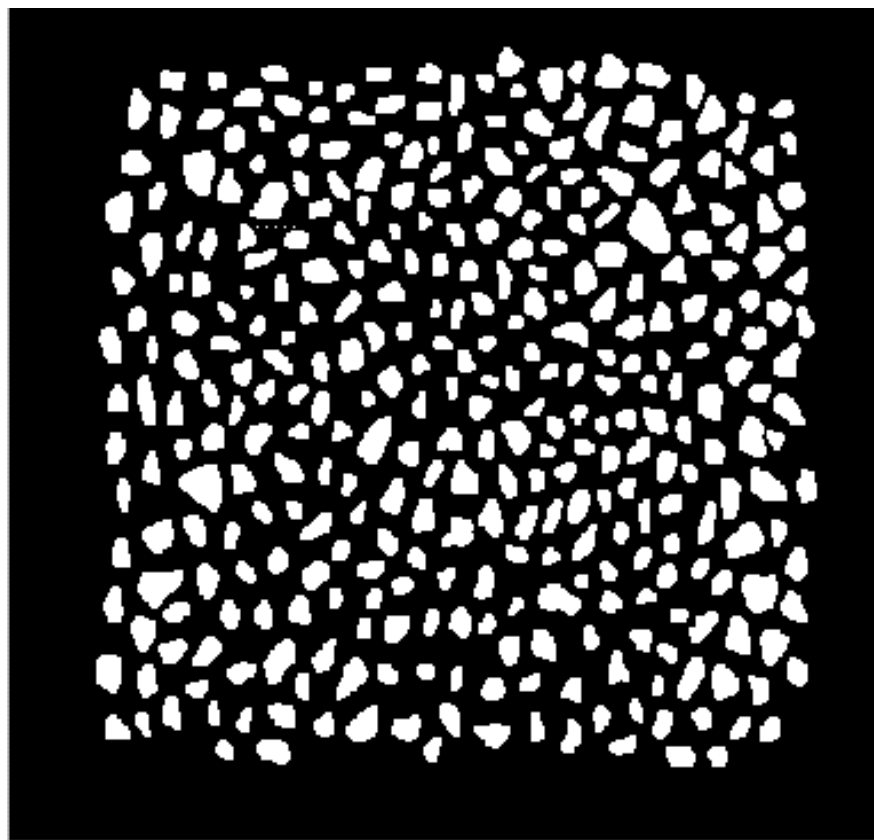
(g) 7th particle



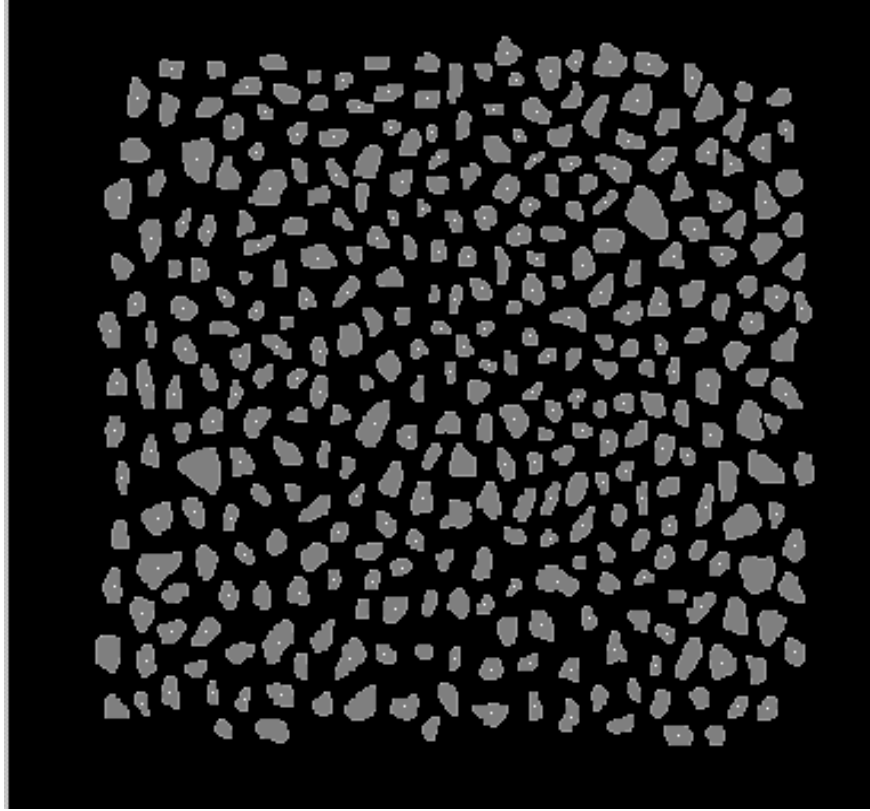
(h) 8th particle

Figure 4.10 Centroid of Profile Shape

Fig. 4.11 (a) shows the binary image of large number of aggregate particles, and (b) shows all the particles that have been processed.



(a) binary image of stock aggregates



(b) finished particle processing

Figure 4.11 Aggregate Processing

4.7 Major and Minor Diameter Computation

Image shape analysis relies on examining a two dimensional silhouette of the object. Techniques for describing the shape measure the simple geometric proportion of the object, such as the perimeter-to-diameter ratio, aspect ratio, etc.. Aspect ratio plays an important role in this research because aspect ratio reflects a particle's elongation, and the length of the minor axis is related to the sieve size. Aspect ratio is defined as the ratio of the maximum diameter to the orthogonal minimum diameter of the shape silhouette. For a random shape, finding its aspect ratio can be performed using principal component analysis, also called "principal eigen analysis". The two end-points of the major diameter

must be on the major eigen axis, and the two end-points of the orthogonal minor diameter must be on the minor eigen axis, as demonstrated in Fig. 4.12.

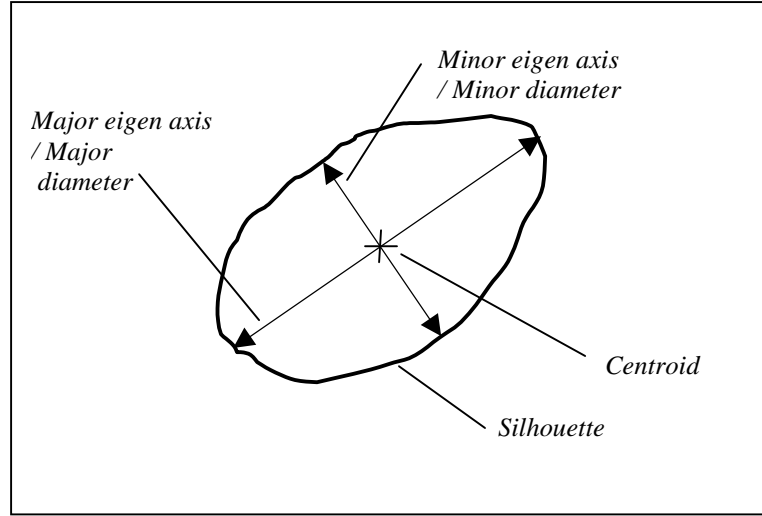


Figure 4.12 Major and Minor Diameter

Consider a set \mathbf{P} of edge point $p(x,y)$ on the contour of interest, with $\mathbf{P} = [\mathbf{p}_1 \mathbf{p}_2 \dots \mathbf{p}_n]$ and

$$\mathbf{p}_i = \begin{bmatrix} x_i \\ y_i \end{bmatrix} \quad (4.6)$$

The mean vector and the covariance matrix are defined as

$$\mathbf{m}_p = \mathbf{E} \{ \mathbf{p}_i \} = \frac{1}{N} \sum_{i=1}^N \mathbf{p}_i \quad (4.7)$$

$$\mathbf{C}_p = \mathbf{E} \{ (\mathbf{p}_i - \mathbf{m}_p)(\mathbf{p}_i - \mathbf{m}_p)^T \} \quad (4.8)$$

where T indicates vector transpose, E is the expected value operator. Because \mathbf{p}_i and \mathbf{m}_p are two dimensional, \mathbf{C}_p must be a matrix of order 2×2 . Element c_{ii} of \mathbf{C}_p is the variance

of x and y in \mathbf{p}_i , and element c_{ij} of \mathbf{C}_p is the covariance between x and y . The matrix \mathbf{C}_p is real and symmetric.

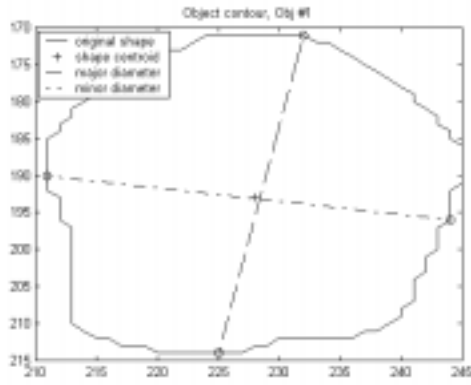
For M vector samples, namely, M edge points, the mean vector and covariance matrix are computed as

$$\mathbf{m}_p = \frac{1}{M} \sum_{i=1}^M \mathbf{p}_i \quad (4.9)$$

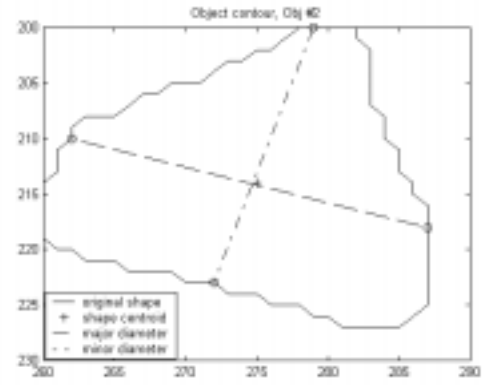
$$\mathbf{C}_p = \frac{1}{M} \sum_{i=1}^M (\mathbf{p}_i \mathbf{p}_i^T - \mathbf{m}_p \mathbf{m}_p^T) \quad (4.10)$$

Because the matrix \mathbf{C}_p is real and symmetric, finding a set of orthogonal eigenvectors of dimension 2 is always possible [2]. Let λ_1 and λ_2 be the eigenvalues of \mathbf{C}_p , with $\lambda_1 > \lambda_2$, and correspondingly, let \mathbf{e}_1 and \mathbf{e}_2 be the resultant eigenvectors. The direction of vector \mathbf{e}_1 indicates the orientation of the particle's major eigen axis, and likewise, the direction of \mathbf{e}_2 coincides with the direction of its minor eigen axis. The end-points of the major and minor axes within the contour can be found, so that the major diameter and its orthogonal minor diameter can thus be obtained.

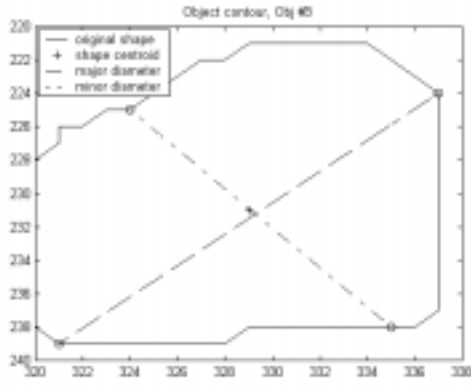
Fig. 4.13 shows the two end-points of major and minor axis found on the edge line of the image shown previously in Fig. 4.9. Note that some major and minor diameters do not appear orthogonal because of pixel's aspect ratio.



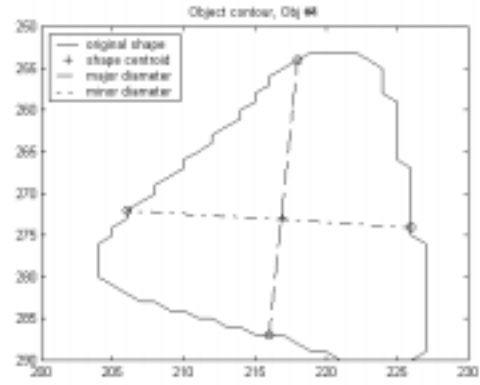
(a) diameters for object #1



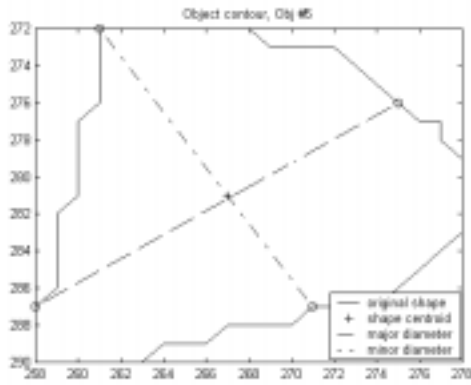
(b) diameters for object #2



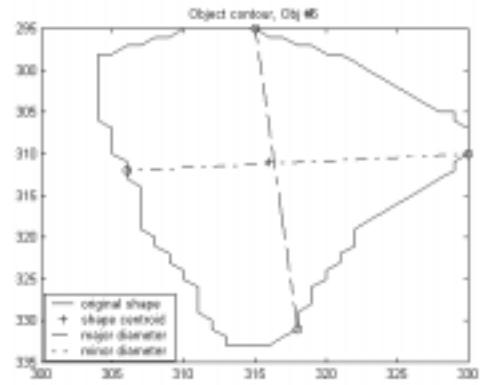
(c) diameters for object #3



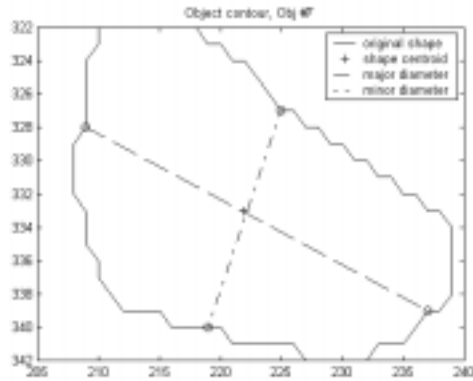
(d) diameters for object #4



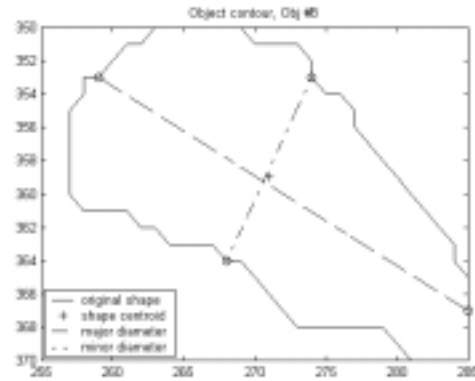
(e) diameters for object #5



(f) diameters for object #6



(g) diameters for object #7



(h) diameters for object #8

Figure 4.13 Major and Minor Diameter

After obtaining the major and minor diameter, the aspect ratio of the profile shape of the particle is computed.

4.8 Profile Shape Characterization

The major reason for needing to know the approximate shape of the particles lies in the fact that shape affects the strategy for converting the particle profile into an equivalent sieve size. For example, rectangular particles will sieve to the smaller of the two dimensions, which can be found approximately using the minor diameter. On the other hand, a triangular shaped particle will sieve to one vertex and the opposite side, the length that is sieved to is greater than the minor diameter of the profile shape. This requires modification of the minor diameter.

Using the list of edge points to plot the radius from the centroid to each edge point, a relation called “signature” is constructed. Fig. 4.14 illustrates such a functional relation for a square. Irrespective of how such a signature is created, the basic idea

remains to reduce the boundary description to a 1-D function, which is easier to describe than the original 2-D contour.

Signatures generated in this way are invariant to translation, but they do depend on rotation and scaling. To achieve invariance of the signature to both scaling and orientation, the plot may be normalized by finding a consistent way to select the same starting point to generate the signature. For instance, the edge point, which has the maximum radius to the centroid, can be selected to start calculating the radius. The maximum radius is also used to scale all signatures to a uniform range, $[0,1]$. The normalization step removes dependency on size and rotation but preserves the fundamental shape of the particle's contour.

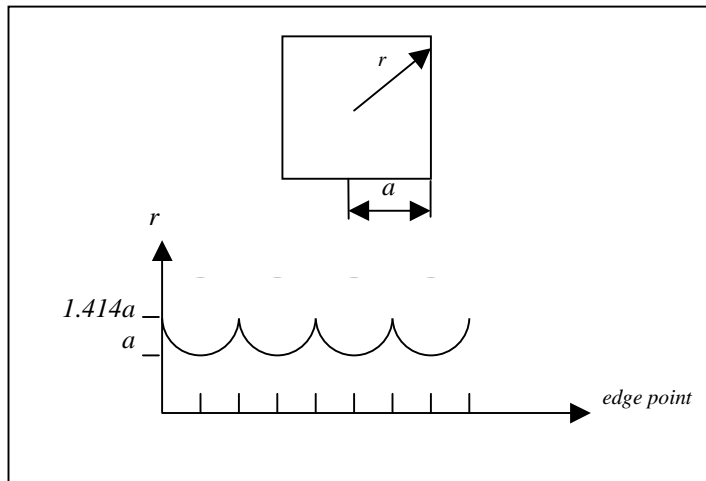


Figure 4.14 Signature

Signatures are used to store and reveal the profile shape information. Analyzing their patterns can give certain shape characteristics. For example, a relatively straight

line parallel to the abscissa indicates that the object's shape is circular. If the signature of a convex shape has four sharp peaks of the same radius and four smooth valleys also of the same radius, and all are evenly spaced along the abscissa, it can be deduced that this object's shape is square shaped. Three peaks and three valleys in a signature imply a triangular shape in a general sense. For a convex object, its shape can be characterized by its simplified contour obtained from connecting all the characteristic vertices, provided these characteristic vertices can be detected. Fig. 4.15 demonstrates this idea, in which the contour \overline{ABCD} can be used to characterize the object's original shape.

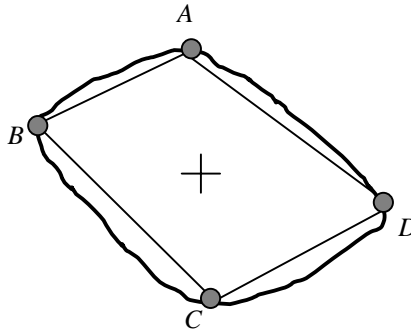


Figure 4.15 Characterizing a Shape

Although all the vertices can be extracted from the signature by observing its first derivative quantities, identifying a few characteristic ones is not an easy task. This is because the signature of an imaged object usually is very noisy, and many points that may not serve the characterizing purpose may be picked as major vertices, making the shape feature description complex. In order to efficiently find the characteristic vertices, noise must be removed.

Polynomial curve-fitting can effectively approximate functions (interpolating polynomials) to smooth out noisy experimental and numerical data, and provide a simple analytical expression. The most commonly chosen form is the polynomial:

$$g(x)=a_0 x^p + a_1 x^{p-1} + a_2 x^{p-2} + a_3 x^{p-3} + \dots + a_{p-2} x^2 + a_{p-1} x + a_p \quad (4.11)$$

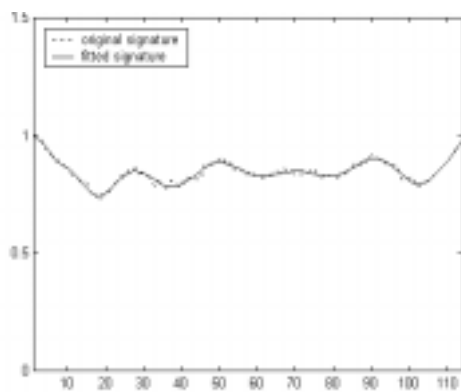
where x is the variable of edge points.

Determination of the order of the polynomial p is problem dependent. For a given set of data points, an order too high causes detection of unwanted and insignificant vertices, an order too low lacks sensitivity of detection. After trial-and-error, $p=18$ was selected in this research. After the order was chosen, the first derivative of the polynomial was taken to identify characteristic vertices, using:

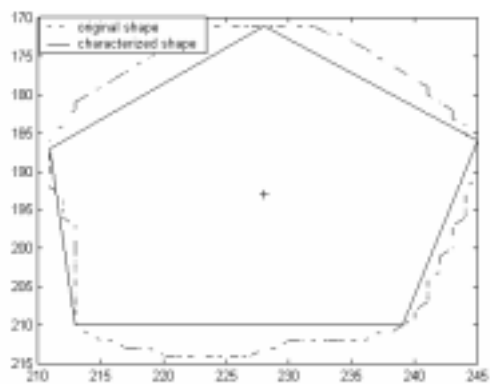
$$\frac{dg(x)}{dx} = 0 \quad (4.12)$$

to locate the positions of the desired vertices on the original signature. The number of maxima and minima is an indicator to the number of “corners” and “sides” that the particle has.

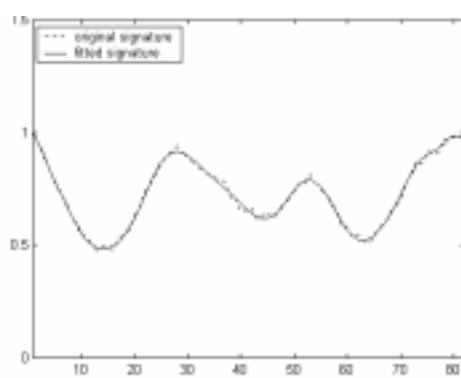
Now, taking the same images as shown in Fig. 4.9, the selected polynomial is applied to identify these eight particles’ profile shape. Fig. 4.16 demonstrates the results. All plots in the left column show the polynomial curve-fitting effect, and shapes identified on the other.



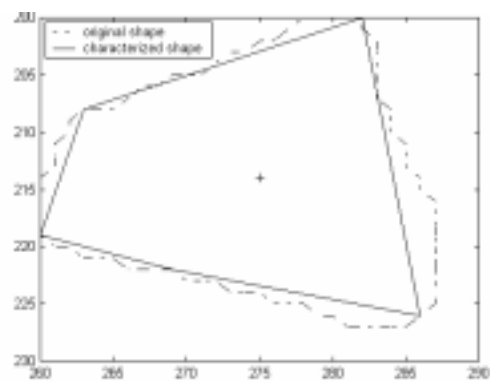
(a) curve-fitting for object #1



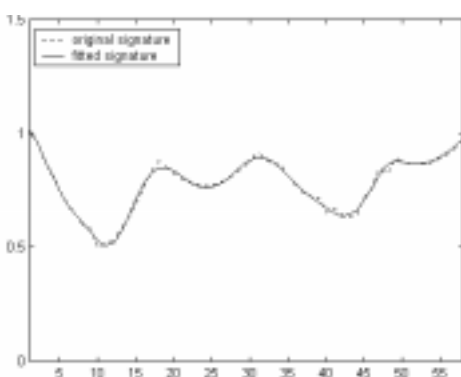
(b) characterized shape for object #1



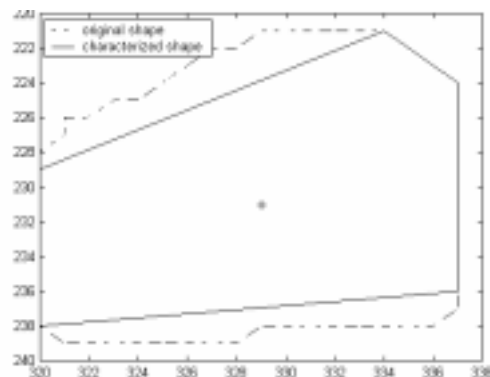
(c) curve-fitting for object #2



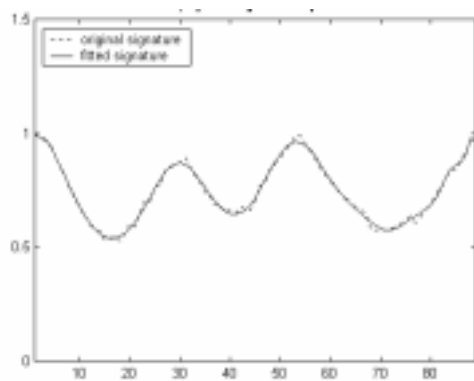
(d) characterized shape for object #2



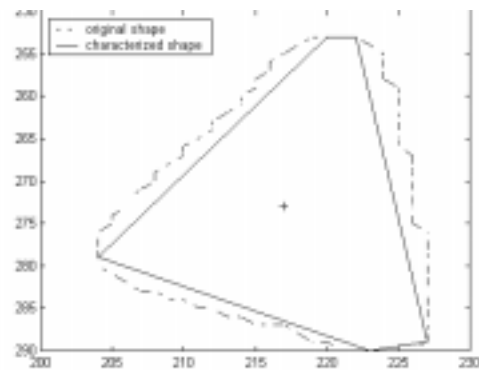
(e) curve-fitting for object #3



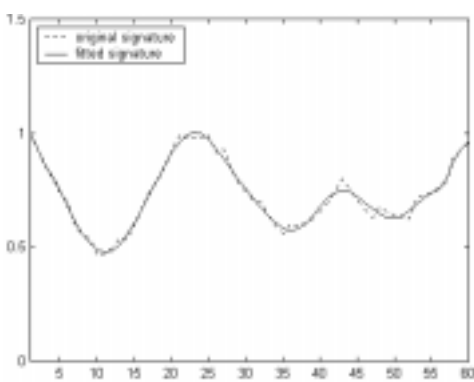
(f) characterized shape for object #3



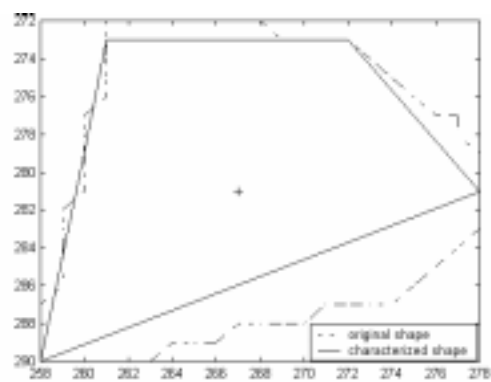
(g) curve-fitting for object #4



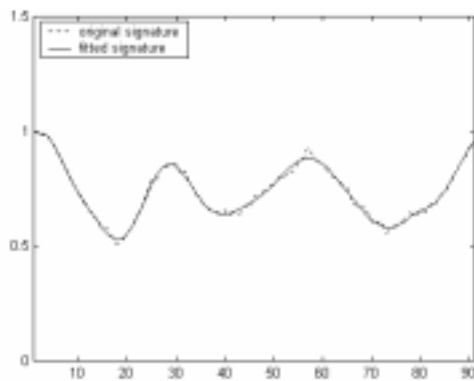
(h) characterized shape for object #4



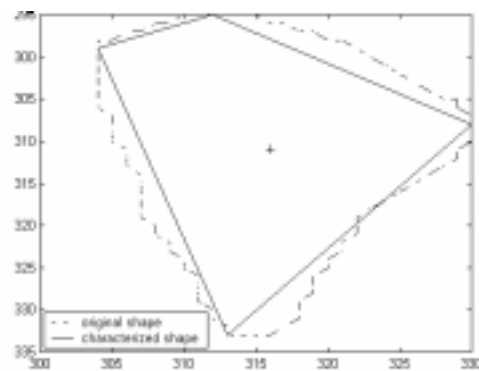
(i) curve-fitting for object #5



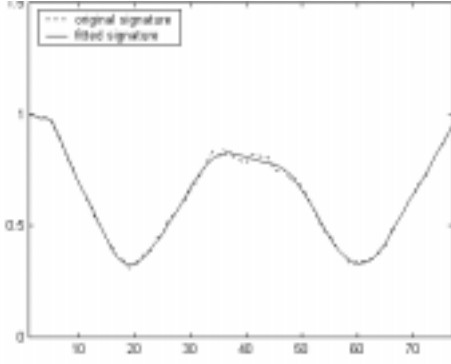
(j) characterized shape for object #5



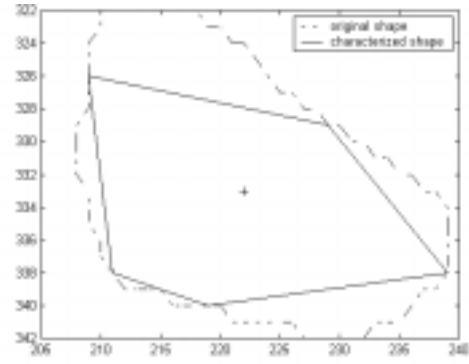
(k) curve-fitting for object #6



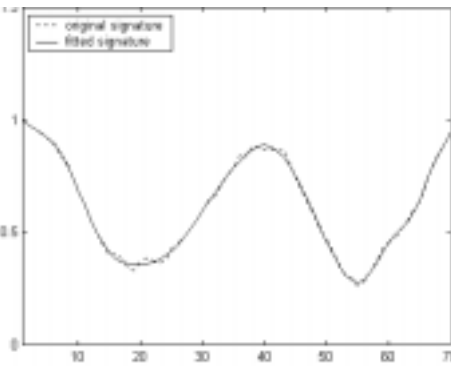
(l) characterized shape for object #6



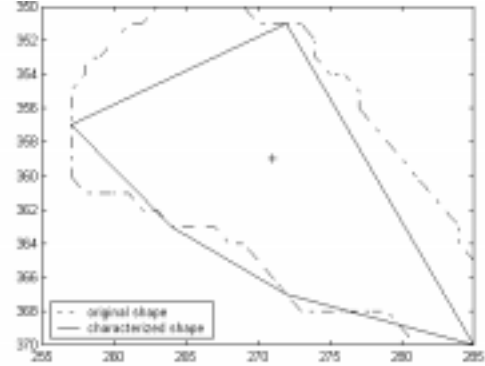
(m) curve-fitting for object #7



(n) characterized shape for object #7



(o) curve-fitting for object #8



(p) characterized shape for object #8

Figure 4.16 Curve-fitting and Shape Characterization

Note that some obviously triangular shapes are “over characterized”, which means that an expected triangular shape is identified as four or five-sided shape instead. Naturally, reducing the order of the polynomial may be able to partially overcome this drawback. However, the side effect is inevitable, that is, some true four or five-sided shapes may be mistaken as triangles. So, in the algorithm of this research, it is regulated that if the number of edge points covering a side length of the shape is less than $1/8$ the total number of edge points, this side can be ignored.

5. SEPARATION OF TOUCHING AND OVERLAPPING PARTICLES

5.1 Introduction

In the processing of aggregate particle images, two problems must be solved before size and shape analysis begin. First, if the particles are touching or overlapping, two or more particles will appear as one large, irregularly shaped particle. Second, each image consists of many individual particles, all of which must be processed individually to determine particle size, shape and mass. These two problems demand separation of all touching or overlapping particles before further analysis can be conducted on the image.

Morphological processing techniques can be used to convert the binary image to a gray scale *topographic* surface [21]. In this chapter, some basic morphological concepts are reviewed. The 3-D geometric characteristics existing between two touching or overlapping objects are analyzed. A morphological erosion process is demonstrated, which leads to finding a saddle point in a concave particle outline. A cut line is made through the saddle point and eventually the two objects are separated.

5.2 Binary Erosion

The fundamental operations of mathematical morphology are erosion and dilation. In this work, erosion is the more important process, and can be described as follows: suppose a binary image $\mathbf{I}_{m \times n}$ contains background pixels with value 0 and object pixels with value 1. Assume that the object pixels are grouped into a single, contiguous object \mathbf{A} comprised of q pixels $a_1, a_2, \dots, a_q, q < m \times n$. Let $\mathbf{B} = \{b_1 \ b_2 \ \dots \ b_k \}$ be a structuring element, which is a set of binary points that are usually (but not necessarily) contiguous

and that usually (but not necessarily) describes some geometric shape – a line, disk, rectangle, etc. Let b_r be the reference point for \mathbf{B} . Note that b_r is usually (but not necessarily) an element of \mathbf{B} . The structuring element \mathbf{B} moves over the image. When \mathbf{B} is completely contained in \mathbf{A} , the reference point location goes into the eroded set. In other words, an eroded image is constructed by a set that is made up of the locations of the reference point of structuring element \mathbf{B} , for those locations $\mathbf{B} \subset \mathbf{A}$. Fig. 5.1 portrays a typical erosion process.

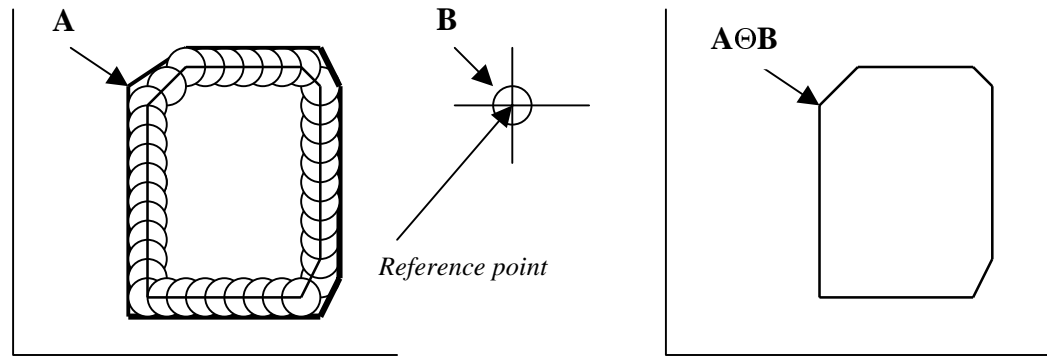


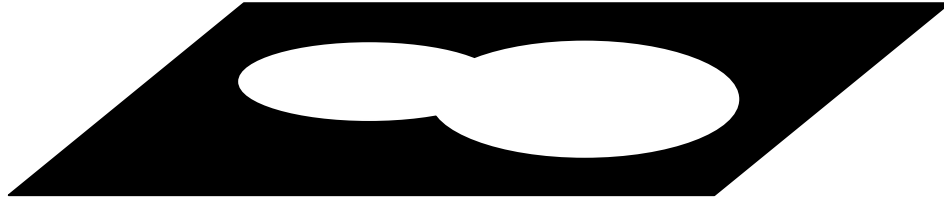
Figure 5.1 Typical Erosion as Shrinking

5.3 Sequential Erosion

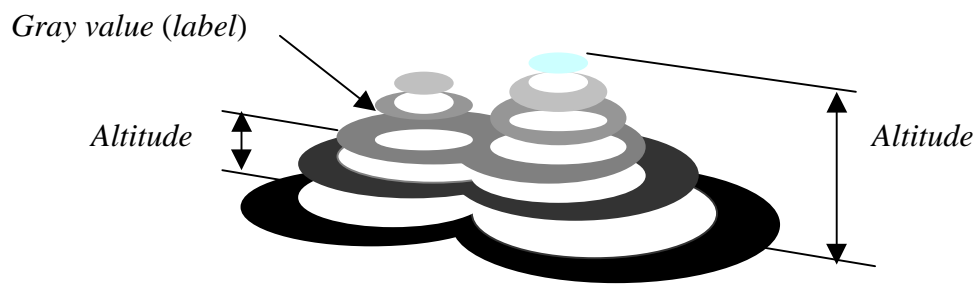
The erosion process is performed by mathematically “moving” the structuring element over the object image. At each location, a simple Boolean process is used. If the structuring element is completely contained in the object to be eroded, the pixel location corresponding to the reference point of the structuring element is placed in the new set, which forms the eroded object. Otherwise, the reference pixel becomes background in the new image that contains the eroded object(s).

In a sequential erosion, when the eroded object can not be eroded any more, in other words, at the point when the eroded object can not entirely contain the structuring element any more, this state is called *ultimate erosion*.

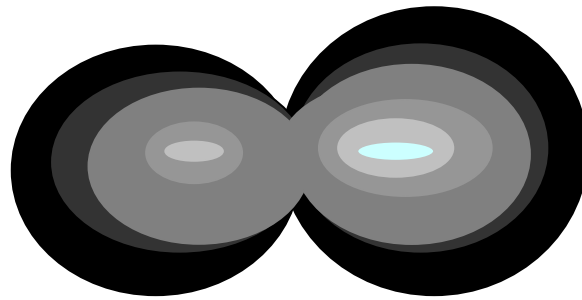
Sequential erosion on binary images is widely used in morphological processing. For example, computation of *gradients*, *marking functions*, *distance functions* are based on sequential erosion [21]. The basic mechanism is that as an erosion is performed, the eroded section is labeled with a value that increases with each erosion operation. The original binary image is thus converted to a gray-scaled ‘mountain’. The brightest part (largest gray value, or highest altitude) is located at the ultimate erosion for that shape. Fig. 5.2 illustrates the sequential erosion process.



(a) original binary image



(b) after ultimate erosion (oblique view)



(c) after ultimate erosion (top view: topographic surface)

Figure 5.2 Sequential Erosion

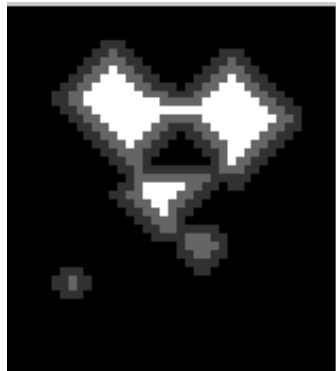
Fig. 5.3 shows the whole sequential erosion process for a simulated image on a matrix of size 44×40 in which touching and overlapping take place. A structuring element of size 3×3 was used.



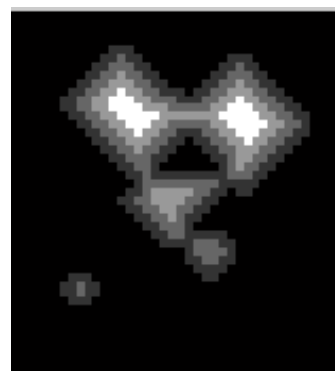
(a) before erosion



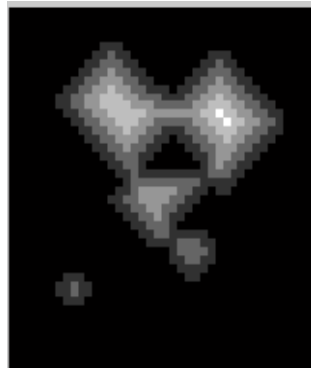
(b) 1st erosion



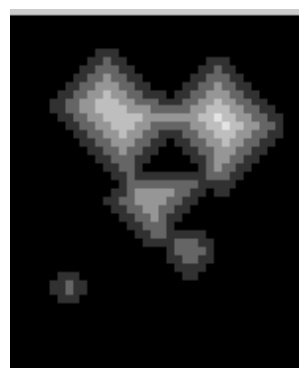
(c) 2nd erosion



(d) 3rd erosion



(e) 4th erosion



(f) ultimate erosion

Figure 5.3 Sequential Erosion on Simulated Image

The pseudocode of the sequential erosion is listed in Table 5.1 below.

Table 5.1 Pseudocode of Sequential Erosion

```
/* A binary image set I is available, a structuring element B is selected. */  
  
for (total each number of erosion operation)  
  
    for (each pixel in the image)  
        if (the structuring element B is completely included in an object )  
            - create a new set E , E forms the eroded object in the new image set.  
        end  
    end  
  
    - label C, the complement set of I and E, a non-zero value which will be increased for next erosion  
    operation Otherwise all are labeled 0 for background, 1 for E.  
    - assign this new image set to I which becomes the next image to be further eroded in next operation.  
  
    /* Check if the ultimate erosion is reached. */  
    if (the the eroded object still can contain B )  
        - start next erosion operation on this new image.  
    else  
        - stop.  
        - obtain the final sequentially eroded grayscale image (topographic surface) by adding up all C's  
    end  
  
end /*end of the first "for" loop*/
```

The total number of erosion operations necessary to reach the ultimate erosion and morphological gradient of the eroded grayscale image depends on structuring element size, and on the size and shape of the object. The smaller the structuring element size (greater than one pixel, of course), the more topographic information can be revealed. Obviously, this comes with a trade-off of longer run time for computer.

5.4 Separating Location

As shown in Fig. 5.3, successive bands (or rings) created by the erosion are assigned grayscale values, increasing with each erosion operation. The bands generate a contour for each object, similar to a topographic contour map. After the ultimate erosion, a complete topographic surface is formed. An inevitable characteristic for those touching and overlapping object shapes can be noted: a saddle shaped surface exists between two connected objects in the topographic plane. The erosion process serves the purpose of creating the topographic surface, on which the right place to cut these two connected objects apart is located. The right place to cut is located at the “saddle point”, which mathematically is the point where a 3-D function simultaneously reaches a (local) minimum in one direction and a (local) maximum in the other direction. Examples would be the center of a saddle seat or the lowest point (gap) in a ridge between two hills. Fig. 5.4 depicts the saddle shaped surface over two connected hills and saddle point location. Note that the saddle point S has the minimum value in the plane A , and meanwhile the maximum value in the plane B . Both planes are perpendicular to the background and intersect each other through the saddle point.

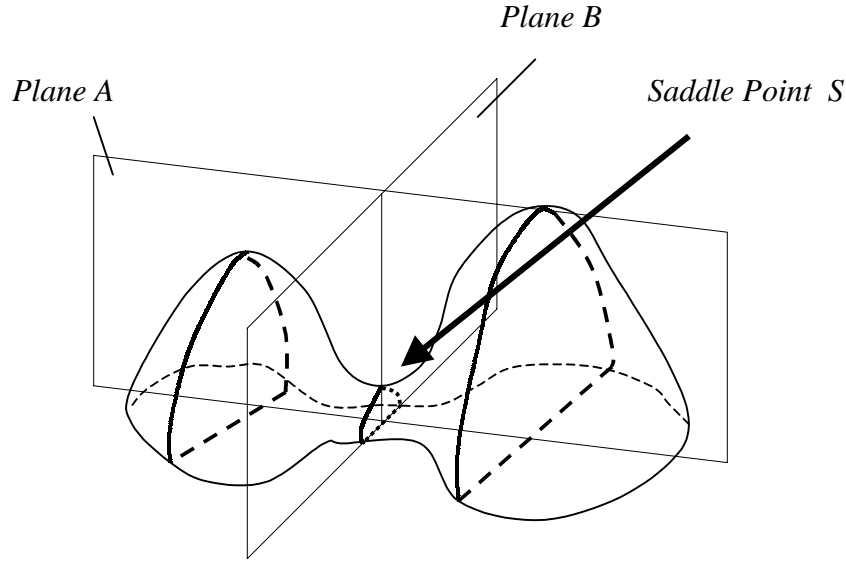


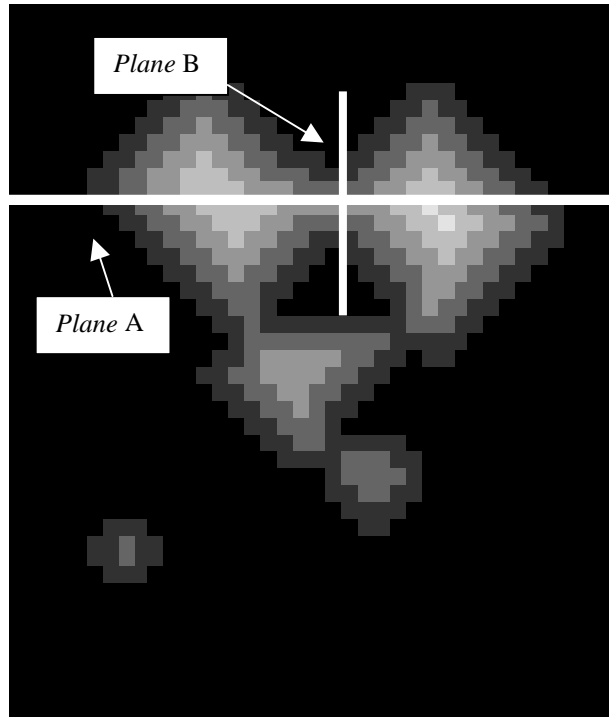
Figure 5.4 Saddle and Saddle Point

The saddle point in the ultimately eroded image shown in Fig. 5.3 (f) can be located. Fig. 5.5 (a) shows the two dissecting plane locations to find the saddle point between two hills, and (b) illustrates these two corresponding plane locations in the topographic map. Mathematically, the point set in each plane constructs a parabolic curve, with opposite opening direction. The saddle point is located at the intersecting point of these two curves. Note that the same saddle point has the minimum value for the set of all the gray value points in the plane A, and the maximum value in the plane B. Notationally, let **A** be the set of all gray value points in the plane A, and **B** the set of all gray value points in the plane B, s the gray value at the saddle point, then the following equations hold:

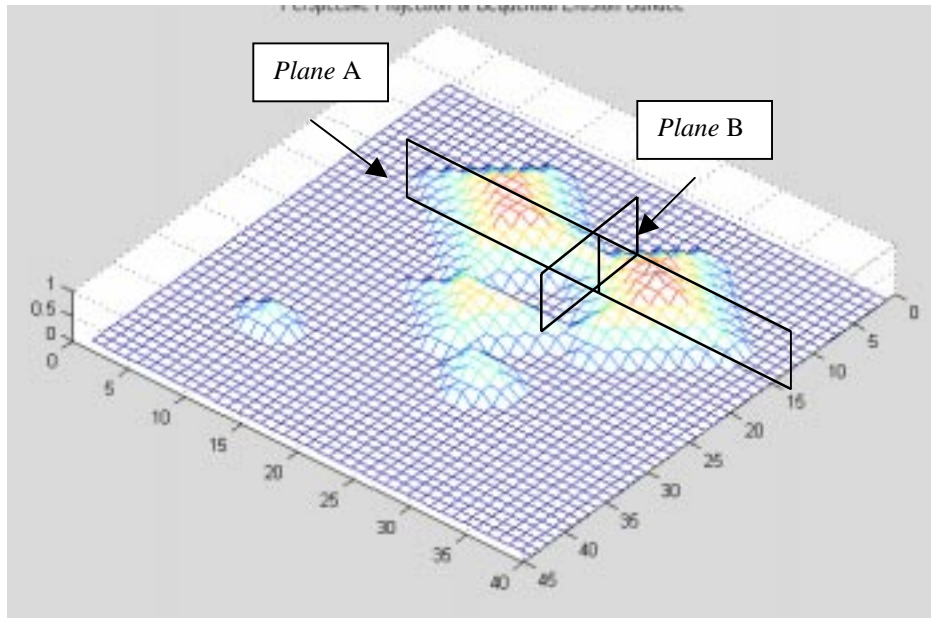
$$s = \min\{a_i, \forall a_i \in \mathbf{A}, i=1,2,\dots,n\} \quad (5.1)$$

$$s = \max\{b_i, \forall b_i \in \mathbf{B}, i=1,2,\dots,m\} \quad (5.2)$$

Once the saddle point is located, next is to determine the direction of cutting. The cutting line is contained in the plane that contains maximum gray value with the parabolic curve opening downward. In the above example, the cutting line is contained in plane *B*.



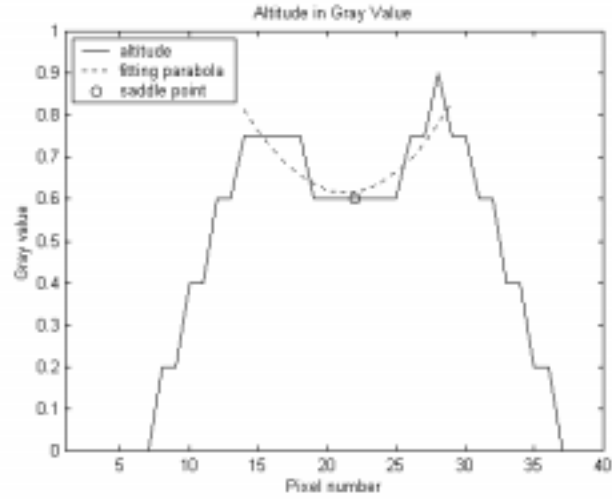
(a) dissecting planes (top view)



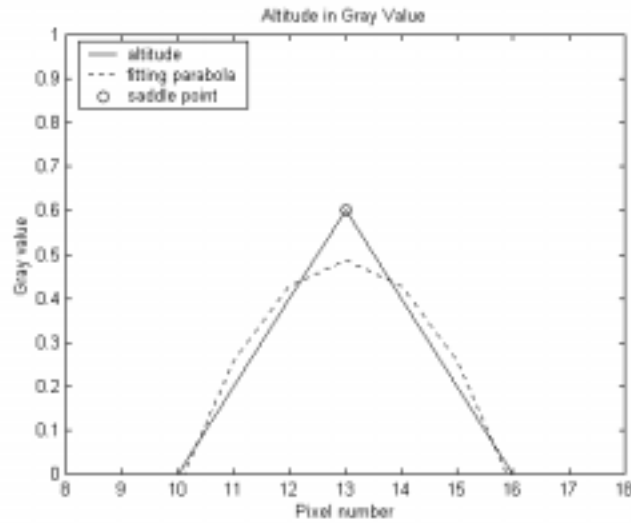
(b) dissecting planes (oblique view)

Figure 5.5 Dissecting Planes for Finding Saddle Point

More specifically, Fig. 5.6 (a) shows the altitude in gray value in dissecting plane *A* with a fitting parabola opening upward. Similarly, (b) shows the altitude in dissecting plane *B* with a fitting parabola opening downward. Note that both sets intersect at gray level of 0.6, and the desired saddle point is located at position (13,22) with the gray level 0.6.



(a) altitude in plane A



(b) altitude in plane B

Figure 5.6 Gray Level Altitude in Plane A and B

5.5 Detection of Saddle Point by Filtering

5.5.1 Filter Design

A filter (or mask) can be designed to detect the saddle shaped domain and accordingly, the saddle point in the topographic surface. Based on finding saddle point,

the cutting line can be oriented and separation can be carried out. Since the geometric characteristics of saddle surface are known, a filter was engineered to serve the separating purpose.

Again, hold the same definitions made for the plane A , plane B and the set \mathbf{A} , set \mathbf{B} , as stated in the last section. Further, let a filter have the size of $n \times m$, each grid holds value f_{ij} , $i=1,2,\dots,n$, $j=1,2,\dots,m$. Fig. 5.7 shows a filter of size 5×5 .

f11	f12	f13	f14	f15
f21	f22	f23	f24	f25
f31	f32	f33	f34	f35
f41	f42	f43	f44	f45
f51	f52	f53	f54	f55

Figure 5.7 A Filter of Size 5×5

The objective of designing a filter is to locate the saddle point. This requires that the filter can detect the gray value points distributing in a parabolic pattern in both planes A and B . To achieve this, the value in each grid of the filter is assigned with $+1$ or -1 , symmetric about the reference point f_{ij} in planes A and B . At each reference point, plane A and B are assumed to be orthogonal to each other, and may rotate simultaneously from 0° to 90° anti-clockwise searching for the orientation that qualifies the reference point to be the saddle point. If the preset conditions as given in the next section are met, the current reference point becomes the saddle point, and cutting then begins in the orientation of plane B . Fig. 5.8 demonstrates the values given for a filter of size 5×5 , and the filter rotates from 0° to 90° .

0	0	+1	0	0
0	0	+1	0	0
+1	+1	0	-1	-1
0	0	-1	0	0
0	0	-1	0	0

(a) filter at 0°

0	+1	0	0	0
0	+1	0	-1	-1
0	0	0	0	0
+1	+1	0	-1	0
0	0	0	-1	0

(b) filter rotated by 22.5°

+1	0	0	0	-1
0	+1	0	-1	0
0	0	0	0	0
0	+1	0	-1	0
+1	0	0	0	-1

(c) filter rotated by 45°

0	0	0	-1	0
+1	+1	0	-1	0
0	0	0	0	0
0	+1	0	-1	-1
0	+1	0	0	0

(d) filter rotated by 67.5°

0	0	-1	0	0
0	0	-1	0	0
+1	+1	0	-1	-1
0	0	+1	0	0
0	0	+1	0	0

(e) filter rotated by 90°

Figure 5.8 Rotation of Filter

5.5.2 Saddle Point Conditions

The filter demonstrated above can be extended to any larger size, and the rotating angle step then may be smaller accordingly. Suppose that in the plane A , there exist two points that are symmetrical to the reference point S (recall that S is also in the plane B). Let these two points denote $P_{A,R}$ and $P_{A,L}$ (subscript R and L indicate *Right* and *Left* to S in the plane A), which take the gray value (altitude) $I_{A,R}$ and $I_{A,L}$, respectively. Correspondingly, assume that the filter values at these two locations are $f_{A,R}$ and $f_{A,L}$ (Note that if one is $+1$, the other must be -1), respectively.

Mathematically, if this reference point is detected as a saddle point S which takes gray value s_{ij} , the following conditions hold:

In plane A , at certain orientation θ in the image plane,

$$I_{A,R}f_{A,R} + I_{A,L}f_{A,L} = 0 \quad (5.3)$$

$$s_{ij} = \min\{P_{ij}, \forall P_{ij} \in \mathbf{A}\} \quad (5.4)$$

Eqn. (5.3) ensures the two gray value points in plane A have the same gray value, and Eqn. (5.4) indicates that the parabolic shape opens upward, and the reference point S is at bottom on the parabola.

Similarly, in orthogonal plane B at $(\theta \pm 90^\circ)$ in the image plane,

$$I_{B,R}f_{B,R} + I_{B,L}f_{B,L} = 0 \quad (5.5)$$

$$s_{ij} = \max\{P_{ij}, \forall P_{ij} \in \mathbf{B}\} \quad (5.6)$$

For the sake of clarity, two more characteristics may be observed,

$$s_{ij} \in (\mathbf{A} \cap \mathbf{B}) \quad (5.7)$$

$$(\mathbf{A}, \mathbf{B})^c = (\mathbf{A} \cup \mathbf{B}) - (\mathbf{A} \cap \mathbf{B}) \quad (5.8)$$

where $(\mathbf{A}, \mathbf{B})^c$ denotes the complement set of sets \mathbf{A} and \mathbf{B} .

The separation algorithm can be described as follows:

Step 1: At each reference point with θ° orientation in plane A , first check its left and right neighboring pixels' gray value, see if all conditions set in Eqn. (5.3) and (5.4) are satisfied. If not, then extend to next pair of pixels before and after the two pixels just checked in the same plane. Same process is taken until the conditions are satisfied within the preset filter size n .

Step 2: If the conditions are met during searching within the preset filter size n , then further check its upper and lower neighboring pixels in the orthogonal plane B , see if

all conditions set in Eqn. (5.5) and (5.6) are satisfied. If not, check next pair of pixels' gray value extending upward and downward within the preset filter size m .

Step 3: If an affirmative answer has been obtained for step 1 and 2, in other words, if logical *AND* is used to combine the two conditions set in *step 1* and *step 2*, and a positive answer is found, then the current reference point is the desired saddle point. Followed is to carry out the cutting process in the direction of plane *B*. *Step 1* to *Step 3* are repeated for the next new reference point in the image.

Step 4: If a negative answer has been found in either *step 1* or *step 2*, in other words, the *AND* logic fails, then the current reference point is not the saddle point at the current orientation, stop.

Step 5: Simultaneously rotate the plane *A* and plane *B* to certain orientation, repeat *step 1* to *step 5*.

Step 6: If after a rotation of 90° is finished, and no *AND* logic is found affirmative, then the current reference point is detected as a non-saddle-point. Move to the next new reference point, repeat *Step 1* to *Step 6*.

The simplified pseudocode of separation for touching and overlapping shapes is listed as follows:

Table 5.2 Pseudocode of Separation

```
/*A gray scale ultimately eroded image G is available, and a filter of size  $n \times m$  is selected.*/  
/*Scan with the filter */  
for (each reference point)  
    if (within the filter size  $n$  in plane A, all conditions are met, referring to Eqn. (5.3)and (5.4))  
        AND (within the filter size  $m$  in plane B, all conditions are met, referring to Eqn. (5.5) and  
            (5.6))  
            - the current reference point is a saddle point  
            - cut in the direction of plane B  
    else  
        - simultaneously rotate both plane A and B anti-clockwise to certain angle, provided a total  $90^\circ$  is  
            not swept. Otherwise stop.  
        - go back to above "if" condition, check AND logic again in new orientation just rotated.  
    end  
  
end /* end of "for" loop */
```

Referring to Fig. 5.5 (a), the separated shapes are shown in Fig. 5.9 (b), while (a) shows the connected shapes.



(a) connected shapes



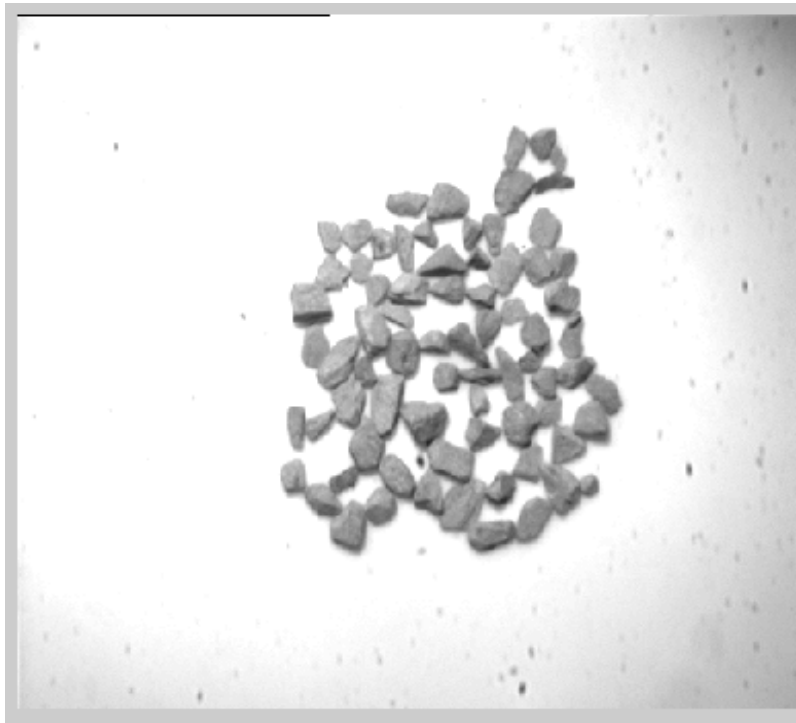
(b) separated shapes

Figure 5.9 Separation by Filtering

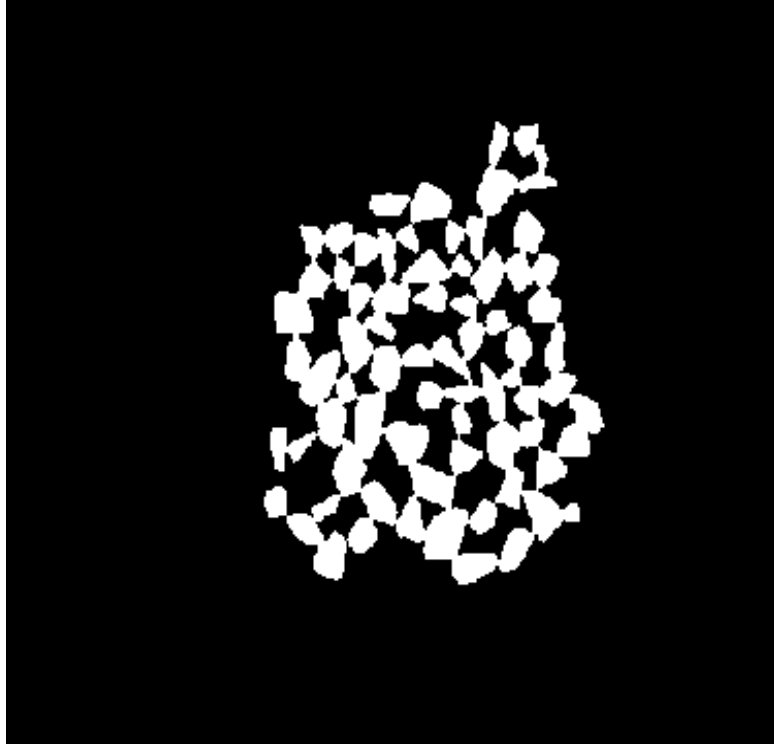
5.6 Testing on a Real Image

Now, using a structuring element of size 3×3 for sequential erosion, and a filter of size 15×15 for saddle point detection, the touching and overlapping limestone rocks

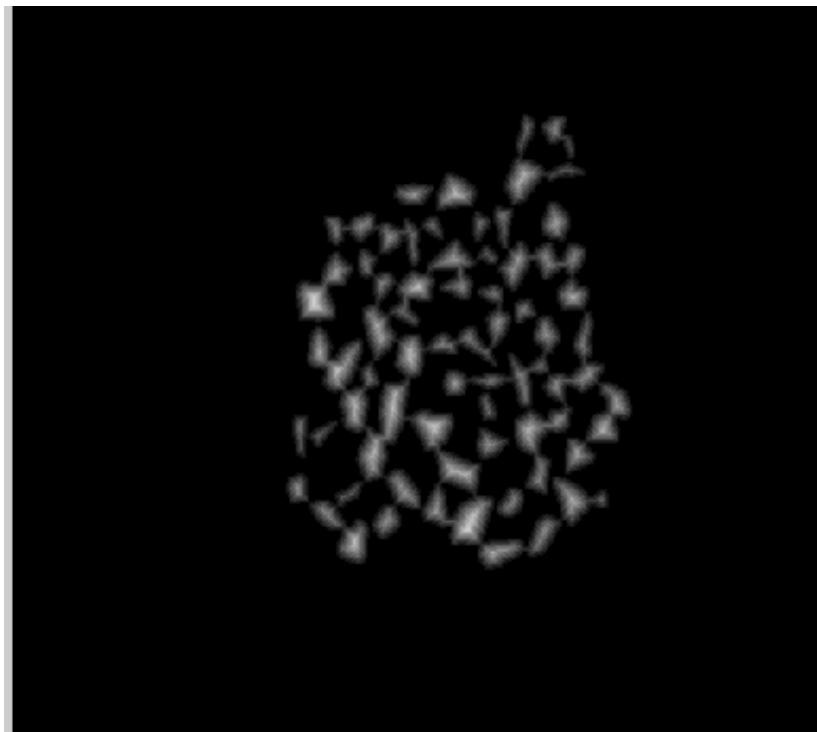
digitized in a 484×512 matrix, as shown in Fig. 5.10 (a), was separated. The corresponding binary image is given in sub-figure (b). A total of 10 erosion operations has been elapsed before the ultimate erosion is reached. Sub-figure (c) demonstrates the resultant topographic surface, while (d) portrays the same topographic surface in an oblique view. Finally, an image of separated particles is presented in sub-figure (e).



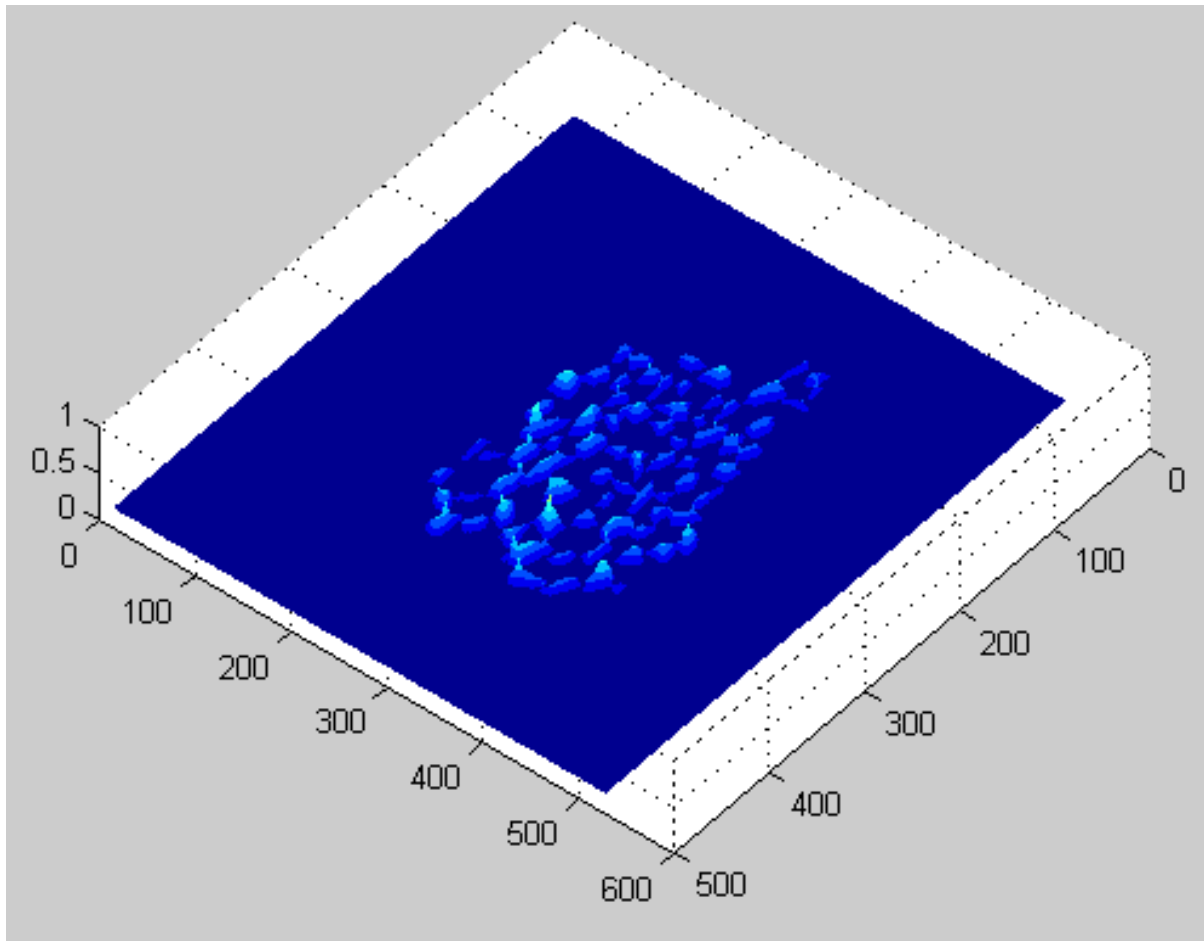
(a) gray scale image



(b) binary image



(c) topographic surface (Top view)



(d) topographic surface (Oblique view)



(e) particle separated image

Figure 5.10 Separation Process

The size of the filter used in the separation process is problem dependent. Larger filters give more accurate detection, but take longer to perform the filtering. Proper size can be determined experimentally. Some “false cutting” can occur for particles whose edge contour is significantly concave on opposite edges.

6. VOLUMETRIC MODELING

6.1 Introduction

Particle size distribution (gradation) in the Superpave and in many other applications is based on the sieve mesh sizes and particle mass. In most sieving operations, gradation is evaluated as “percent-passing” by mass. The minor diameter of the particle profile shape obtained through using principal eigen analysis is used as a particle’s size. This dimension is correlated to the sieve size. In this research, the density is assumed a constant, so the total mass is proportional to the volume of aggregates. Also in this research, all the obtainable information comes from a 2-D image. Volume information is not directly observed. Lack of 3-D information brings the need to estimate the volume using some of the available 2-D measurements, such as area, aspect ratio, signature mean and variance. In other words, modeling the volume of aggregates is needed.

Statistical techniques are important for image analysis. From the images captured of the mineral aggregates, all the sizes and shapes are random. The process of extracting useful information becomes equivalent to estimating random variables. The objective in this chapter is to estimate the volume of mineral aggregates to serve the purpose of gradation.

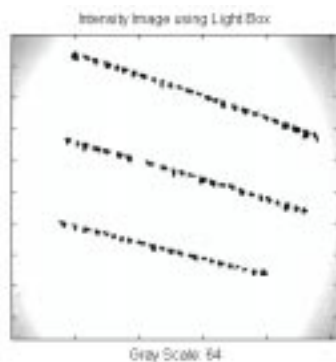
6.2 Modeling Sample Preparation

To observe how particle mass might be correlated with some of its parameters found in 2-D images, some samples of aggregate were collected. Fig. 6.1 demonstrates images of some of these samples. Altogether 501 pieces of limestone rock varying in

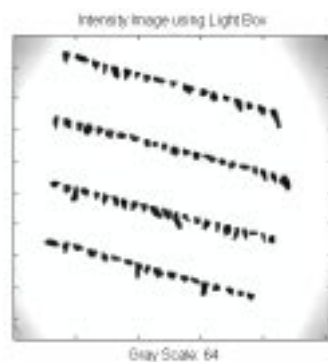
size and shape were imaged. The following measurements were taken for each individual particle:

- Projected area (mm^2)
- Major and minor diameter (mm)
- Aspect ratio
- Non-normalized signature mean (mm) and variance (mm^2)
- Mass (g) and volume (mm^3) with a measured constant density of 0.00305 (g/mm^3)

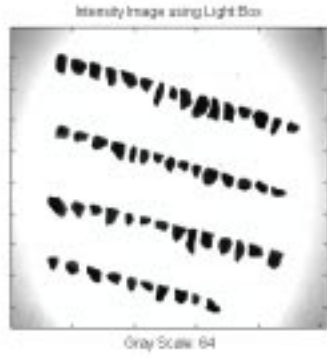
The methods for obtaining above measurements except mass and volume were described in Chapter 4. The mass of each particle was found using a laboratory digital balance, and added to the data vector. All the measurements are listed in Appendix I. The aggregates were arranged on the lighting box as shown in Fig. 6.1 so that each particle could be paired with its image statistics. The particles' sizes are visually judged ranging from 4.75 (mm) to 25.00 (mm).



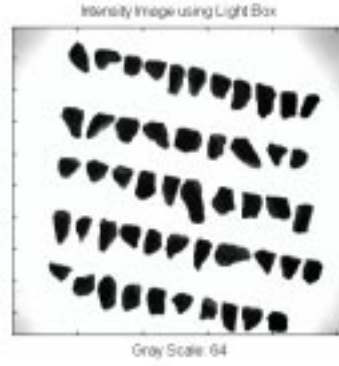
(a) size ≈ 4.75 (mm)



(b) size ≈ 9.50 (mm)



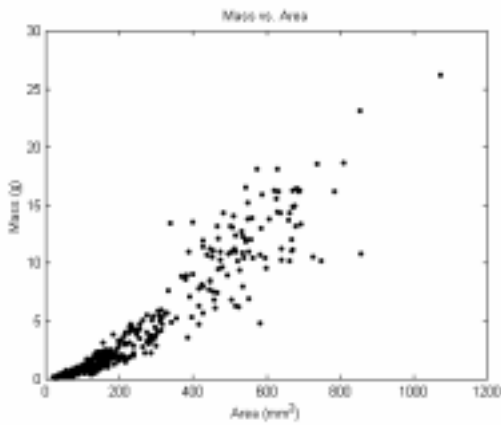
(c) size ≈ 12.50 (mm)



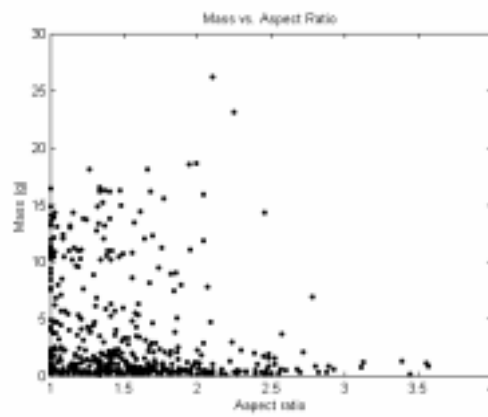
(d) size $\approx 19.00\sim 25.00$ (mm)

Figure 6.1 Sample Photos

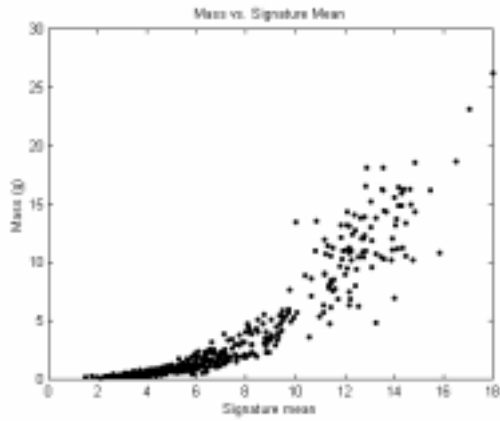
To gain some intuitive perceptions about how some parameters from a particle's 2-D image influence its mass, Fig. 6.2 illustrates the observations in which the mass of each individual particle is plotted against its area, aspect ratio, non-normalized signature mean and variance, major and minor diameter, respectively.



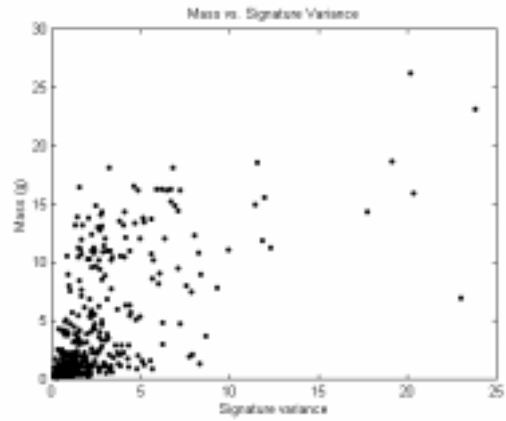
(a) mass vs. area



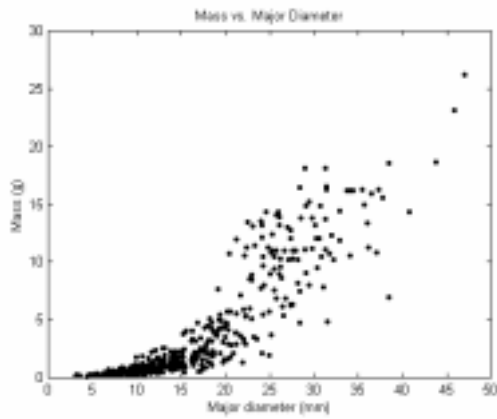
(b) mass vs. aspect ratio



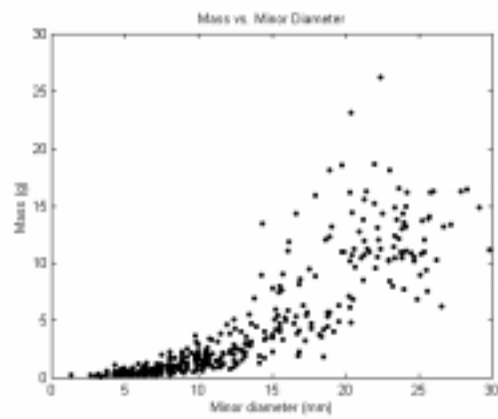
(c) mass vs. signature mean



(d) mass vs. signature variance



(e) mass vs. major diameter



(f) mass vs. minor diameter

Figure 6.2 Sample Data Observations

If coupled with shape information, the particle's projected area can reflect its size. The signature mean is basically the “effective radius”. The projected area and signature mean are apparently the dominant factors that correlate with the mass from both intuitive and experimental considerations. The general trend shows that particle mass value grows as its area and signature mean increase. The aspect ratio gives partial information about the profile shape, but is obviously not correlated directly with mass, at least in this

sample. The signature variance may reveal how irregular the particle shape is, more specifically, how far the actual edge line deviates from the circumference whose radius is the signature mean. Major and minor diameter also indicate particle size.

Evidently, discovering a way to more accurately predict particle's 3-D measurements should be attempted based on combinations of several pertinent 2-D variables. The objective here must be to create a model using appropriate measurements from the image data, so that a “good” model is obtained. A good model will be the one in which the estimated particle volumes and the actual particle volumes are equal, at least when averaged over sufficient number of particles.

6.3 Model Selection

Regression analysis is a statistical technique for modeling the relationship between two or more variables. Once an adequately good model is found, it is then used to predict the response to the new set of variables of the same type. In fact, multiple regression is one of the most widely used statistical techniques [16].

In general, for a dependent variable, or response, y that may be related to k independent variables, the standard multiple linear regression (MLR) model takes form

$$y = \beta_0 + \beta_1 x_1 + \beta_2 x_2 + \dots + \beta_k x_k + \varepsilon \quad (6.1)$$

where

y : Observation or response.

β_j : Partial regression coefficient, $j=0, 1, 2, \dots, k$

x_j : Regressor variable, $j=1, 2, \dots, k$

ε : Random error with zero mean and variance σ^2 .

This model describes a hyperplane in the k -dimensional space of the independent variables $\{x_j\}$. The parameter β_j represents the expected change in the response y per unit change in x_j when all the remaining independent variables x_i ($i \neq j$) are held constant.

It is worth mentioning that, in general, any regression model that is linear in the parameters, that is, the β values, is a linear regression model. Models that are polynomial or include interaction effects in the parameters may also be analyzed by multiple linear regression model by defining regressor variables that include the nonlinear effects [16].

In matrix notation, the model in Eqn. (6.1) can be expressed as

$$\mathbf{Y} = \mathbf{X}\boldsymbol{\beta} + \boldsymbol{\varepsilon} \quad (6.2)$$

Where

$$\mathbf{Y} = \begin{bmatrix} y_1 \\ y_2 \\ \vdots \\ y_n \end{bmatrix} \quad \mathbf{X} = \begin{bmatrix} 1 & x_{11} & x_{12} & \cdots & x_{1k} \\ 1 & x_{21} & x_{22} & \cdots & x_{2k} \\ 1 & x_{31} & x_{32} & \cdots & x_{3k} \\ \vdots & \vdots & \vdots & & \vdots \\ 1 & x_{n1} & x_{n1} & \cdots & x_{nk} \end{bmatrix}$$

$$\boldsymbol{\beta} = \begin{bmatrix} \beta_1 \\ \beta_2 \\ \vdots \\ \beta_k \end{bmatrix} \quad \boldsymbol{\varepsilon} = \begin{bmatrix} \varepsilon_1 \\ \varepsilon_2 \\ \vdots \\ \varepsilon_n \end{bmatrix}$$

The summation of error square is

$$L = \sum_{i=1}^n \varepsilon_i^2 = \boldsymbol{\varepsilon}^T \boldsymbol{\varepsilon} = (\mathbf{Y} - \mathbf{X}\boldsymbol{\beta})^T (\mathbf{Y} - \mathbf{X}\boldsymbol{\beta}) \quad (6.3)$$

The vector of least square estimators, $\hat{\mathbf{a}}$, can be obtained by minimizing L and satisfying

$$\left. \frac{\partial L}{\partial \hat{\mathbf{a}}} \right|_{\hat{\mathbf{a}}} = -2\mathbf{X}^T\mathbf{Y} + 2\mathbf{X}^T\mathbf{X}\hat{\mathbf{a}} = \mathbf{0} \quad (6.4)$$

thus

$$\hat{\mathbf{a}} = (\mathbf{X}^T\mathbf{X})^{-1}\mathbf{X}^T\mathbf{Y} \quad (6.5)$$

The estimated regression model is

$$\hat{\mathbf{Y}} = \mathbf{X}\hat{\mathbf{a}} \quad (6.6)$$

6.4 Particle Geometric Assumptions and Definitions

To use MLR model, the regressor variables that may influence the observations must be found. Reasonably, these variables are particle geometry related.

Referring to Fig. 6.3, some important variables that will relate to the prospective MLR model are defined:

H_{top} : Top height, which is measured from the imaged background up to the highest point found in the upper surface of the particle.

H_{cent} : Central height, which is also measured from the imaged background and through the centroid of the profile shape to the upper surface.

H_{nom} : Nominal height, which is the most related variable. The value of this height quantitatively results from the actual volume of the particle, as illustrated in sub-figure (a), divided by its projected area, as depicted in sub-figure (c). In other words, the actual volume of any particle can be obtained by multiplying its projected area with its nominal height.

D_{maj} : Major diameter of the particle's profile shape.

D_{\min} : Minor diameter of the particle's profile shape.

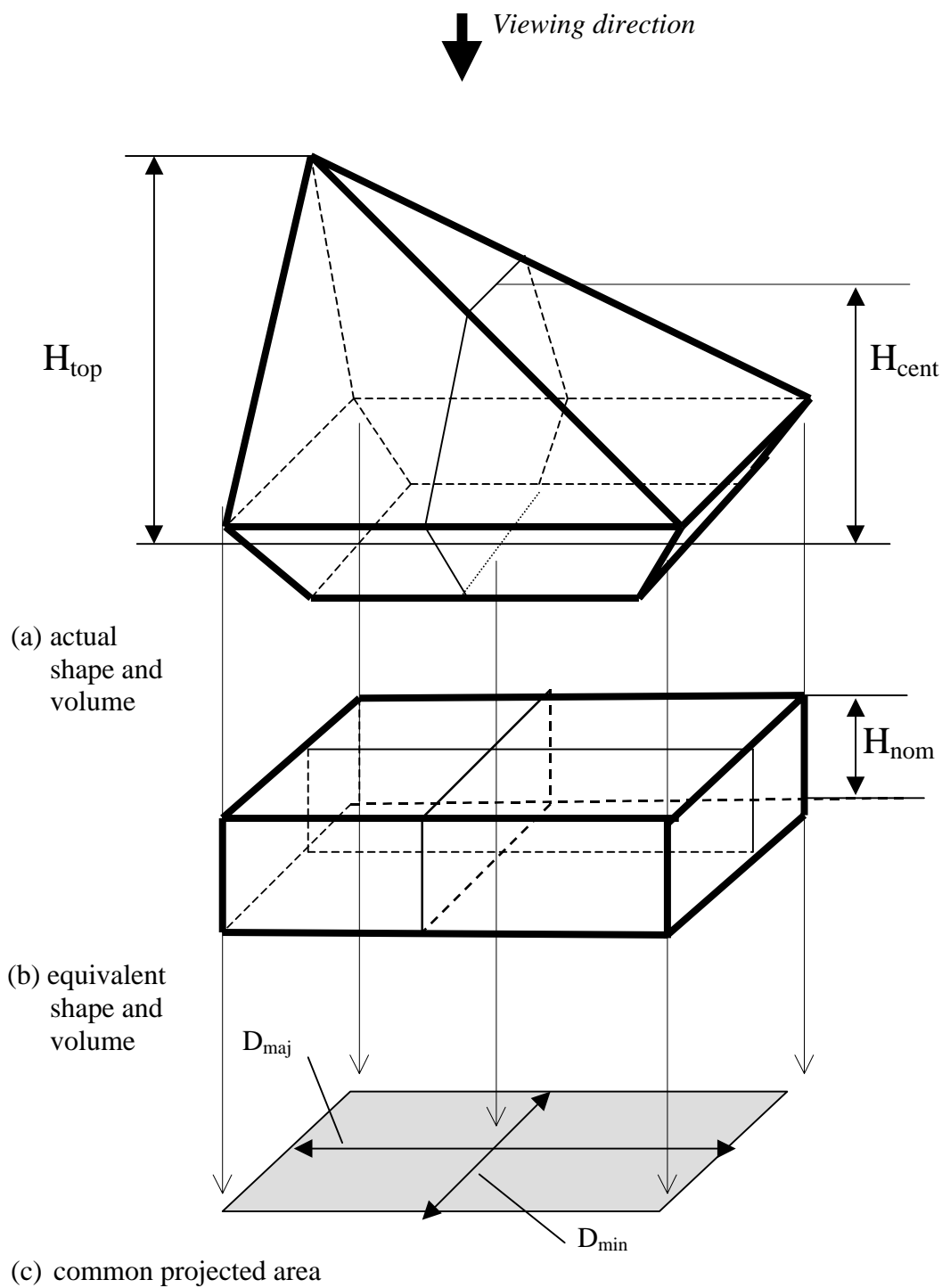


Figure 6.3 Geometric Perspective of Particle

It is clear that the posture of the particles in the imaging scene may affect the modeling results. Here the following assumptions regarding the pattern of particle positioning in the imaged scene are claimed:

1) After randomly vibrating and toppling, the majority of the particles will lie on the background with their maximum projected area facing down. This state is termed “stable state” hereafter.

2) All particles are assumed to have a constant density.

The assumption 1) can lead to the following inequalities:

For any geometric objects, at the stable state

$$0 < H_{nom} \leq H_{cent} \leq H_{top} \leq D_{min} \quad (6.7)$$

While for the most crushed limestone aggregates at the stable state, it holds

$$0 < H_{nom} \leq D_{min} \quad (6.8)$$

thus

$$0 < \frac{H_{nom}}{D_{min}} \leq 1 \quad (6.9)$$

The term $\frac{H_{nom}}{D_{min}}$ is defined as the flatness of particle throughout this work.

6.5 MRL Model Building

Flatness of the particle is suspected to relate to some geometric attributes, such as elongation, roundness of the profile shape, and jaggedness of the edge line. All the mentioned variables are defined to be particle size and volume independent.

Following MLR model is build first, then each variable in it is described thereafter.

$$\frac{H_{nom}}{D_{min}} = \beta_0 + \beta_1 \frac{D_{maj}}{D_{min}} + \beta_2 \frac{D_{min}}{2M_{sig}} + \beta_3 \left(-\log \left(\frac{V_{sig}}{M_{sig}^2} \right) \right)^{-1} + \varepsilon \quad (6.10)$$

where

H_{nom} : Nominal height (mm).

D_{min} : Minor diameter (mm).

D_{maj} : Major diameter (mm), also as defined in Chapter 4.

M_{sig} : Mean value of the non-normalized signature (mm).

V_{sig} : Variance of the non-normalized signature (mm^2).

ε : Random error.

Definition and interpretation of each variable in Eqn. (6.10) are as follows:

$\frac{H_{nom}}{D_{min}}$: Flatness, as illustrated in Fig. 6.4 (a).

$\frac{D_{maj}}{D_{min}}$: Elongation. It takes the value of aspect ratio, as depicted in Fig. 6.4 (b).

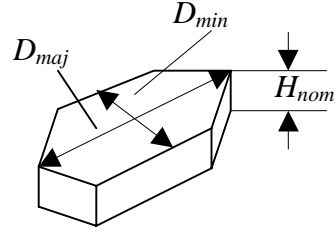
$\frac{D_{min}}{2M_{sig}}$: Roundness. It measures the circularity of the particle. Its value increases

to 1 as the profile shape of the particle becomes more circular. See Fig.

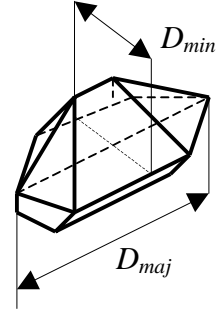
6.4 (c).

$\frac{V_{sig}}{M_{sig}^2}$: Jaggedness. For a perfectly smooth edge line, the value is zero, as

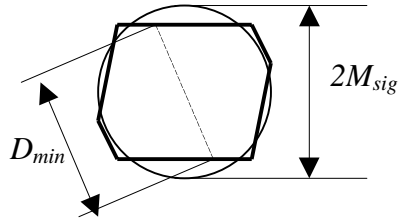
demonstrated in Fig. 6.4 (d).



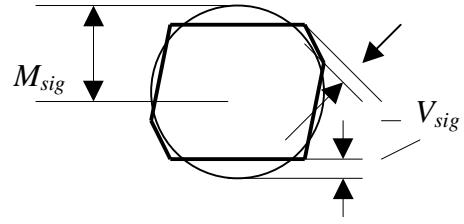
(a) flatness: $\frac{H_{nom}}{D_{min}}$



(b) elongation: $\frac{D_{maj}}{D_{min}}$



(c) roundness: $\frac{D_{min}}{2M_{sig}}$



(d) jaggedness: $\frac{V_{sig}}{M_{sig}^2}$

Figure 6.4 Interpretation of Model Variables

Some aspects regarding $\frac{V_{sig}}{M_{sig}^2}$ need to be mentioned here: first, the signature mean is squared in the denominator to make the parameter dimensionless. Second, the logarithm transformation of $\frac{V_{sig}}{M_{sig}^2}$ makes the very small ratio values more readable and offsets the possible inaccuracy caused by numerical truncation in the computer system. Third, the reciprocity of the negative logarithm transformation ensures a positive value that decreases to zero as the edge line becomes smoother. To clearly demonstrate the

purpose of this data transformation, given a array of small (not very small in order to view the plots effectively) values, starting from 0.01 up to 0.33, increasing step by 0.04, Fig. 6.5 shows values of the logarithm transformation of this array, and the final values of the negative reciprocity of this transformation.

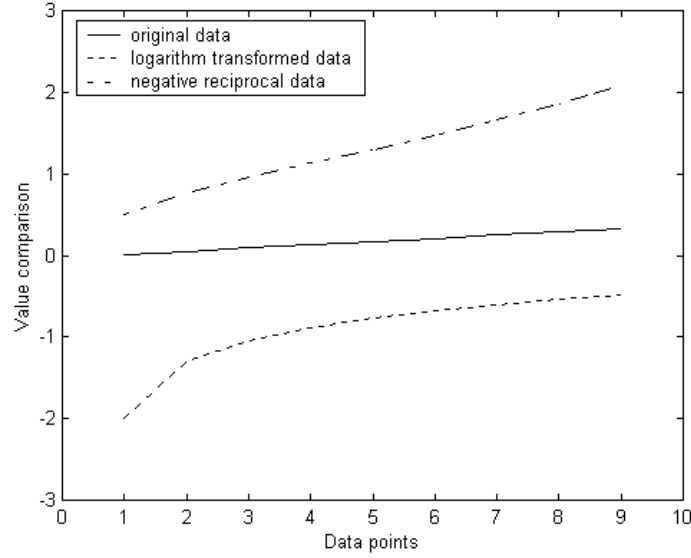


Figure 6.5 Data Transformation

The model in Eqn. (6.10) can be simplified, correspondingly, as

$$Y_{flat} = \beta_0 + \beta_1 X_{elong} + \beta_2 X_{round} + \beta_3 X_{jagged} + \epsilon \quad (6.11)$$

where X_{elong} , X_{round} and X_{jagged} are equivalent to the corresponding regressor variables in Eqn. (6.10).

In matrix notation,

$$\mathbf{Y}_{flat} = \hat{\mathbf{a}} \mathbf{X} + \epsilon \quad (6.12)$$

The unbiased regression coefficient estimators are thus in matrix form

$$\hat{\mathbf{a}} = (\mathbf{X}^T \mathbf{X})^{-1} \mathbf{X}^T \mathbf{Y}_{flat} \quad (6.13)$$

The prediction of flatness for each particle is

$$\hat{Y}_{flat} = \hat{\beta}_0 + \hat{\beta}_1 X_{elong} + \hat{\beta}_2 X_{round} + \hat{\beta}_3 X_{jagged} \quad (6.14)$$

where

$$\hat{Y}_{flat} = \frac{\hat{H}_{nom}}{D_{min}} \quad (6.15)$$

Recall that the final goal is to use this model to predict the volume of the particle. Since the volume estimate used in this research equals the projected area multiplied by corresponding nominal height, the following expression holds:

$$\hat{V} = \hat{H}_{nom} A_{part} = \hat{Y}_{flat} D_{min} A_{part} \quad (6.16)$$

where

A_{part} : Particle projected area (mm^2).

6.6 Overall Modeling Effect

Using all the available data from the modeling sample of 501 particles, the complete model in Eqn. (6.10) was found to be:

$$\frac{\hat{H}_{nom}}{D_{min}} = 0.6660 - 0.1390 \frac{D_{maj}}{D_{min}} - 0.4754 \frac{D_{min}}{2M_{sig}} + 0.4668 \left(-\log \left(\frac{V_{sig}}{M_{sig}^2} \right) \right)^{-1} \quad (6.17)$$

From Eqn. (6.14) and Eqn. (6.15), Eqn. (6.16) can be rewritten as

$$\hat{V} = \hat{\beta}_0 A_{part} D_{min} + \hat{\beta}_1 A_{part} D_{min} X_{elong} + \hat{\beta}_2 A_{part} D_{min} X_{round} + \hat{\beta}_3 A_{part} D_{min} X_{jagged} \quad (6.18)$$

Now, further define

$$X_0^* = A_{part} D_{min}$$

$$X_{elong}^* = A_{part} D_{min} X_{elong}$$

$$X_{round}^* = A_{part} D_{min} X_{round}$$

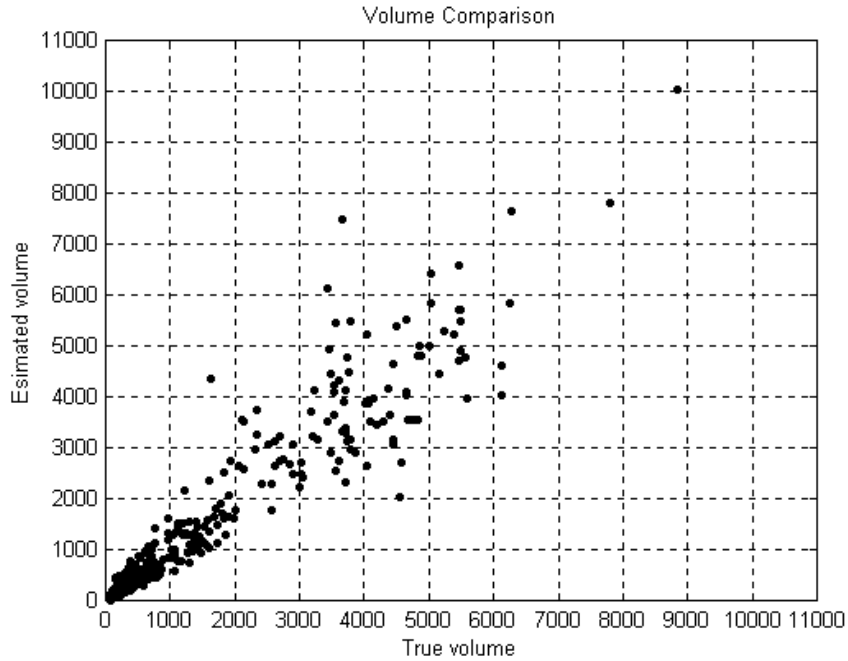
$$X_{jagged}^* = A_{part} D_{min} X_{jagged}$$

Thus, Eqn. (6.18) becomes

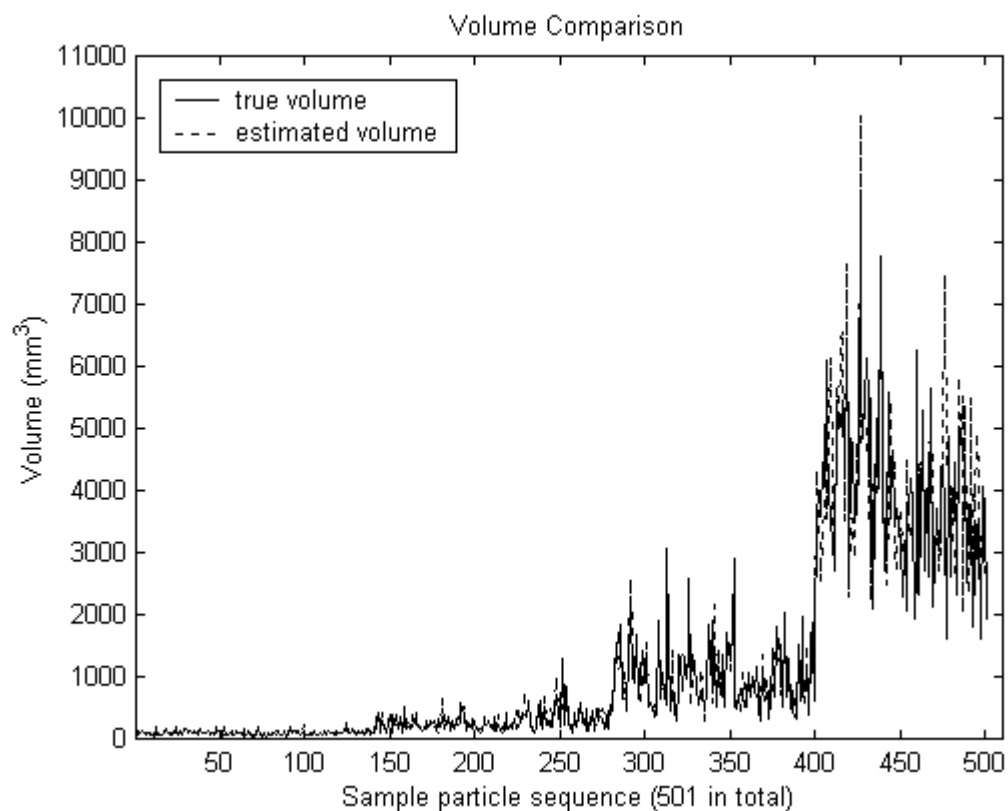
$$\hat{V} = \hat{\beta}_0 X_0^* + \hat{\beta}_1 X_{elong}^* + \hat{\beta}_2 X_{round}^* + \hat{\beta}_3 X_{rough}^* \quad (6.19)$$

with the same $\hat{\mathbf{a}}$ values as obtained.

Fig. 6.6 shows the overall modeling effect, i.e., comparison of estimated and true volume. Fig. 6.7 zooms in on the constituent parts of the plot in Fig. 6.6 (b) for better viewing.

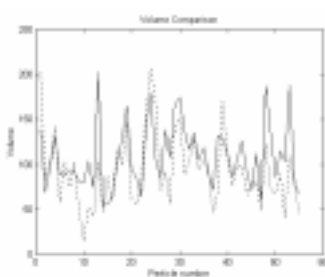


(a)

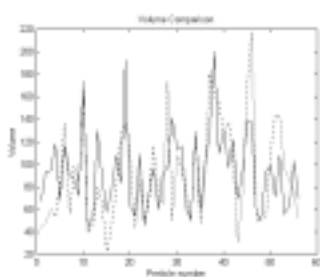


(b)

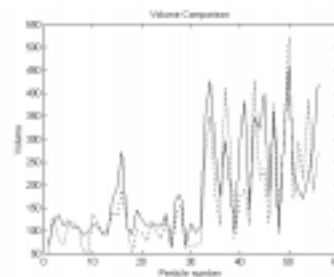
Figure 6.6 Volume Comparison



(a) particle #1~#55



(b) particle #56~#110



(c) particle #111~#165

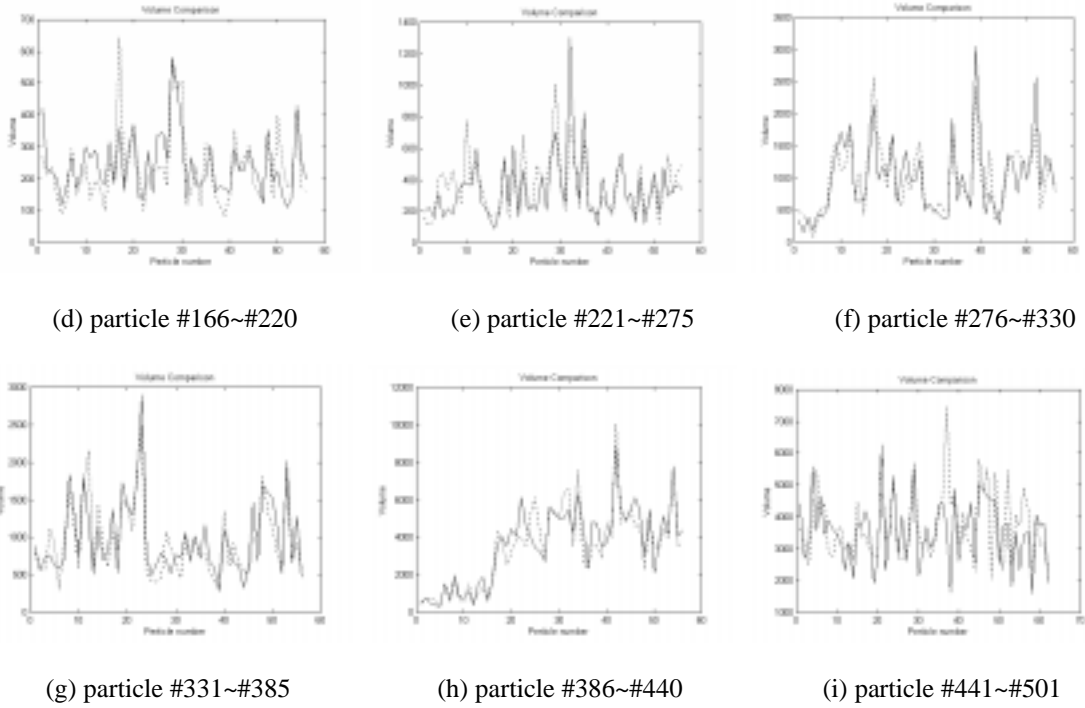


Figure 6.7 Modeling Effect Observation

6.7 Model Adequacy

To simplify the statistical analysis of the model, Eqn. (6.19) is treated as an approximated standard MLR model with zero intercept. A number of techniques can be used to measure the adequacy of a multiple regressor model [16]. Two of those techniques to present the adequacy of the model were used. The pertinent theoretical basis can be reviewed in the book by Hines and Montgomery [16] and Myers [18].

6.7.1 The Coefficient of Multiple Determination

The coefficient of multiple determination, in a loose sense, is a measure of the amount of reduction in the variability of the response obtained by using the regressor

variables [16], is defined in the problem as

$$R^2 = 1 - \frac{SS_E}{S_{vv}} \quad (6.20)$$

where

$$SS_E = \mathbf{\hat{a}}^T \mathbf{\hat{a}} = \sum_{i=1}^{n=501} \left(\hat{V}_i - V_i \right)^2 \quad (6.21)$$

$$S_{vv} = \sum_{i=1}^{n=501} \left(V_i - \bar{V} \right)^2 = \mathbf{V}^T \mathbf{V} - \frac{\left(\sum_{i=1}^{n=501} V_i \right)^2}{n} \quad (6.22)$$

where SS_E is the sum of squares for error, and S_{vv} is the sum of squares.

For the modeling sample of 501 particles, it was calculated that $SS_E = 118075237$, $S_{vv} = 1257933386$, thus $R^2 = 0.91$. This indicates that about 91% of the variability in the actual volume V has been explained when the three regressor variables are used in the model.

6.7.2 Error Normality

One of the assumptions for fitting a regression model is that the errors are uncorrelated random variables and normally distributed with mean zero and constant variance, i.e., $NID(0, \sigma_e^2)$. Fig. 6.8 shows the errors plotted against the particle sequence. Note that it follows the same particle sequence as that used in Fig. 6.6.

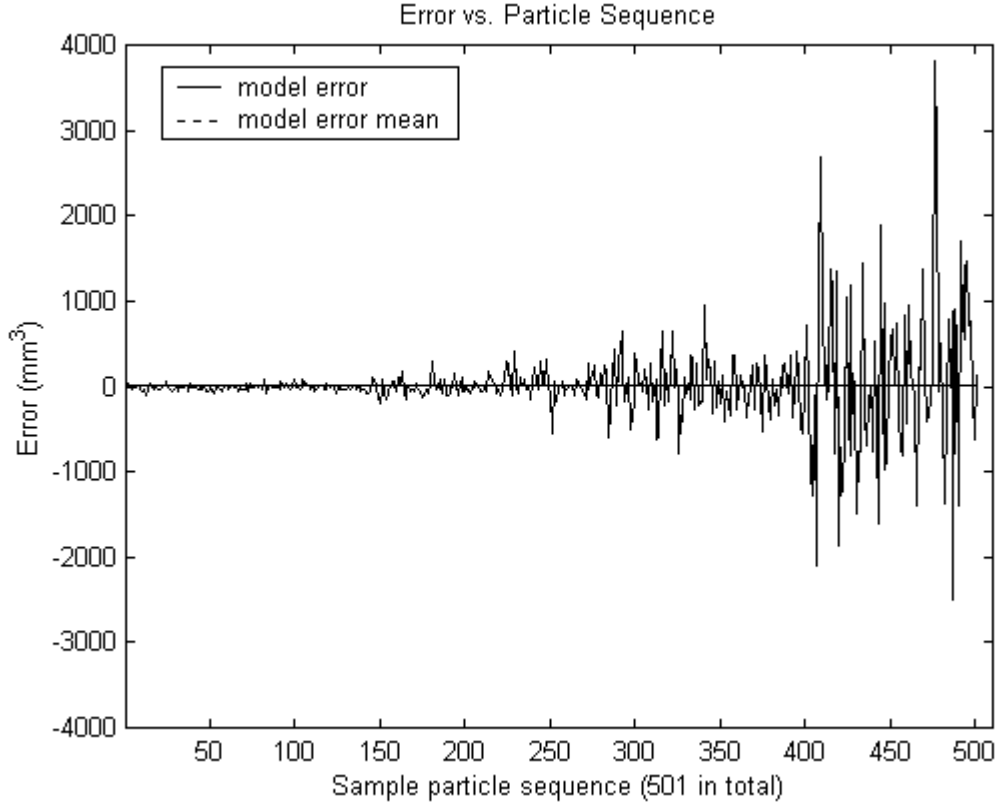


Figure 6.8 Model Error vs. Particle Sequence

To test the normality of the residual which is the difference between actual volume and estimated volume, one may standardize the residuals by computing the quantity

$$d_i = \frac{\varepsilon_i}{\sqrt{MS_E}} \quad (6.23)$$

where $i=1,2,3,\dots, n$

MS_E : mean squares, and

$$E(MS_E) = \sigma_e^2 \quad (6.24)$$

where $E(\bullet)$ denotes the expectation, and σ_e^2 is the error variance [16].

If the error are $NID(0, \sigma_e^2)$, then approximately 95% of the standardized residuals should fall in the interval $(-2,2)$. Fig. 6.9 presents the histogram of the d_i 's for the sample.

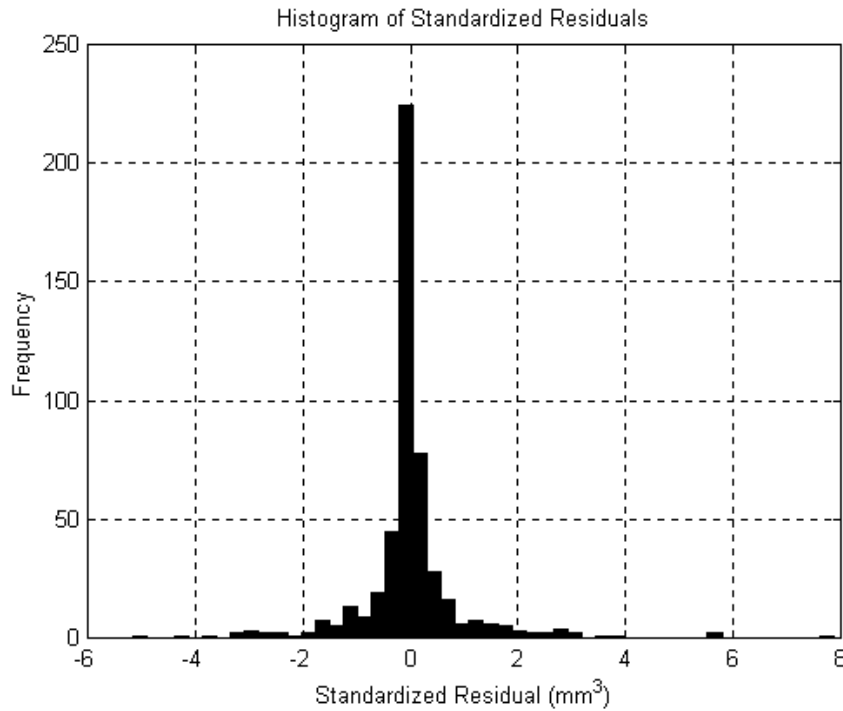


Figure 6.9 Histogram of Standardized Residuals

The percentage of the resultant standardized residuals that are within $(-2,2)$ is found to be 94.01 %, the errors can thus be regarded as being distributed normally.

6.8 Model Testing

The quality of the developed volumetric model needs to be tested using the randomly selected samples. If the sample population satisfies the size range (minor diameter is between 4.75 mm and 25.00 mm), it is reasonable to expect a satisfactorily accurate result.

6.8.1 Preparation of Testing Sample Population

Due mainly to the size constraints of the lighting box on which the particles are placed, the number of particles in an image is limited. Eight batches of testing sample were prepared. Particles in each batch were then placed in the imaging scene and were photographed. The same particles were photographed five times. Each time the particles were “stirred up” to give a completely new image. The five images of each batch were marked with *a, b, c, d, e* respectively for analysis, thus there were 40 total images in the sample.

To test the model, one out of five images from each sample batch was randomly selected. The statistics of the each batch are tabulated in Table 6.1. The histograms of some useful measurements for each and for the combined batch are included in Appendix II. The total actual mass of the each batch is obtained by weighing.

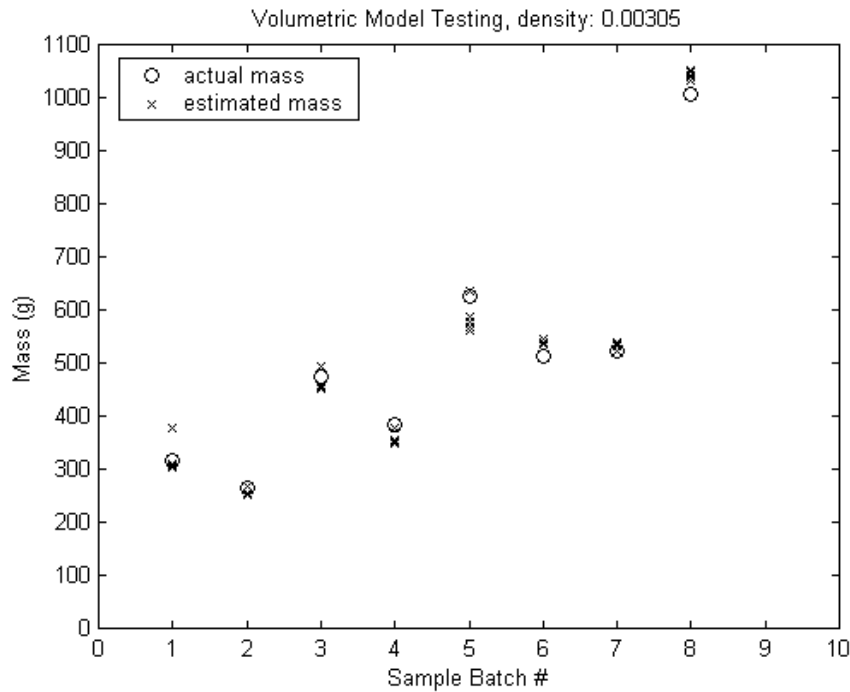
Table 6.1 Sample Measurement Statistics

Batch / Image #	Total particle #	Total true mass (g)	Area mean (mm^2)	Area STD ⁺ (mm^2)	Major diameter mean (mm)	Major Diameter STD ⁺ (mm)	Minor diameter mean (mm)	Minor Diameter STD ⁺ (mm)
#1 / b	345	316.25	96.3661	40.0473	11.4350	3.0401	7.8602	2.2699
#2 / a	376	265.91	75.2003	38.4560	9.8945	3.4555	6.5525	2.1892
#3 / e	215	475.06	169.2037	81.5658	15.4329	4.7307	10.8713	3.6119
#4 / d	251	383.46	125.3001	75.1036	13.1246	4.4820	8.8168	3.6209
#5 / a	378	625.52	128.0232	78.6642	13.1727	5.0281	8.8973	5.9956
#6 / a	76	512.02	362.9582	197.1795	23.5464	7.7220	16.1730	5.3785
#7 / c	71	521.38	376.1573	204.8211	23.1580	7.3076	17.3936	6.2691
#8 / e	150	1006.19	356.2143	206.9573	22.5798	8.0629	16.2522	6.1154

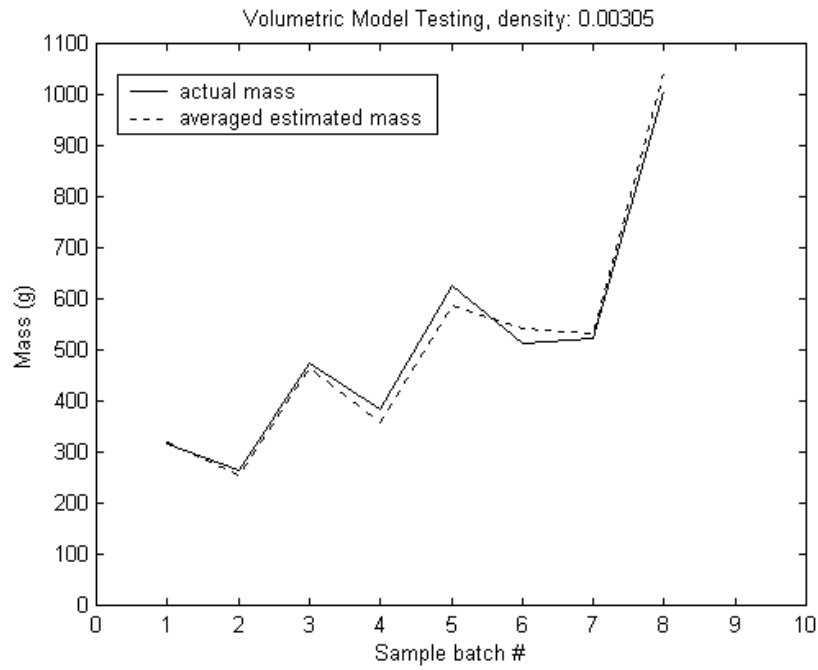
STD⁺ : Standard deviation.

6.8.2 Testing Results

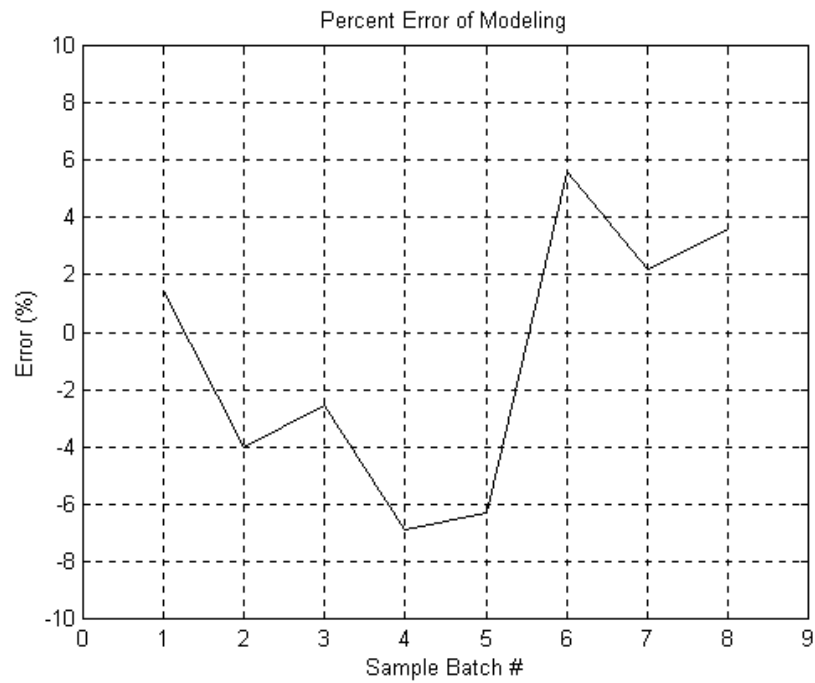
For five images from the same batch, eight batches in total, using the volumetric model and the same density used before to compute the estimated mass, sub-figure (a) shows the estimated mass of each image from batch #1 to #8. So, for a single batch, every five mass estimates are plotted versus one actual mass. In (b), for each batch, averaging these five estimated mass values as a data point, then plot them against the actual mass. (c) demonstrates the percent error from (b).



(a) mass comparison



(b) mass comparison



(c) percent error

Figure 6.10 Model Testing for Mass

From sub-figure (c), it is observed that the percent error can reach as high as around $\pm 6\%$ for batch #4, #5 and #6. If the size of the population N is increased, the accuracy can then be improved. To do this, take a random combination of the images, and each image of the combination was randomly selected from one of the eight batches. This indicates that the total number of particles will increase up to $N=1862$, which is a total particle number of eight batches. Fig. 6.11 illustrates such a random combination formed by image b, a, d, e, c, e, c, d from the sample batch #1, #2, ... #8, respectively.

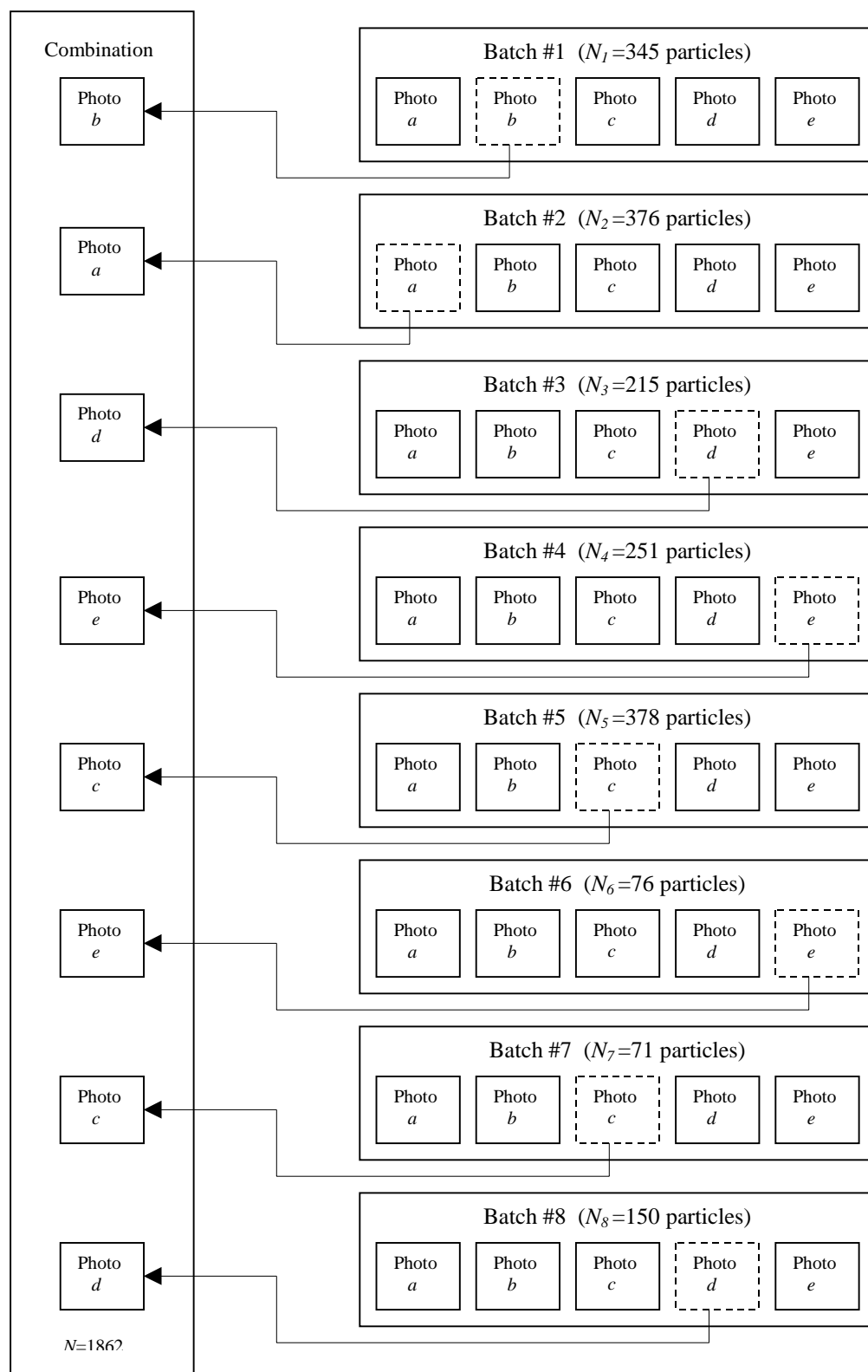


Figure 6.11 A Random Combination of Sample Batches (*badececd*)

100 combinations were tested. Each combination may represent one “grand” image covering all 1862 particles. Each new constituent image results from a new “stir-up”, and in total 100 stir-ups were conducted for producing 100 grand images. The result is shown in Fig. 6.12. Fig. 6.13 shows the percent error, which mainly stays within $\pm 2\%$, and is greatly reduced as anticipated.

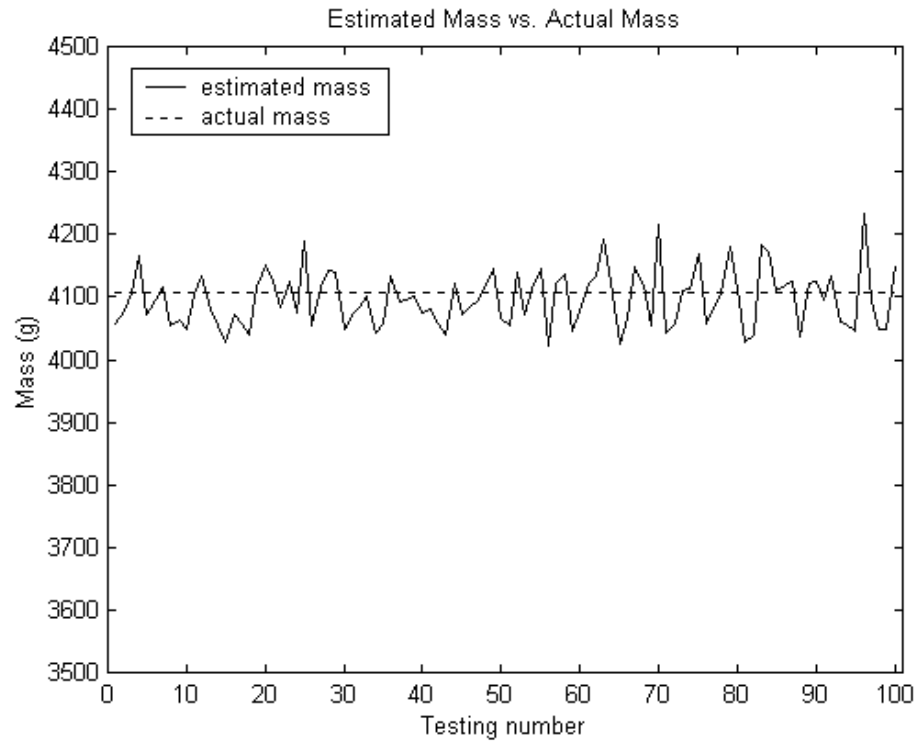


Figure 6.12 Modeling Result for 100 Combinations

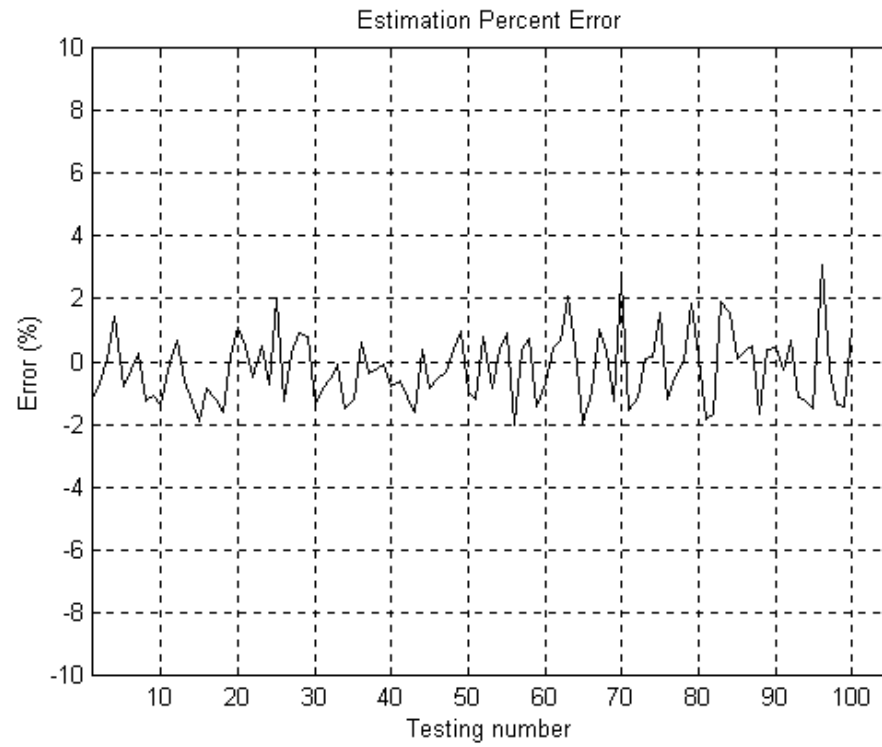


Figure 6.13 Percent Error for 100 Combinations

7. SIEVING CORRELATION

7.1 Introduction

Since the Superpave specifications are given on the basis of percent passing by mass, two correlations must be made. First, particles are optically sieved into “bins” or sizes based on the minor dimension of the particle. In each bin, the number of particles is not important, rather, the total mass of the particles in that bin is. Second, particle’s mechanical sieving behavior must be correlated with the optical sieving behavior. The model which correlates information obtained from the 2-D image to the volume has been established. In this chapter, a sieving correlation method was developed by first modeling the particle cross section into a rectangle, plus the scaling factors obtained from calibration to take the actual cross section shape and other related elements into account. Based on the flatness distribution from 501 sample particles, a criterion was set to determine the sieving strategy for each particle. Results are presented as gradation curves in the format used for Superpave analysis. The optical sieving results were also compared against mechanically sieved measurements of the same samples to test accuracy. The results showing satisfactory correspondance were presented.

7.2 Identified Sieving Problems

Either a circular sieve opening or a cylindrical particle as shown in Fig. 7.1 (a) will make the sieving process easy to describe analytically. In either case, the fashion in which the particles fall through the sieve opening is rotation invariant in the falling direction. Unfortunately, neither the sieve opening shape nor the cross section of the particle is circular. Sieve openings are square, and the cross section of crushed particles

is randomly shaped as illustrated in Fig. 7.1 (b). This makes the sieving analysis rather complex.

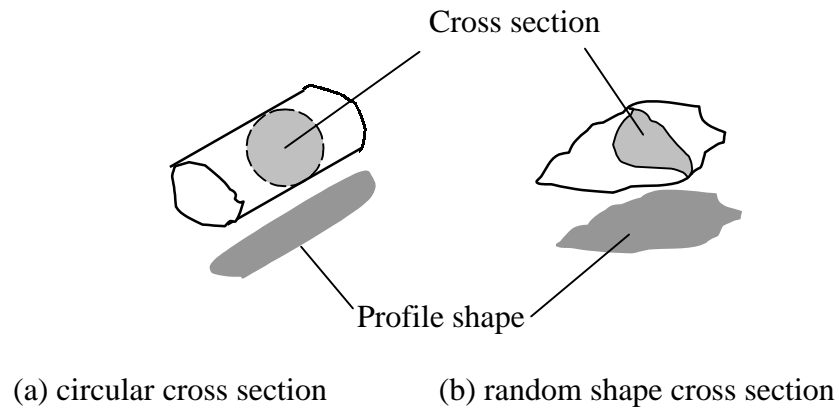


Figure 7.1 Particle Cross Section Shape

For example, for a fairly flat particle with 22 *mm* minor diameter, it is clear that it can not pass if its minor diameter is parallel to the square sieve opening of 19.00 *mm*. However, after rotating a certain angle α , it becomes passable since 22 *mm* is smaller than the diagonal (26.87 *mm*) of the square opening, as shown in Fig.7.2. There is a tendency for flat particles, especially those with rounded edges to pass diagonally through the sieve.

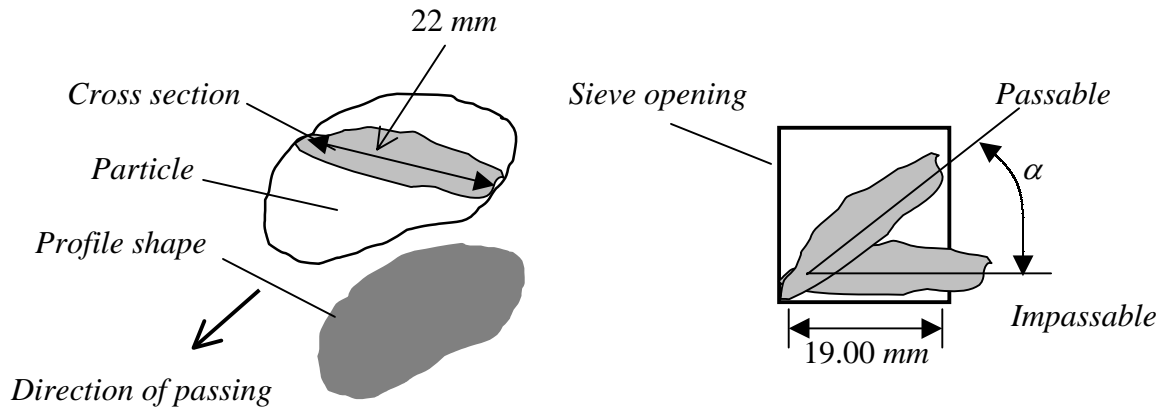


Figure 7.2 Particle Passing Mechanism

In vision sieving, the particle minor diameter is approximately known, but particle thickness is not, and the thickness is undoubtedly a critical factor that influences particle sieving behavior. This requires development a method for relating the 2-D observable features to the sieving behavior of particles. It will probably be impossible to do this with extreme accuracy for individual particles. However, it is expected that reasonably accurate results for bulk measurements should be obtained.

7.3 Analytical Discussion

To simplify the complexity of the sieving behavior problem, the interaction between the particle cross section and the square mesh of a given sieve was first analytically modeled. Let d_{sv} be the size of a given sieve, and as defined previously, D_{min} be the minor diameter, and H_{nom} be the nominal height. This way the cross section takes the shape of a rectangle, as illustrated in Fig. 7.3.

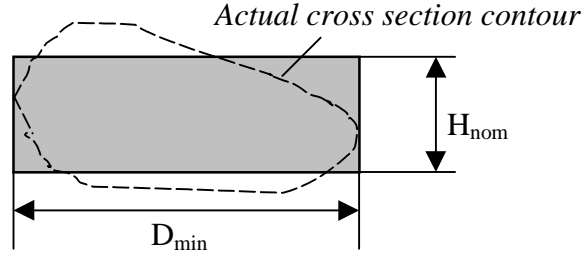


Figure 7.3 Modeled Particle Cross Section

The interaction of the cross section with the sieve size takes place only for those particles whose minor diameters are within the range $d_{sv} < D_{min} < \sqrt{2} d_{sv}$. The reason that the equal sign “=” was not included is that, if particle minor diameter equals the sieve size, it is expected to pass, while if it has the same dimension as the diagonal of square mesh, it will be retained with certainty, since particles are not “razor thin”.

Given a sieve mesh size d_{sv} , the critical position for a particle with assumed rectangular cross section of minor diameter D_{min} and nominal height H_{nom} to pass or be retained in the sieve is illustrated in Fig. 7.4.

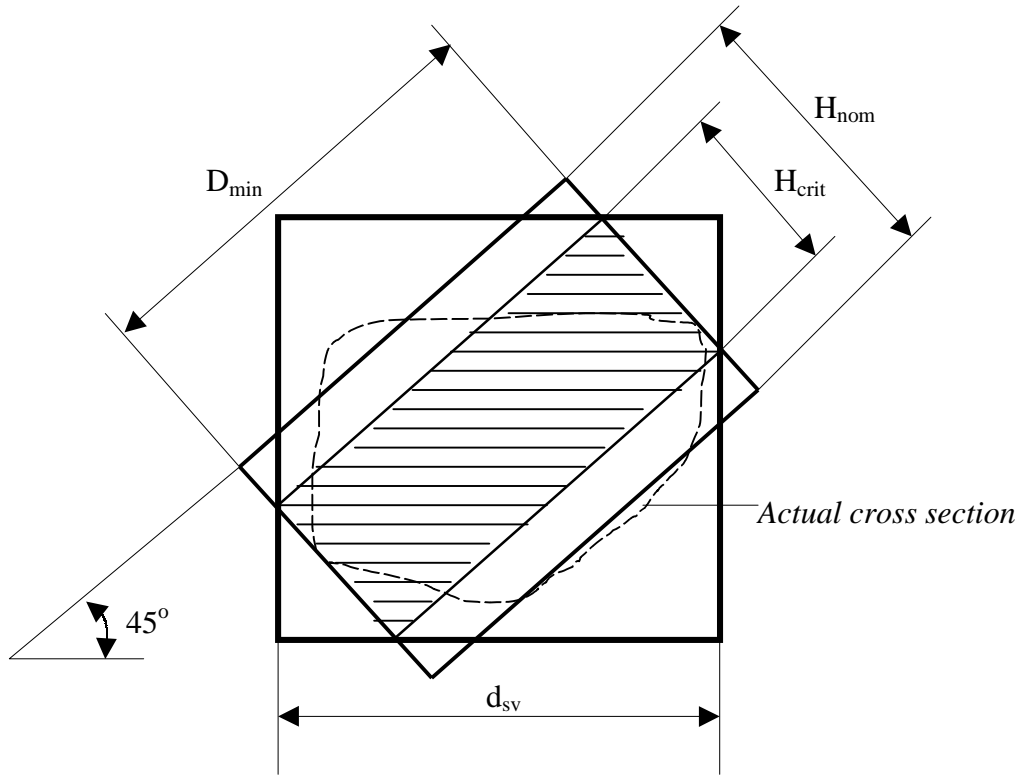


Figure 7.4 Critical Position

For any given minor diameter D_{min} satisfying $d_{sv} < D_{min} < \sqrt{2} d_{sv}$, it has a “critical height”, denoted as H_{crit} in above figure. The hatched rectangle is correspondingly formed by D_{min} and H_{crit} , as also shown in above figure. If the nominal height H_{nom} is shorter than H_{crit} , the particle passes this sieve, otherwise it is retained. The following simple relation holds for H_{crit} and D_{min} :

$$H_{crit} = \sqrt{2} d_{sv} - D_{min} \quad (7.1)$$

Two special cases determine the range of H_{crit}

- i) if $D_{min} = \sqrt{2} d_{sv}$, then $H_{crit} = 0$. This means that unless the particle is “razor thin”, it will be retained on the sieve. Particles with this D_{min} will always be retained in practice.
- ii) if $D_{min} = d_{sv}$, then $H_{crit} = 0.4142 D_{min}$. Particles with this D_{min} will be expected to pass the sieve.

From i) and ii), the range of the critical height is thus

$$0 < H_{crit} < 0.4142 D_{min} \quad (7.2)$$

Recall that the flatness of the particle is defined as

$$Y_{flat} = \frac{H_{nom}}{D_{min}} \quad (7.3)$$

and further define the *critical flatness* for a particle of D_{min} as

$$Y_{crit} = \frac{H_{crit}}{D_{min}} \quad (7.4)$$

Apparently, the state of any particle of D_{min} in the sieve can be determined by the following conditions:

$$\begin{cases} \text{if : } Y_{flat} \leq Y_{crit}, \text{ pass} \\ \text{if : } Y_{flat} > Y_{crit}, \text{ retained} \end{cases} \quad (7.5)$$

One may argue that for the crushed limestone aggregates, the shapes of the cross section are not rectangular, so the conditions set in inequality (7.4) are not sufficient to determine a particle’s passing or being retained. To remedy this, a calibration factor is obtained experimentally and added to correct the above conditions, as described later .

7.4 Sieving Probability Analysis

For any particle with D_{min} in a sieve, the conditions expressed in inequality (7.5) are fundamental for judging its ultimate state: passing or being retained. From Eqn. (7.1) and (7.4), the corresponding critical flatness can thus be easily obtained as

$$Y_{crit} = \sqrt{2} \frac{d_{sv}}{D_{min}} - 1 \quad (7.6)$$

Now the question arises: what is the flatness, Y_{flat} , of the particle of interest?

The sample of 501 particles was analyzed to determine the probability distribution of the particle flatness. Fig. 7.5 and Fig. 7.6 present a scatter diagram and a histogram of the sample flatness statistics.

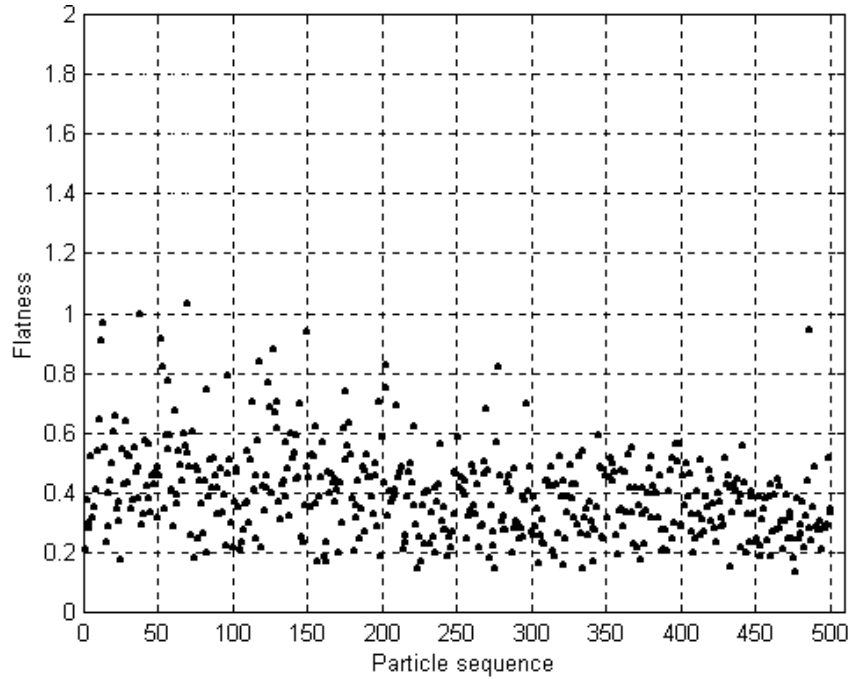


Figure 7.5 Scatter Diagram of Sample Flatness

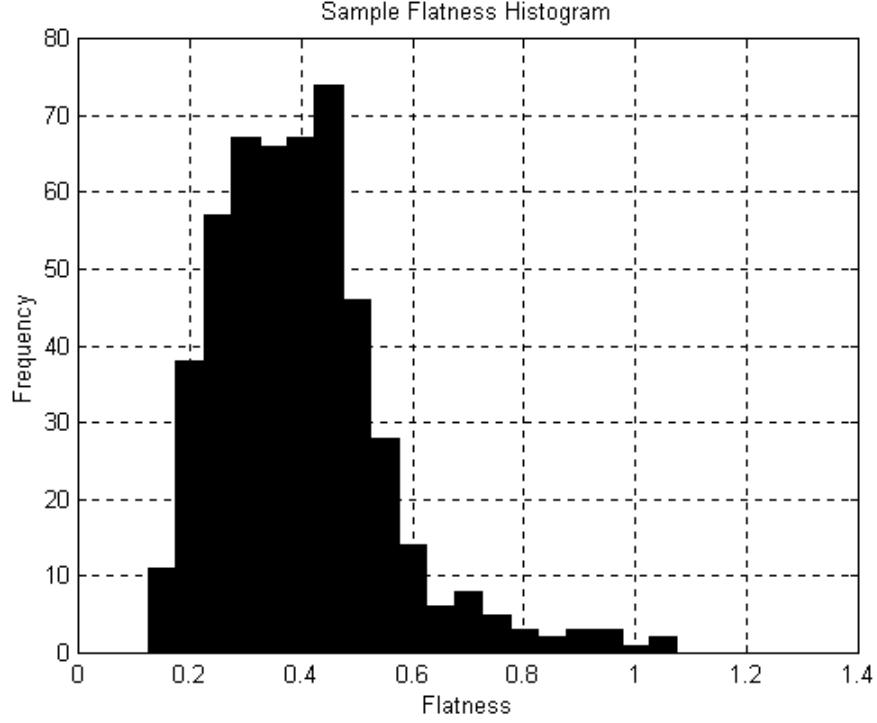


Figure 7.6 Sample Flatness Histogram

The cumulative distribution of the 501 sample particles is obtained from the probability density data. Its approximated distribution function is attained by applying a curve-fitting technique, shows as the solid curve in Fig. 7.7. The distribution function is approximated as

$$P(Y_{crit}) = -19.9524 Y_{crit}^5 + 67.41075 Y_{crit}^4 - 83.6898 Y_{crit}^3 + 44.4792 Y_{crit}^2 - 7.6510 Y_{crit} + 0.4069 \quad (7.7)$$

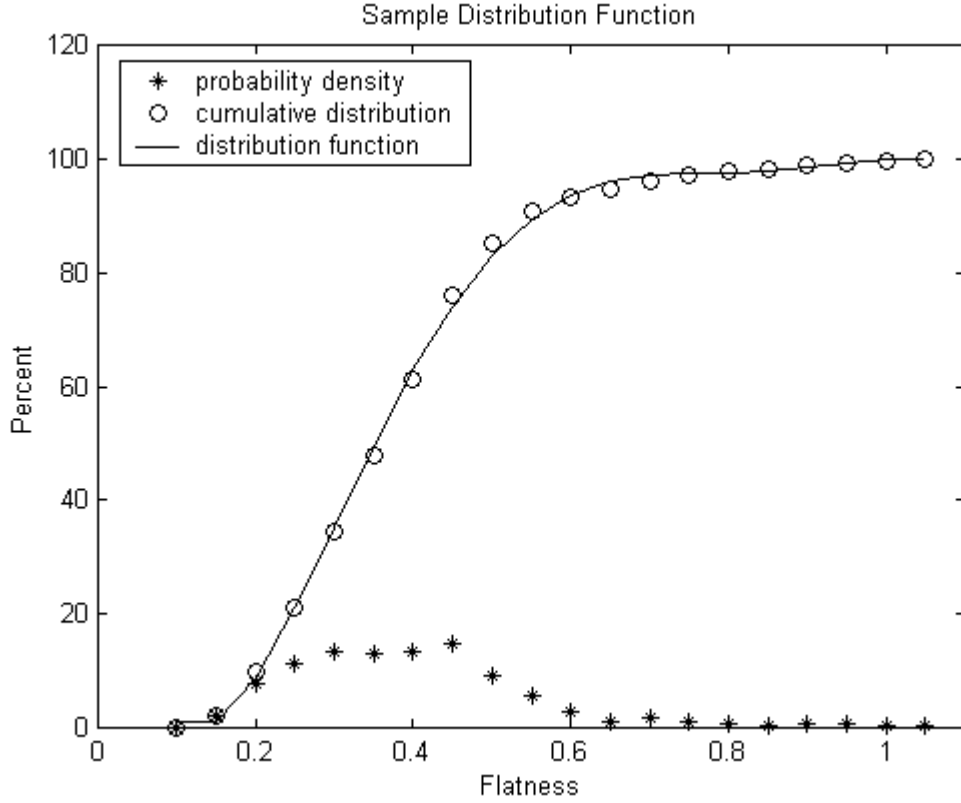


Figure 7.7 Sample Flatness Distribution

The strategy for using the function in Eqn. (7.7) is straightforward:

- 1) Given the particle's measured minor diameter D_{min} , select those particles for

which $d_{sv} < D_{min} < \sqrt{2} d_{sv}$.

- 2) Calculate the H_{crit} .
- 3) From the cumulative probability distribution function in Eqn. (7.7), calculate

$$P^* = \{P(Y_{flat}) \leq Y_{crit}\} \quad (7.8)$$

where $P(\bullet)$ indicates probability.

- 4) Create a random number η on $[0,1]$ using a uniform distribution.
- 5) If $\eta \leq P^*$, the particle passes. Otherwise it is retained.

This approach makes no attempt to determine analytically whether an individual particle passes or is retained. Rather, it exploits the central tendency of the data to provide an estimate which proves to be fairly accurate over a large sample.

For the sake of convenience, rewrite inequality (7.5) which are the conditions for sieving behavior.

$$\begin{cases} \text{if : } Y_{flat} \leq Y_{crit}, \text{pass} \\ \text{if : } Y_{flat} > Y_{crit}, \text{retained} \end{cases} \quad (7.9)$$

Recall that inequalities expressed in (7.9) are based on the assumption that the particle has rectangle shaped cross section which is not true in reality. Also, the conditions in (7.9) is for analytical determination whether an individual particle passes or is retained. At this point, the analytical determination for an individual particle has been converted to statistical determination for a group of particles. This fact imposes an additional modification to P^* to compensate for inaccuracies caused by irregular shaped cross section. Referring to the steps in using sample flatness distribution function stated previously, multiply P^* by a scaling factor called *sieving calibration factor*, ζ_{sv} , where $\zeta_{sv} \geq 1.00$. Then conditions for sieving behavior becomes

$$\begin{cases} \text{if : } \eta \leq \zeta_{sv} P^*, \text{pass} \\ \text{if : } \eta > \zeta_{sv} P^*, \text{retained} \end{cases} \quad (7.10)$$

where ζ_{sv} can be calibrated experimentally for the given sieve size.

7.5 Sieving Phase Analysis

7.5.1 Size Modification for Triangular Shapes

The minor diameter of the shape is regarded as the size that determines the sieving behavior. For triangular shaped particles as shown in Fig. 7.8, however, the

actual sieve size will be greater than the minor diameter, to an extent that may vary according to the actual shape. This requires to sort out those triangle shapes, and modify the minor diameter that is the most vital element to determine passing or staying on a given sieve.



Figure 7.8 Triangle Shaped Particles

Rather than determine the modifying extent for each triangular particle, the minor diameter is multiplied by a correction factor, which can be obtained experimentally. This factor found to work well is:

$$D_{\min}^* = D_{\min} (1 + \mu) \quad (7.11)$$

where

D_{\min}^* : modified minor diameter.

μ : a uniformly distributed random number within [0,0.3].

7.5.2 Sieve Series and Sieving Phase

The same sample population that had been applied to test the volumetric model was used to determine the calibration factors, ζ_{sv} . As stated previously, it consists of eight batches, whose basic statistics are tabulated in Table 6.1. The histograms of some measurements for each batch and for the total sample are included in Appendix II.

The sieve set consists of five sizes: 4.75 *mm*, 9.50 *mm*, 12.50 *mm*, 19.00 *mm*, and 25.00 *mm*. They are stacked with the largest mesh size at the top, with successively smaller mesh sizes below, as shown in Fig. 7.9. For the sake of notational convenience, d_{sv} denotes a sieve of any size. Note that the particles in investigation are poured in the top 25.00 *mm* sieve, falling through onto the next sieve below if not retained. Sieves are vibrated and rotated using an automatic sieve shaker.

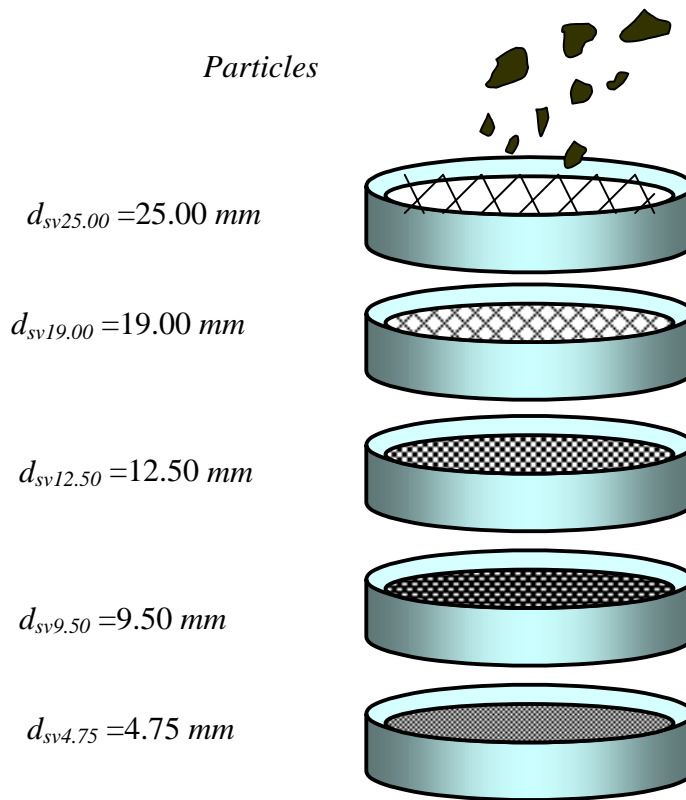

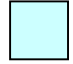



Figure 7.9 Physical Sieve Cascade


For a given sieve of size d_{sv} , only those particles whose minor diameter D_{min} , are within the range $d_{sv} < D_{min} < \sqrt{2} d_{sv}$, are candidates for sieving behavior consideration. The particles outside this range will be either retained in the upper sieve or pass through onto the lower sieve.

Fig. 7.10 outlines the overall sieving analysis for the whole prospective sample population.

 : A symbolic curve that means the particle may or may not be retained on the sieve.

 : The state in which all particles within the corresponding size range are partially retained, i.e., some pass, some remain in the current sieve.

 : The state in which all particles within the corresponding size range are absolutely retained.

 : The state in which all particles within the corresponding size range are partially retained either in the sieve of $d_{sv12.50}$, or in the sieve of $d_{sv9.50}$.

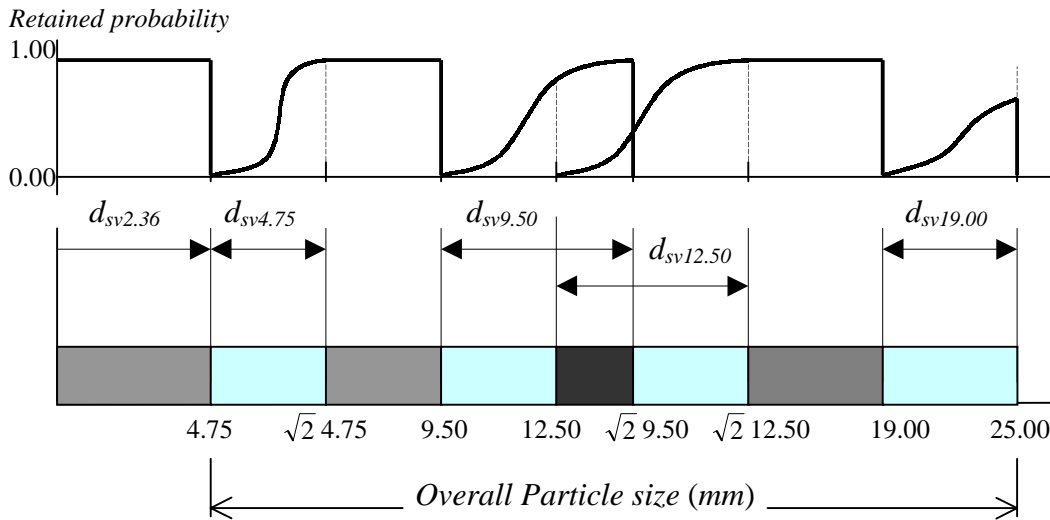


Figure 7.10 Overview of Sieving Phase Analysis

After all particles in the image scene have been processed, three available parameters can be used to conduct the vision sieving process: shape, minor diameter, and estimated mass, denoted as S_{shp} , D_{min} , and \hat{M} , respectively. For N particles in the image

scene having been processed, a data array can thus be formed ready for vision sieving processing:

$$\begin{bmatrix} S_{shp,1} & D_{min,1} & \hat{M}_1 \\ S_{shp,2} & D_{min,2} & \hat{M}_1 \\ \vdots & \vdots & \vdots \\ S_{shp,N-1} & D_{min,N-1} & \hat{M}_{N-1} \\ S_{shp,N} & D_{min,N} & \hat{M}_N \end{bmatrix} \quad (7.12)$$

The shape parameter gives information about the triangle shaped particles, whose minor diameter must be modified to correctly relate them to their sieving behavior.

In the algorithm, the sieving starts off with scanning the first column in matrix (7.12), finding triangles and modifying their diameters. Then the second column is scanned to group particles by size into bins for the percent passing statistics. The elements in the third column are assigned to the corresponding “volume bins” (sieves) suitable to their minor diameters. At the end of the “binning ” algorithm, the percent passing is computed as the Superpave specifies according to the formula:

$$\frac{\sum_{k=1}^m \hat{M}_k}{\sum_{w=1}^N \hat{M}_w} \times 100 \quad (7.13)$$

where

m : the total number of particles retained in the sieve in question.

N : the total number of particles in the population.

\hat{M}_k : mass of k^{th} particle in the sieve in question.

\hat{M}_w : mass of w^{th} particle in the population.

The pseudocode of the overall sieving procedure is given in Table 7.1. Note that the actual working code can be written in various ways, and the coding presented in the following pseudo code is not necessarily the optimal one. The major purpose here is to clearly present the logic thread imbedded in the optical sieving phase.

Table 7.1 Pseudocode of Sieving Procedure

```

/* After all particles have been processed, and the matrix of (7.12) is formed */

/* Scan 1st column for triangular shapes. */
for (each shape element in 1st column)
    if (it is a triangle)
        - modify its minor diameter in the 2nd column.
    end
end

/* Scan 2nd column for excluding particle sizes that are definitely retained in the sieve. */
for (each minor diameter element in 2nd column)
    if ( $D_{min} \leq 4.75$  or  $4.75\sqrt{2} \leq D_{min} \leq 9.50$  or  $12.50\sqrt{2} \leq D_{min} \leq 19.00$ )
        - place its mass into the corresponding sieve that retains it.
    end
end

/* Scan 2nd column again for particle sizes that are partially retained in the sieve. */
for (each minor diameter element in 2nd column)

    if ( $D_{min} \geq 19.00$  or  $9.50\sqrt{2} \leq D_{min} \leq 12.50\sqrt{2}$  or  $12.50 \leq D_{min} \leq 9.50\sqrt{2}$  or ...
         $9.50 \leq D_{min} \leq 12.50$  or  $4.75 \leq D_{min} \leq 4.75\sqrt{2}$ , referring to Fig. 7.10 )
        - compute for its critical flatness  $Y_{crit}$  using Eqn. (7.6)
        - calculate the probability  $P(Y_{flat}) \leq Y_{crit}$  using Eqn. (7.7)
        - generate a uniformly distributed random number  $\eta$ .

        if ( $\eta \leq \zeta_{sv} P(Y_{crit})$ , referring to conditions in (7.10))
            - pass the current sieve.
            if ( $12.50 \leq D_{min} \leq 9.50\sqrt{2}$ )
                - place it into sieve 9.50 mm for testing again.
            end /* end of "if" condition */
        elseif ( $\eta > \zeta_{sv} P(Y_{crit})$ , also referring to conditions in (7.10))
            - retained in the current sieve. Place its mass in this sieve.
        end /* end of "if" condition */

    end /* end of "if" condition */

end /* end of "for" loop */

/* Compute for the percent passing using Eqn (7.13) */

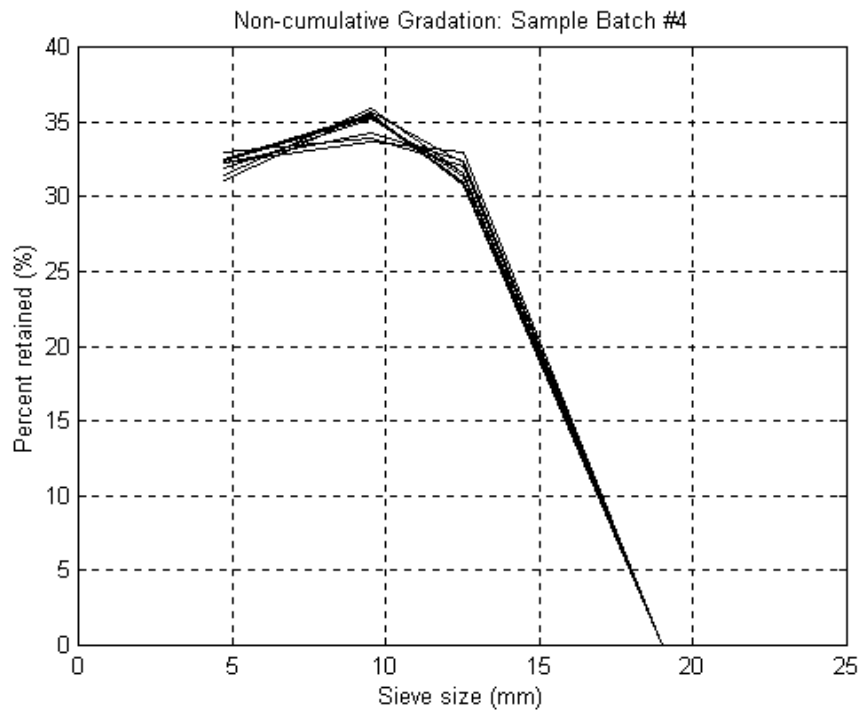
```

7.6 Benchmark

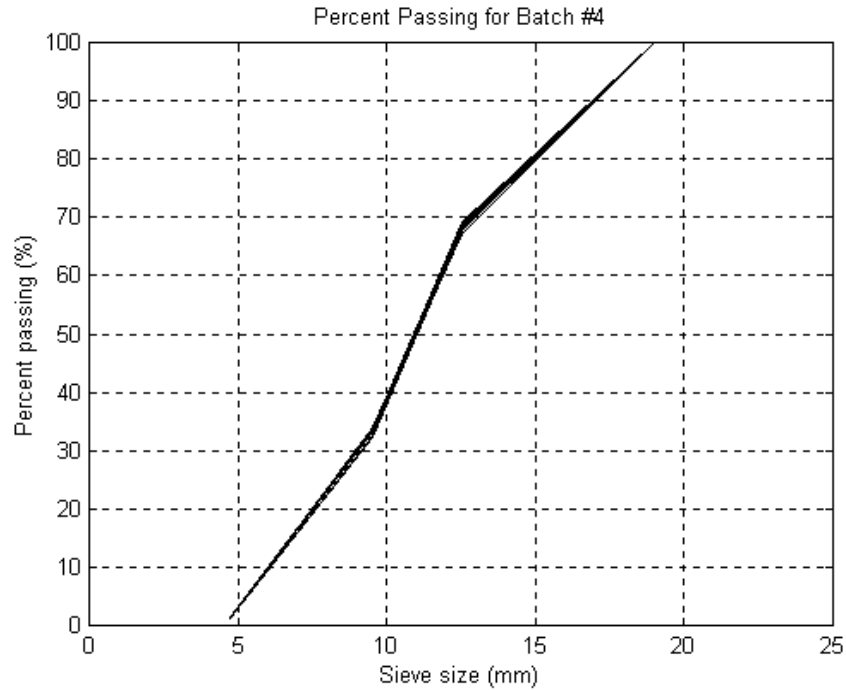
The particle size distribution (gradation) obtained from the vision sieving is calibrated against the results obtained from mechanically sieving the same sample. The

result works as the “benchmark” for the sieving parameter calibration. The same eight batches of sample particles were used to obtain the benchmark.

The eight batches of sample particles are mechanically sieved. Each batch was sieved ten times in order to achieve better accuracy. As a result, for each batch, ten percent passing curves and ten percent retained curves were obtained. The desired results, the percent retained and percent passing, can be acquired. By percent retained, it means the percent of the particles in terms of volume (or mass) retained on each of the five sieves. As an example, Fig. 7.11 (a) and (b) shows the result for batch #4 of percent retained and percent passing from mechanical sieving, respectively.



(a) percent retained



(b) percent passing

Figure 7.11 Percent Retained and Percent Passing for Sample Batch #4

As expected, each resultant curve does not coincide with each other. In other words, ten times of mechanical sieving come up with ten different results. Two major reasons may explain these differences. First, borderline particles may only pass for a very particular orientation, which may or may not be achieved during the random tumbling of the sieving process. Secondly, attrition occurs during the sieving process. When all the particles are toppling in the enclosure of the vibrating and rotating sieves, particles are hitting and breaking down each other, inevitably reducing the size and volume of each particle. As a consequence, the mass in each sieve decreases as sieving goes on. This affects the value of percent retained, and thereby, affects the percent passing. Fig. 7.12 shows for sample batch #7 the data scattering for the 9.50 mm, 12.50 mm, and 19.00 mm sieve results.

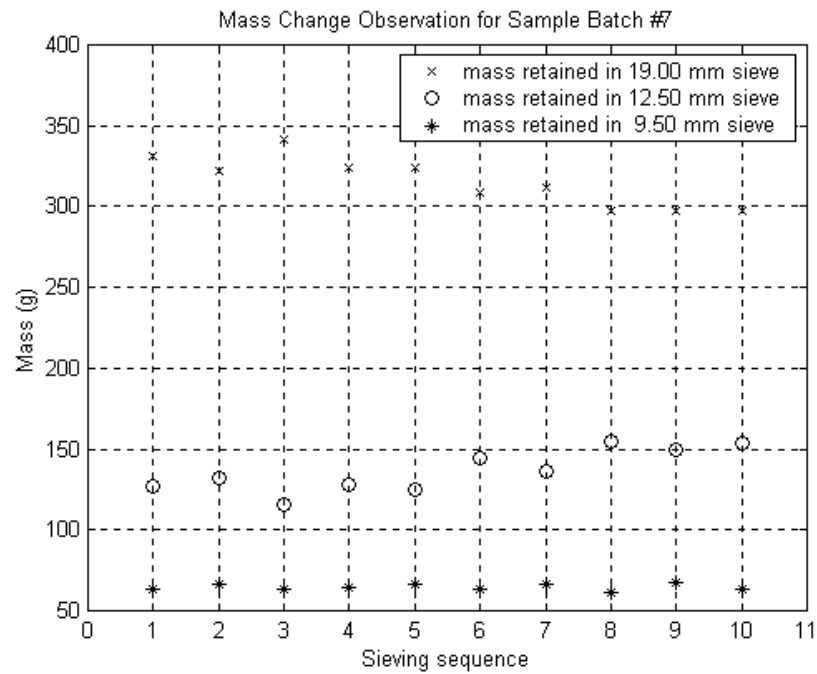
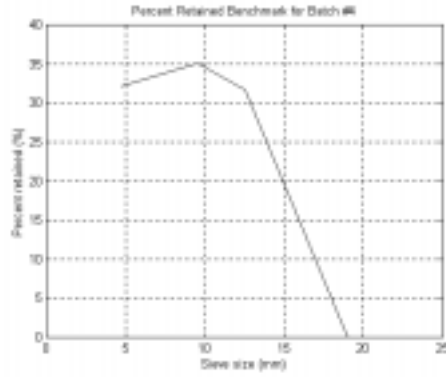
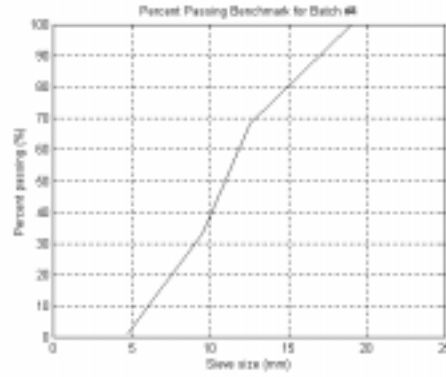


Figure 7.12 Mass Change in Sieving Process

To obtain the benchmark, the data points at each sieve size was averaged. Fig. 7.13 (a) (b) shows the benchmark of percent retained and percent passing, respectively, for sample batch #4.



(a) percent retained



(b) percent passing

Figure 7.13 Benchmark for Sample Batch #4

By the same method, the benchmark of all other batches was obtained, and given in Appendix III.

A sample population of larger size was formed by combining all the particles from the eight batches. The corresponding percent retained and percent passing benchmark are shown in Fig. 7.14, and the values are listed in Table 7.2.

7.7 Sieving Calibration Factor

Using a large sample population formed by combining all eight batches, the sieving calibration factor, ζ_{sv} , as introduced in inequality (7.10), was calibrated to be

$$\zeta_{sv} = \begin{bmatrix} \zeta_{19.00} \\ \zeta_{1250} \\ \zeta_{950} \\ \zeta_{4.75} \end{bmatrix} = \begin{bmatrix} 2.00 \\ 7.00 \\ 3.00 \\ 1.00 \end{bmatrix} \quad (7.14)$$

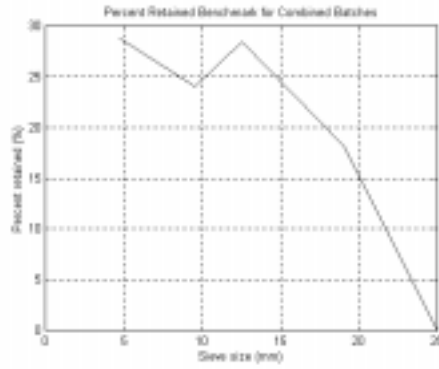
The calibration factors can be interpreted as follows:

The cross section of the particle is not rectangular. In most cases, the height at two ends of the minor diameter is shorter than the critical height H_{crit} , as illustrated

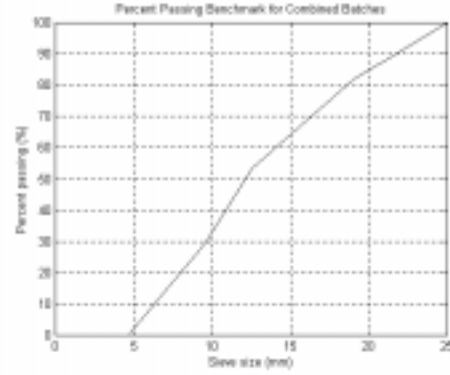
previously in Fig. 7.4. This apparently increases the probability for the particles to pass the sieve. $\zeta_{sv} \geq 1$ accounts for this rounding effect.

For each sieve of different size, there is a different calibration factor value. All these factors have been determined by back calculation from the large sample population with known size distribution. With the addition of these calibration factors, the sieving strategy's conditions expressed in inequality (7.10) becomes semi-empirical, because they are empirically derived values. The significance of ζ_{sv} is that it accounts for numerous effects such as particle's cross section shape distribution. In summary, the physical significance is to account for combination of the following aspects:

- 1) The effect of the particle's cross section shape distribution. Although there is no theoretical *a priori* knowledge about cross section shape distribution inherent in the used method, it does affect the behavior of particles in the sieve to pass or be retained.
- 2) The effects of separation of overlapping and touching particles. Using the developed algorithm, the separated particles' shape and mass are not the same as they are manually isolated. This affects the particle's sieving behavior. Again, no *a priori* knowledge is available to determine even statistically how the sieving behavior will be influenced.
- 3) The effects caused by vision system errors such as hardware calibration, software imperfection.
- 4) The effects of sample population size.



(a) percent retained



(b) percent passing

Figure 7.14 Benchmark for Combined Sample Batches

Table 7.2 Benchmark Values for Combined Sample Batches

Type	Sieve Size (<i>mm</i>)				
	4.75	9.50	12.50	19.00	25.00
Percent Retained (%)	28.806	23.996	28.390	18.250	0.000
Percent Passing (%)	0.557	29.383	53.385	81.766	100

7.8 Vision Sieving Result

With the calibrated ζ_{sv} 's, sieving correlation testing conducted. The samples are the same as those used for volumetric model testing, i.e., eight batches with a total of 1862 particles. Recall that the benchmark has been available, as shown in Fig. 7.14. The basic algorithm was written in Table 7.1

Again, a random combination of the images was taken, each of combination's constituent image was randomly selected from one different sample batch. This indicates that the total number of particles will increase up to $N = N_1 + N_2 + \dots + N_8 = 1862$, which is a

summation of particle number of all eight batches. Fig. 7.15 illustrates how a random combination of photo d, a, b, e, b, d, c, a selected from sample batch #1, #2, ..., #8 respectively, is formed.

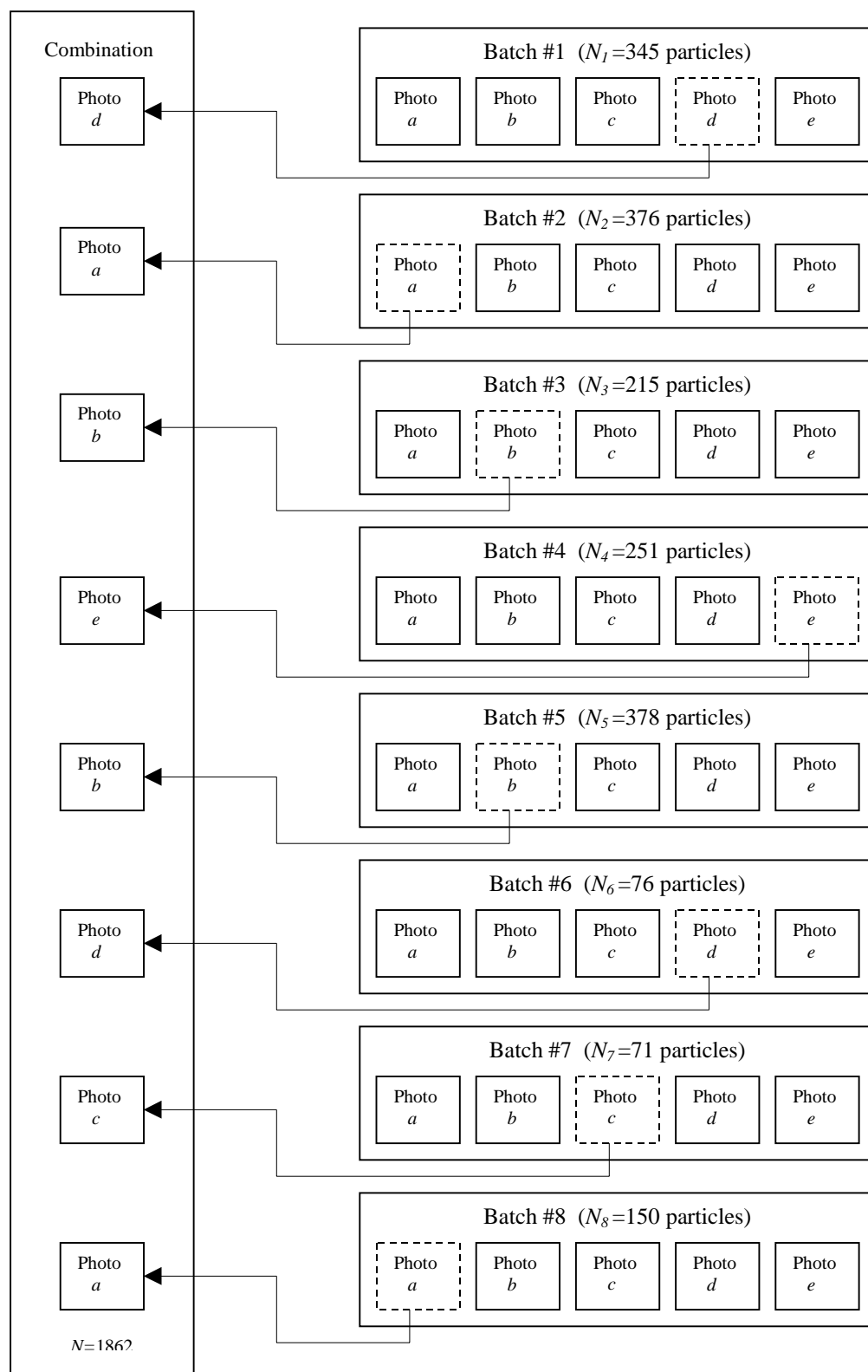


Figure 7.15 A Random Combination of Sample Batches (*dabebdca*)

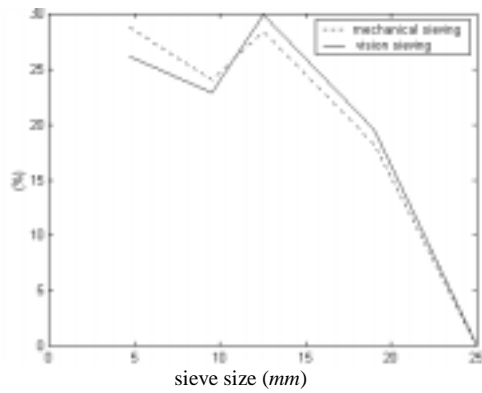
In effect, each random combination represents one “grand” image covering all 1862 particles. Each constituent image results from a new “shuffling” of the same sample batch. Therefore, each random combination of images may be regarded as result of “grand shuffling” of 1862 particles.

Testing on five grand images was conducted. This means that 1862 particles were shuffled five times to produce these five grand images. On each grand image, all particles were “optically” sieve ten times, final vision sieving result is taken by averaging these ten results, and then compare it to the benchmark.

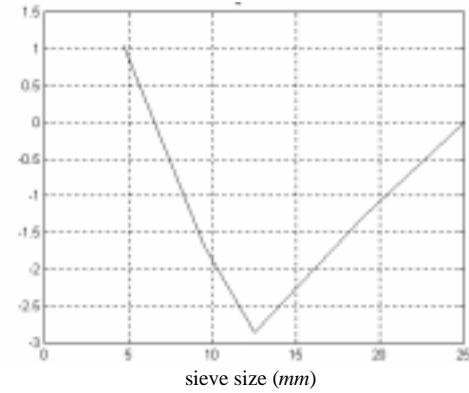
Figures from Fig. 7.16 to Fig. 7.20 demonstrate the results of these five testings. From the results, it shows that the percent passing residuals are within $\pm 3\%$. The residual between the percent passing benchmark and vision sieving percent passing is listed in Table 7.3. The error may be contributed to by the following reasons:

- 1) Simple measurement of the particle minor diameter is not an entirely true representation of what happens in physical sieving. Particles that are somewhat flat can turn diagonally in the sieve and pass a smaller mesh size than one would suspect from simple size measurements.
- 2) Error in the calibration factor *mm/pixel* can contribute to vision sieving error.
- 3) Accurate measurement of percent passing requires accurate projection of the volume from the optically measured parameters. This in practice is impossible to achieve with extreme accuracy, especially for individual particles.
- 4) Error existing in minor diameter estimation for triangular shapes can contribute to sieving correlation error.

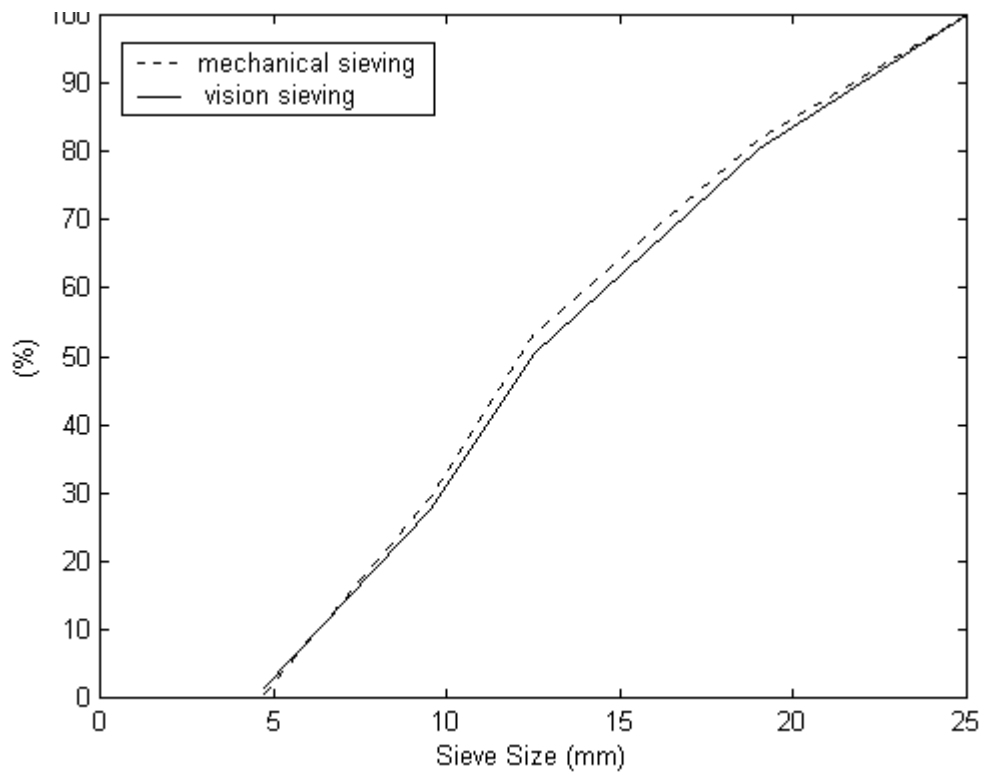
- 5) Overlapping and touching particles' profile shape and volume estimate change during separation.
- 6) If the size sample population is not sufficiently large, it will create error in vision sieving process because a uniformly distributed random number is involved in determining "pass or retain" for a particle in the sieve.
- 7) The benchmark itself has certain discrepancies due to particle physical sieving behavior.



(a) percent retained



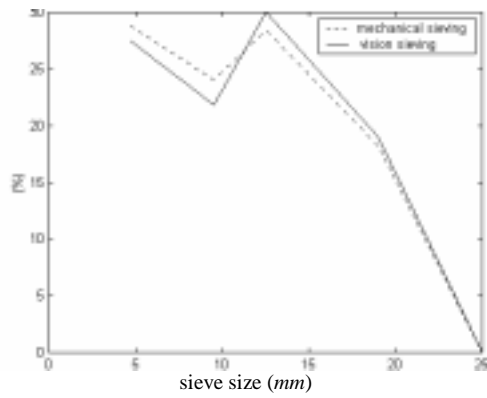
(b) percent passing residual



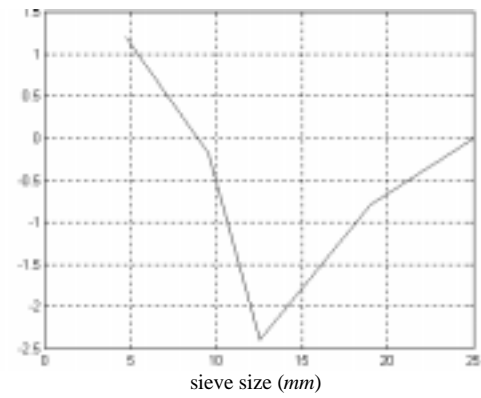
(c) cumulative percent passing

Figure 7.16 Sieving Correlation Testing #1

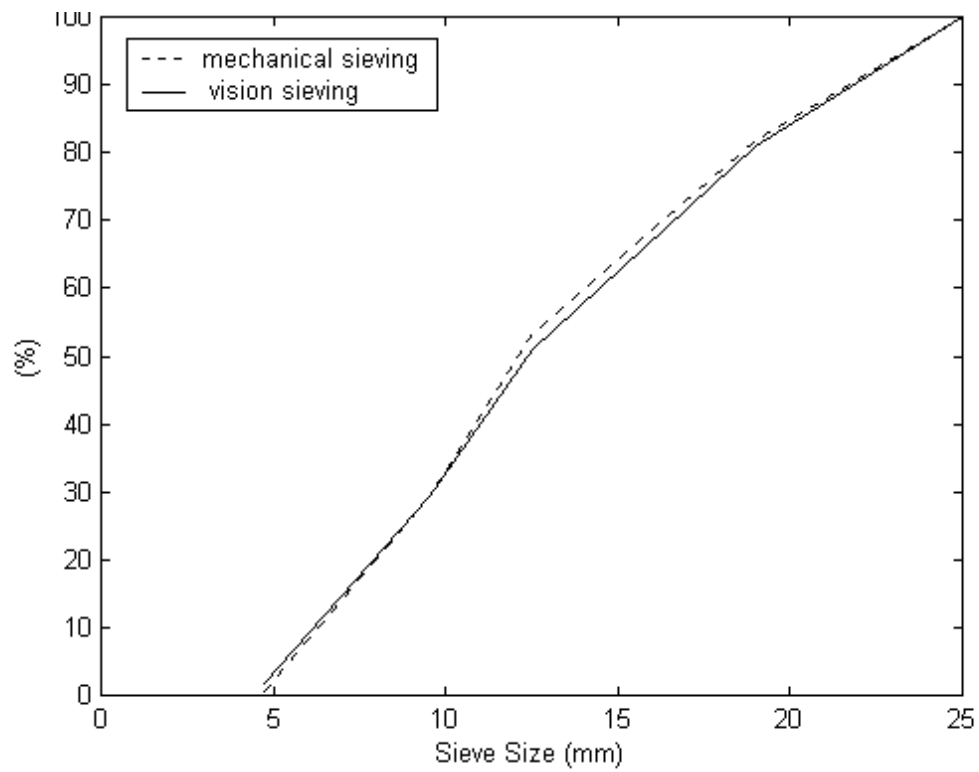
(Combination: image e,e,d,b,c,d,c,e from sample batch #1 to #8, respectively)



(a) percent retained



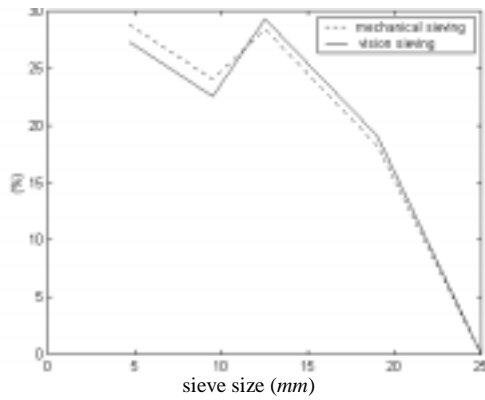
(b) percent passing residual



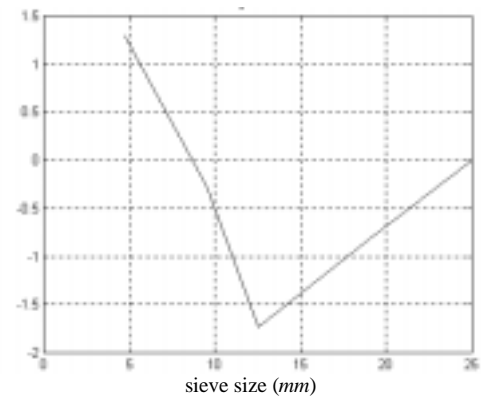
(c) cumulative percent passing

Figure 7.17 Sieving Correlation Testing #2

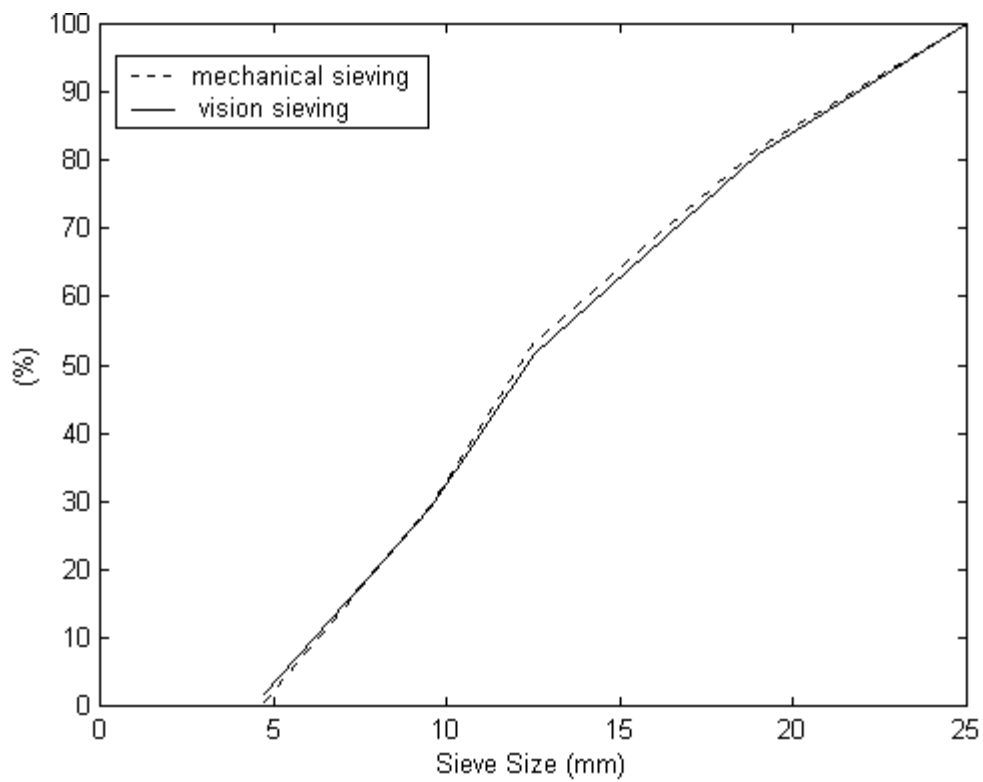
(Combination: image c,e,a,c,a,b,d,e from sample batch #1 to #8, respectively)



(a) percent retained



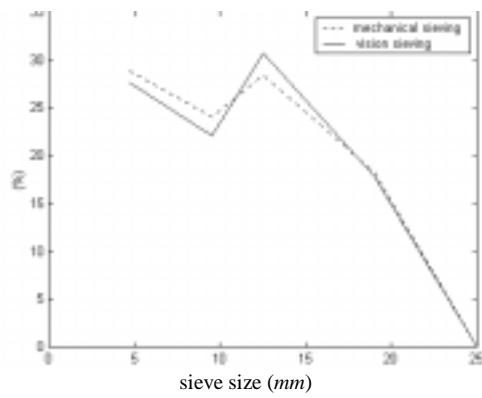
(b) percent passing residual



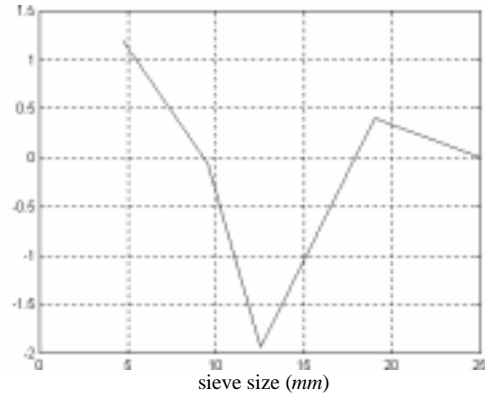
(c) cumulative percent passing

Figure 7.18 Sieving Correlation Testing #3

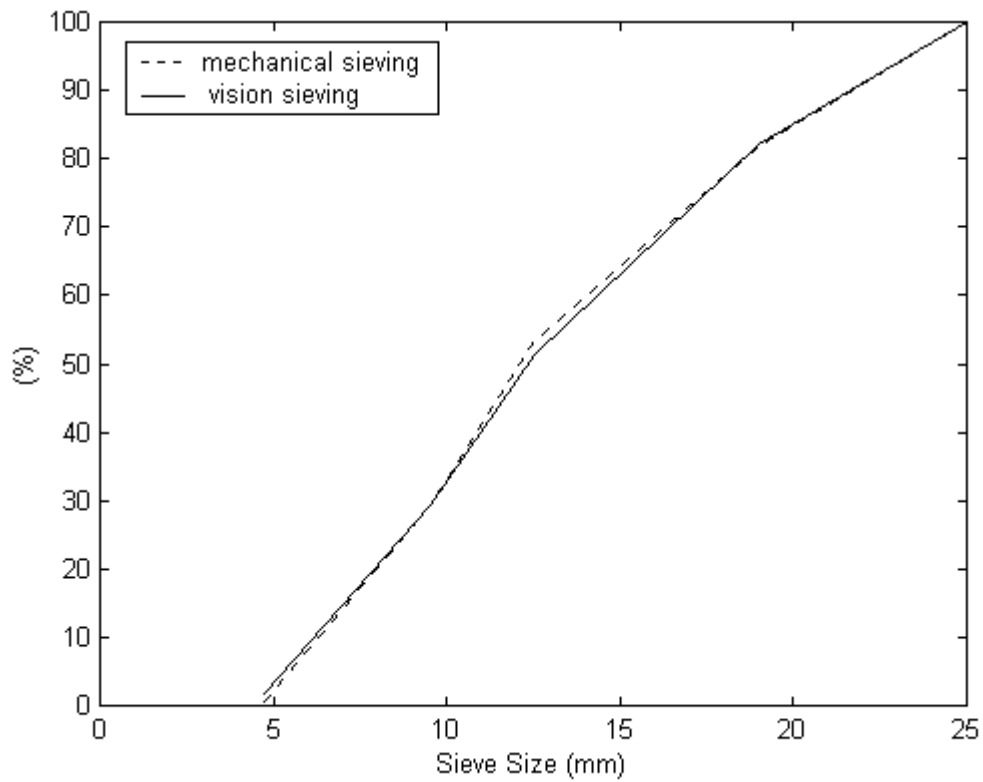
(Combination: image e,d,e,a,a,a,b,c from sample batch #1 to #8, respectively)



(a) percent retained



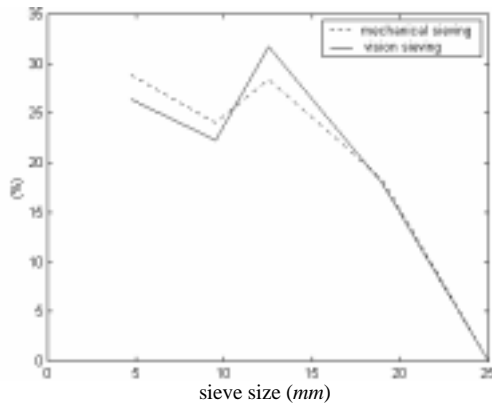
(b) percent passing residual



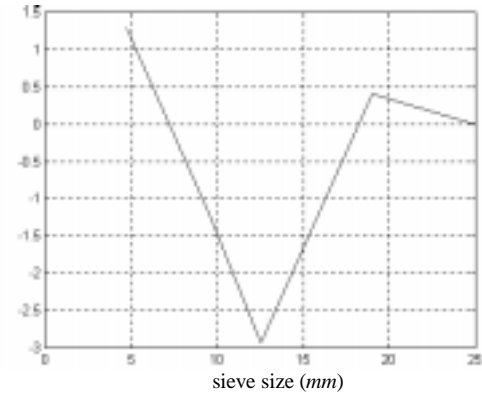
(c) cumulative percent passing

Figure 7.19 Sieving Correlation Testing #4

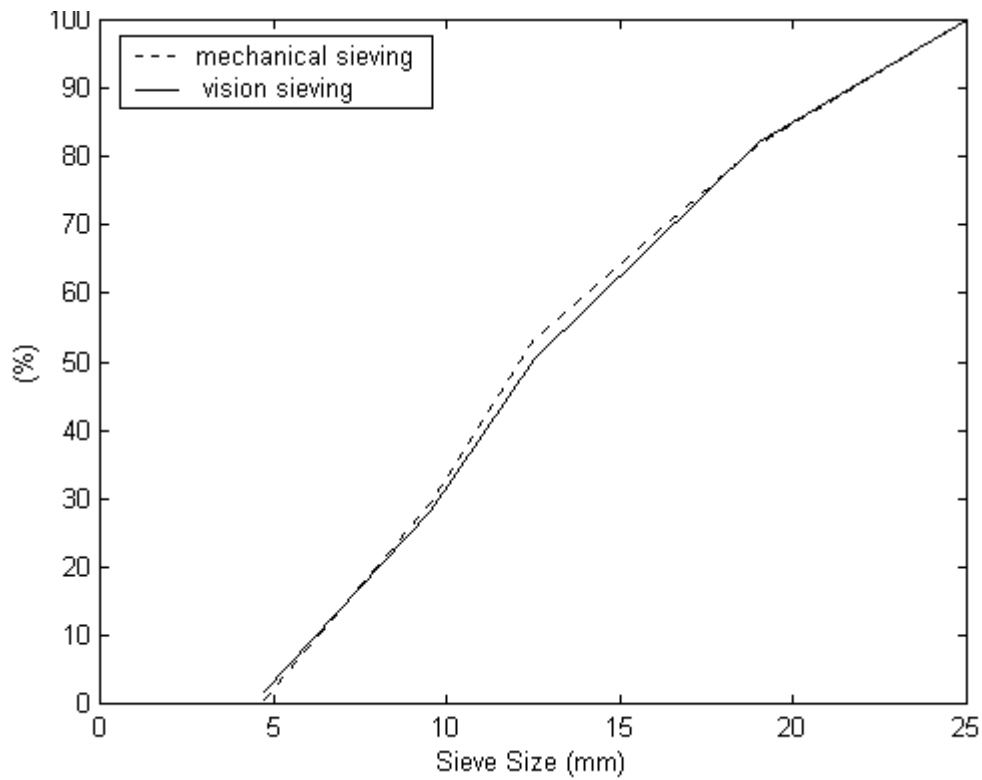
(Combination: image b,e,c,e,a,e,e,e from sample batch #1 to #8, respectively)



(a) percent retained



(b) percent passing residual



(c) cumulative percent passing

Figure 7.20 Sieving Correlation Testing #5

(Combination: image e,d,d,a,c,e,d,b from sample batch #1 to #8, respectively)

Table 7.3 Testing Residuals

Test number	Sieve Size (<i>mm</i>)				
	4.75	9.50	12.50	19.00	25.00
	Percent-Passing Residual (%)				
#1	1.0406	-1.6774	-2.8493	-1.2805	0.0000
#2	1.1905	-0.1776	-2.3980	-0.7918	0.0000
#3	1.2950	-0.2743	-1.7304	-0.8218	0.0000
#4	1.1915	-0.0563	-1.9429	0.4042	0.0000
#5	1.2828	-1.1989	-2.9305	0.3992	0.0000
Mean Error	1.2001	-0.6769	-2.3702	0.4181	0.0000

8. SYSTEM PERFORMANCE

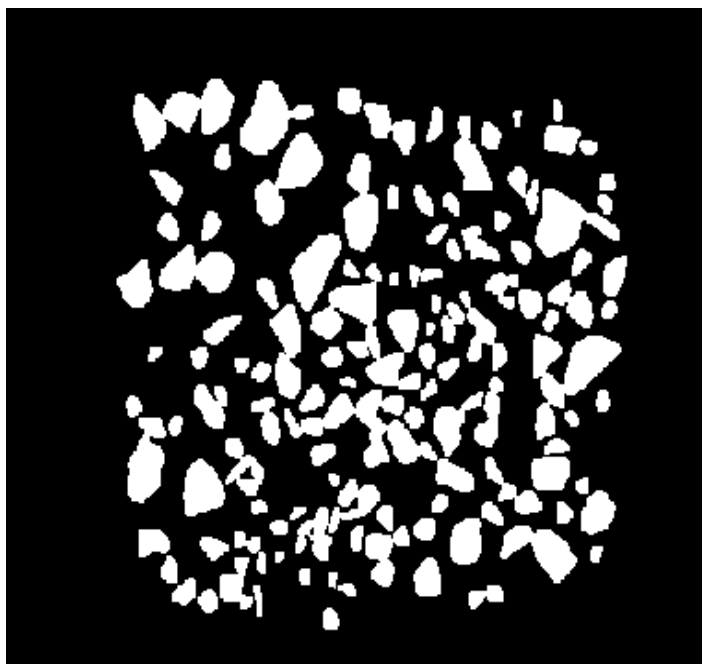
8.1 Introduction

The testing results that have been obtained thus far were from the sample population in which all the particles were separated manually. In practice, it is implausible to manually arrange a large number of particles prior to being imaged.

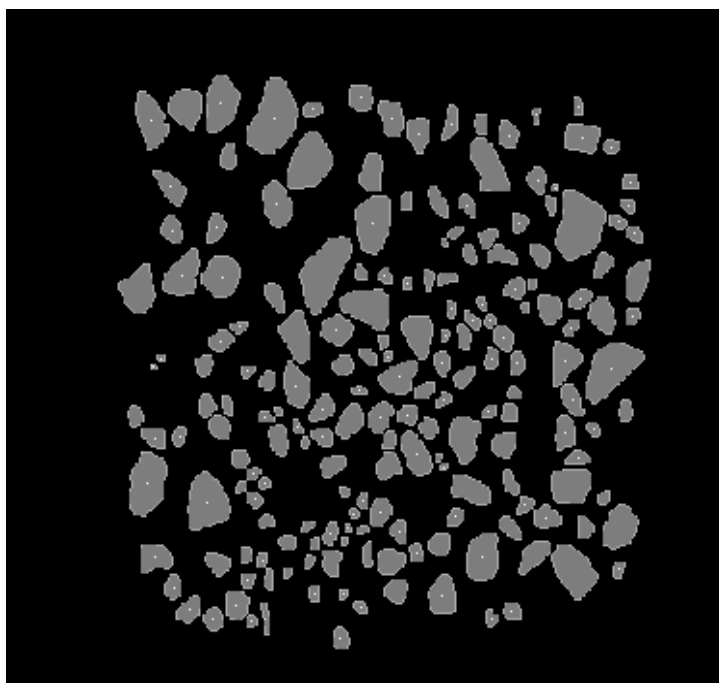
In this chapter, a sample population was arranged in such a way that particle touching and overlapping occurrences were allowed. The touching and overlapping particles are separated using the separation algorithm described in chapter 5, then go through the same process of image analysis as did the samples previously. The benchmark of percent passing for the sample tested is obtained from the WVU civil engineering laboratory. By comparison of the optical sieving result and the benchmark, the performance of the system is evaluated.

8.2 Sample Preparation and Discussion

A sample of population of $N=1972$ particles was prepared for testing the performance of the developed system. These particles were broken down into ten sample groups due to backlight panel dimension limitation. In each sample group, touching and overlapping were allowed among particles. For sample group #2, Fig. 8.1 (a) shows the binary images with some occurrences of touching and overlapping of limited extent, while (b) shows the corresponding image in which separation was completed. The similar figures for all ten groups are given in Appendix IV.



(a) group #2: particles with touching and overlapping



(b) group #2: particles after separation

Figure 8.1 Particles of Sample Group #2

Some effects caused by separation can be observed after applying the algorithm to such a large number of particles. For a few particles, “false cutting” took place, mainly for particles with a concave shape. This increases the total number of particles retained in smaller sieves. “Miscutting” was noted among a very small number of particles. By miscutting, it means that the connected particles are separated, but not at the place they should be. The reason for miscutting is complex, and is definitely related to the contour shape of the connected particles. In most cases, the separating process appears satisfactory. The impact on the sieving results caused by separation is assumed to be insignificant.

To gain some statistical perception of the sample population tested, the histogram of optically measured minor diameter, estimated flatness, and estimated volume are presented in Fig. 8.2, Fig. 8.3, and Fig. 8.4, respectively.

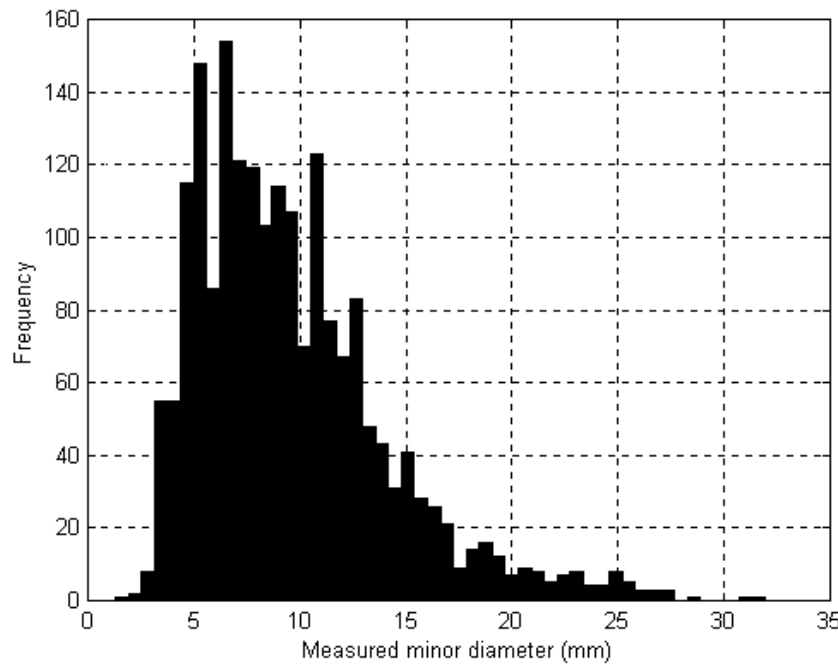


Figure 8.2 Histogram of Measured Minor Diameter

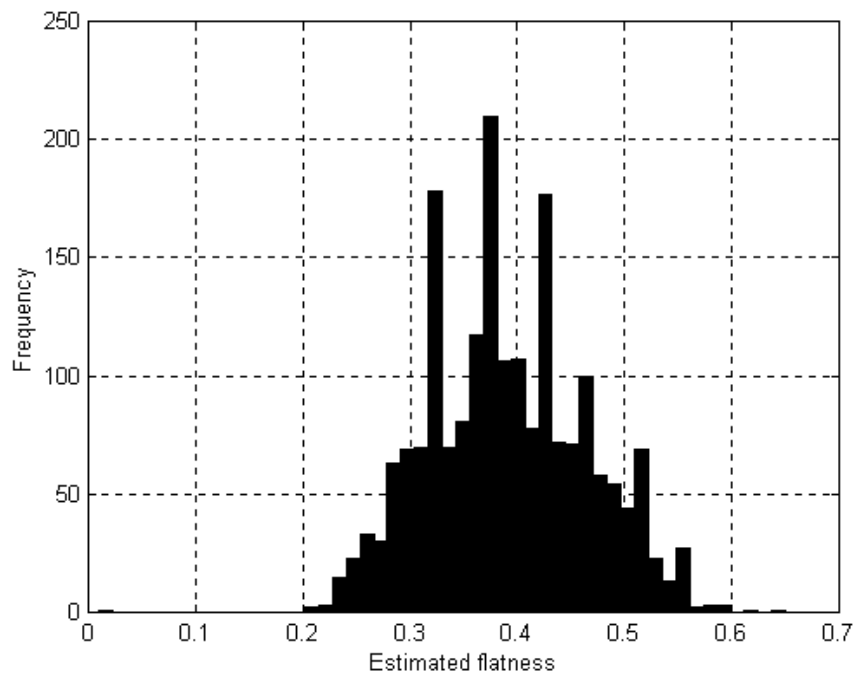


Figure 8.3 Histogram of Estimated Flatness

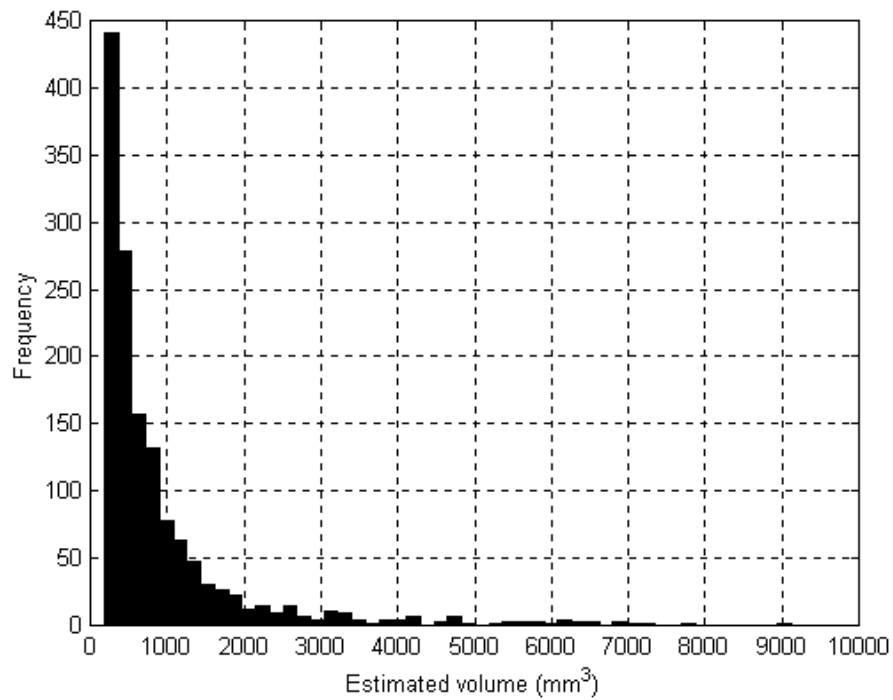
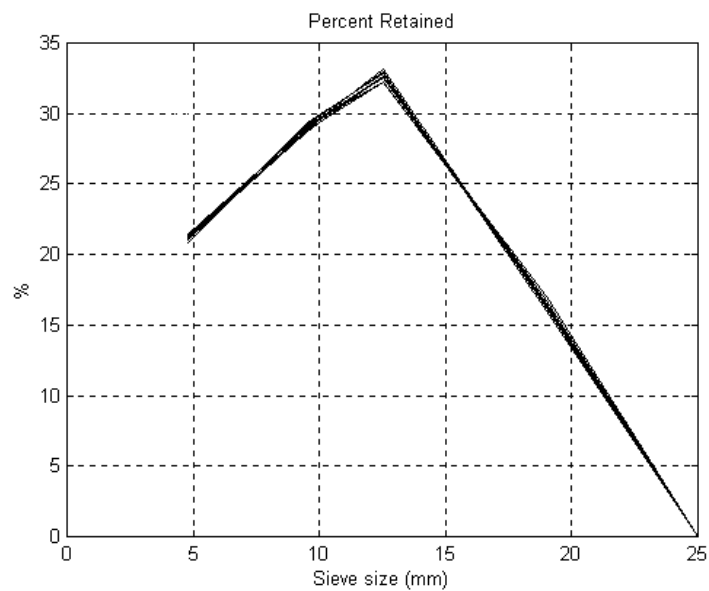


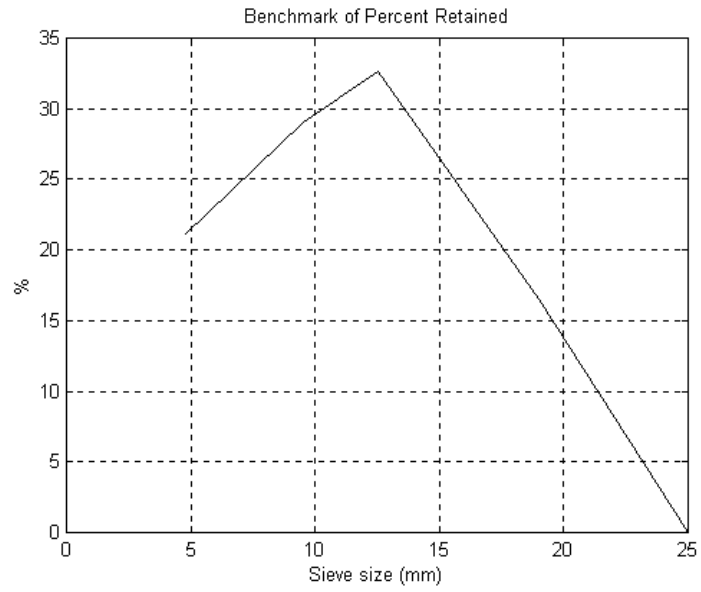
Figure 8.4 Histogram of Estimated Volume

8.3 Sample Benchmark

The sample of 1972 particles was mechanically sieved ten times in the laboratory. Each time the sieving result is expectedly different. The causes of these differences were described in section 7.6. Fig. 8.5 (a) shows the percent retained curves from the ten sievings, and (b) is the benchmark that is averaged from these ten values at each sieve size. Correspondingly, Fig. 8.6 (a) shows the ten percent passing curves, and (b) works as the percent passing benchmark for the sample population that will be sieved optically.

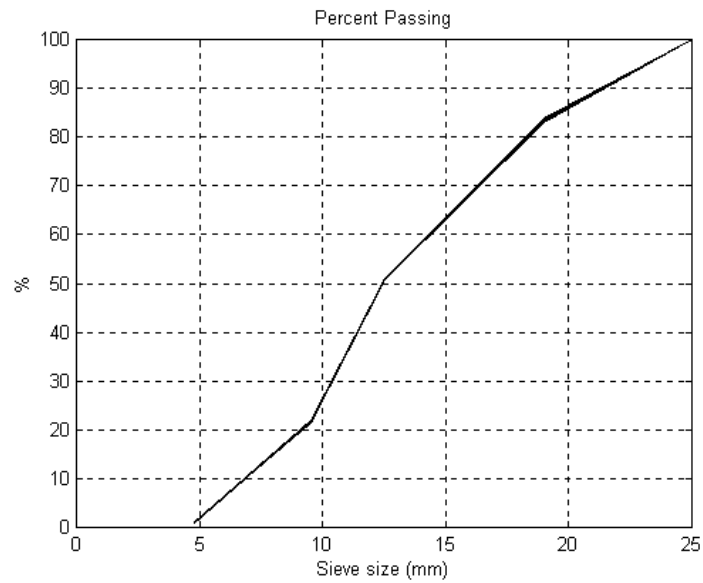


(a) percent retained curves for sieving 10 times

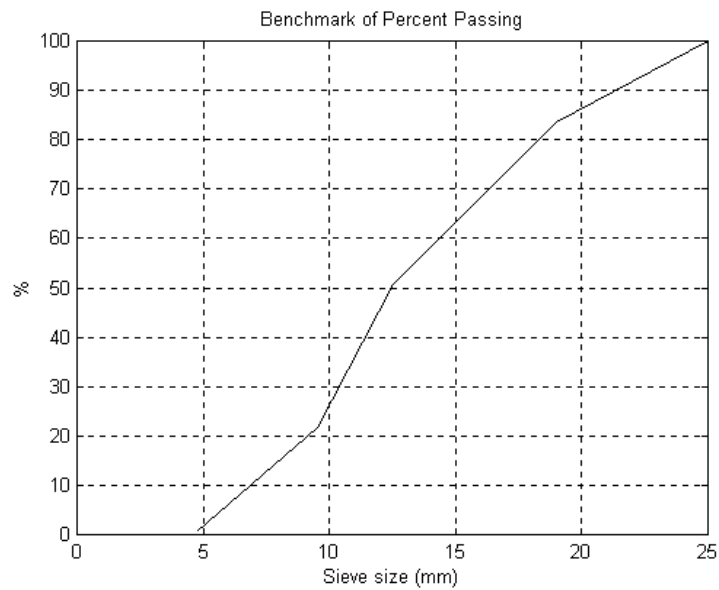


(b) averaged curve as the benchmark

Figure 8.5 Percent Retained Benchmark



(a) percent passing curves for sieving 10 times



(b) averaged curve as the benchmark

Figure 8.6 Percent Passing Benchmark

The statistics of the mechanical sieving is tabulated in the table below.

Table 8.1 Statistics of the Benchmark (Sieving of 10 times)

Percent Retained (%)			Percent Passing (%)		
Sieve size (mm)	Mean	Variance	Sieve size (mm)	Mean	Variance
25.00	0.00	0.00	25.00	100.00	0.00
19.00	16.51	0.10	19.00	83.49	0.10
12.50	32.65	0.08	12.50	50.84	0.03
9.50	29.06	0.03	9.50	21.78	0.02
4.75	21.06	0.03	4.75	0.72	0.00

8.4 Results Comparison

To establish confidence in the optical sieving system, the technique must yield results readily comparable to mechanical sieving methods.

For these separated 1972 particles, the same sieving procedure was used as had been for those samples described in section 7.8. The same sieving calibration factors were used. The sample was “optically” sieved 10 times, and the mean of the results was taken as the test value.

The results are listed in Table 8.2 and Table 8.3. Fig. 8.7 and Fig. 8.8 show the graphical comparison.

Table 8.2 Percent Retained Result Comparison

	Sieve Size (mm)							
	4.75		9.50		12.50		19.00	
Test -ing #	Benchmark Value (%)							
	21.06		29.06		32.65		16.51	
	Comparison and Residual							
	Testing result	Residual	Testing result	Residual	Testing result	Residual	Testing result	Residual
1	23.33	2.27	27.85	-1.21	33.91	1.26	13.28	-3.23
2	22.16	1.10	29.47	0.41	31.10	-1.55	15.45	-1.05
3	22.34	1.28	28.95	-0.11	32.09	-0.56	14.91	-1.60
4	23.45	2.39	28.77	-0.29	32.62	-0.03	13.63	-2.87
5	22.95	1.89	28.08	-0.98	34.12	1.47	13.27	-3.24
6	22.55	1.49	29.27	0.21	32.67	0.02	13.85	-2.65
7	22.19	1.13	29.59	0.53	31.95	-0.70	14.59	-1.91
8	23.06	2.00	28.59	-0.47	31.26	-1.39	15.47	-1.04
9	22.59	1.53	29.21	0.15	32.12	-0.53	14.40	-2.11
10	22.49	1.43	28.64	-0.42	33.16	0.51	13.97	-2.54
	Average Values							
	22.71	1.65	28.84	-0.22	32.50	-0.15	14.28	-2.22

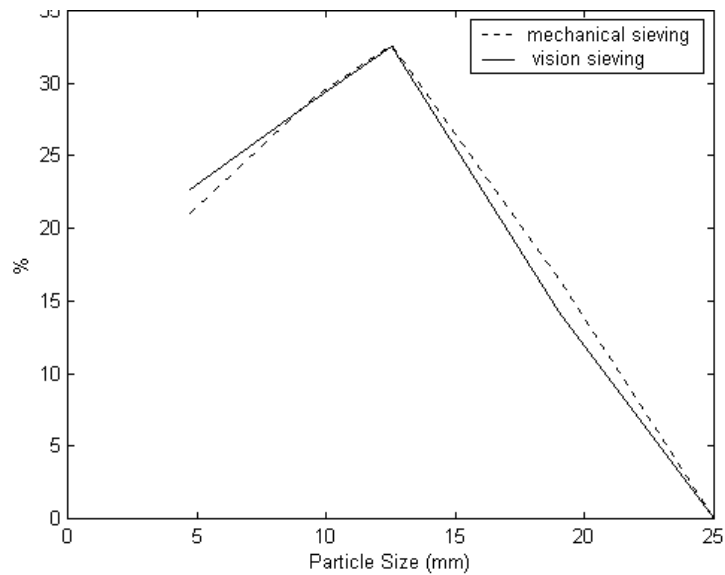


Figure 8.7 Percent Retained Correlation

Table 8.3 Percent Passing Result Comparison

	Sieve Size (mm)							
	4.75		9.50		12.50		19.00	
Test -ing #	Benchmark Value							
	0.72		21.78		50.84		83.49	
	Comparison and Residual (%)							
	Testing result	Residual	Testing result	Residual	Testing result	Residual	Testing result	Residual
1	1.63	0.90	24.96	3.17	52.81	1.96	86.72	3.23
2	1.82	1.10	23.97	2.19	53.44	2.60	84.55	1.05
3	1.71	0.99	24.05	2.26	53.00	2.15	85.09	1.60
4	1.53	0.81	24.98	3.19	53.75	2.90	86.37	2.87
5	1.58	0.86	24.53	2.74	52.61	1.77	86.73	3.24
6	1.65	0.93	24.20	2.42	53.48	2.63	86.15	2.65
7	1.68	0.95	23.87	2.08	53.45	2.61	85.41	1.91
8	1.62	0.89	24.68	2.90	53.28	2.43	84.53	1.04
9	1.68	0.95	24.27	2.48	53.48	2.64	85.60	2.11
10	1.74	1.02	24.23	2.45	52.87	2.03	86.03	2.54
	Average Values							
	1.66	0.94	24.37	2.59	53.22	2.37	85.72	2.22

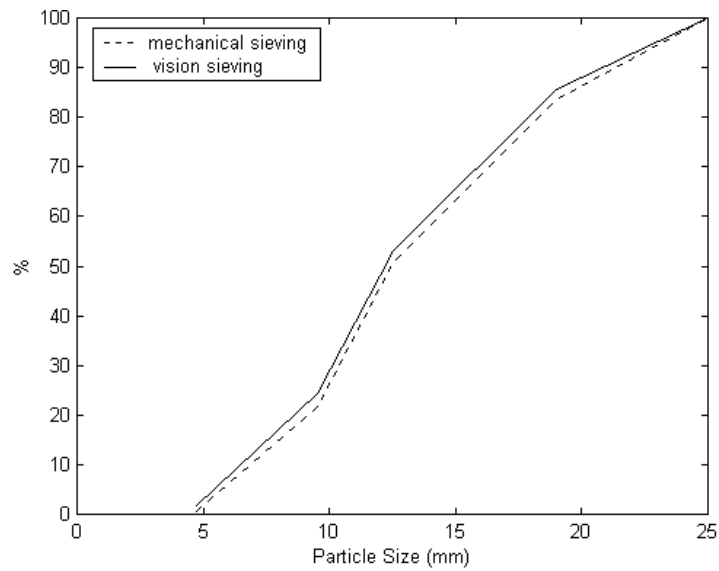


Figure 8.8 Percent Passing Correlation

The vision sieving results of percent passing are all over-estimated after the ten algorithm executions, but the residuals all are under 3 points, which is reasonably acceptable. Several literature reports concerning video grading point out that sample preparation and segmentation methods are a primary source of error. There can be numerous causes that contribute to the testing error, as stated in section 7.8. To analyze aggregates samples comprised of a mix of widely different particles, sorting the sample into groups of similar size is suggested [33, 39].

9. CONCLUSIONS AND FUTURE RESEARCH

9.1 Conclusions

In this dissertation, the feasibility was investigated of using a non-contact optical technique to provide information on crushed limestone aggregates' gradation. The research was conducted mainly on the following three areas and have contributed some insights to prospective application of optical sieving which is to replace relatively slower mechanical methods.

First, particles are often touching and overlapping in the imaged scene. One major contribution of this work has been the development of a simple and effective method to discriminate the touching and overlapping particles in the imaged scene.

Second, standards for classifying particles are generally based on size and mass. Mass needs to be known in order to perform gradation. A second major contribution is the development of a volume model that relates variables available from 2-D aggregate image to particle volume. Assuming constant density, mass is estimated from volume.

Third, as Superpave stipulates, percent-passing curve is used to measure proper mixture of particles of varying sizes. The conventional way of obtaining this curve is based on mechanical sieving. A contribution made in this work is that using statistical analysis, a correlation between mechanical and optical sieving has been constructed.

9.2 Future Research

There are three major areas that are related to this research and may need to be studied further.

First, is there a possibility to apply the same technique to fine particles? It is believed that the processes developed in this research project constitute a feasible approach to the problem of optical sieving of fine aggregates. Although the methods in this research were only demonstrated for the coarse aggregates, it is believed that similar techniques could be applied to fine aggregates by positioning the camera closer to the particles or by using a longer focal length lens to obtain greater magnification, or simply by using a higher resolution camera. It is unlikely that any single scanning technology can yield the desired accuracy for measuring particle sizes over a very broad range. For example, one may need two different grading station designs; one optimized for scanning fine aggregates and a second optimized for scanning coarse aggregates [33]. Since fine particles and dust tend to agglomerate in piles several layers thick, some additional methods may be necessary to evaluate the fines.

Second, specifications are given to coarse aggregate angularity in the Superpave guidebook. In this work, significant effort to this subject has not been devoted. However, it is reasonable to believe that using the similar methods developed in this work for particle shape characterization, automated means to measure coarse aggregate angularity could be feasible.

Consideration of the source of system error is a broad and important topic. There are many factors inherent in the measuring system that adversely affect its accuracy. Of interest would be studies of various types of aggregates and their characteristics, requirements for camera resolution, sampling methods and limitation, and refinements of the volume and sieving models. N. Maerz has investigated some aspects of system error in [25], but the topic remains a rich one for continuing the work.

The approach developed in this work was based on a relatively low cost vision system and sophisticated image analysis. The algorithms were tested on a limited number of samples, and have produced encouraging results. The approaches described in this dissertation are theoretically sound and practically plausible. The research shows that the automation of coarse aggregate inspection is a feasible idea.

BIBLIOGRAPHY

1. US Department of Transportation, Federal Highway Administration, *Background of Superpave Asphalt Mixture Design and Analysis*. Publication No. FHWA-SA-95-003, February, 1995.
2. Rafeal G. Gonzalez, and Richard E. Woods, *Digital Image Processing*. (Massachusetts: Addison-Wesley Publishing, 1992).
3. Mohammed Bennamoun, and Boualem Boashash. "A Structural-Description-Based Vision System for Automatic Object Recognition." *IEEE Transactions on system, man, and cybernetics-Part B: Cybernetics*, vol. 27, no. 6 (1997): 893-906.
4. R. M. Parkin, D. W. Calkin, and M. R. Jackson, "Roadstone Aggregate: An Intelligent Opto-Mechatronic Product Classifier for Sizing and Grading." *Mechatronics*, vol. 5, no. 5 (1995): 461-467.
5. Carlo Castellini, Franco Francini, and Giuseppe Longobardi, and Enrico Pampaloni, "On-Line Characterization of the Shape and Size of Particles." *Part. Part. Syst. Charact.* vol. 10, no. 1 (1993): 7-10.
6. P. L. Rosin, and G. A. W. West, "Curve Segmentation and Recognition by Superellipses." *IEE Proceedings-Vision, Image, Signal Processing*, vol. 143, no. 3 (1995): 280-288.
7. N. N. Clark, "Three Techniques for Implementing Digital Fractal Analysis of Particle Shape." *Powder Technology*, vol. 46, no. 1 (1986).
8. James Pickett, Nigel Clark, and Stephanie Shuker, "A Re-examination of Piper's Shape Analysis Technique." *Part. Part. Syst. Charact.* vol. 8 (1991): 110-115.

9. Nigel N. Clark, and Stephanie Reilly, "Template Matching for Particle Shape Description." *Particulate Science and Technology*, vol. 13, no. 2 (1995): 69-83.
10. S. Reilly, and N. N. Clark, "Computer Based General Shape Description with Polygonal Harmonics and a Roughness Index." *Proc. Instn. Mech. Engrs.* vol. 205 (1991): 103-111.
11. Clark N. N., and T. P. Meloy, "Delta Analysis of Particle Surface Fine Structure." *Journal of Powder & Bulk Solids Technology*, vol. 9, no. 1 (1985): 1-8.
12. Anthony J. Maeder, and Nigel N. Clark, "Harmonic Endurance: A New Shape Descriptor Derived from Polygonal Harmonics." *Powder Technology*, vol. 68 (1991): 137-143.
13. Thomas P. Meloy, and Nigel N. Clark, "Fourier Analysis: A Computer Based Technique for Particle Shape Characterization." Conference on Computers in the Coal Industry, Morgantown, WV, June 1986, Proceedings, pp. 309-319.
14. H. J. Noordmans, and A. W. M. Smeulders, "Detection and Characterization of Isolated and Overlapping Spots." *Computer Vision and Image Understanding*, vol. 70, no. 1 (1998): 23-35.
15. Edward R. Dougherty, *An Introduction to Morphological Image Processing*. vol. TT9 (Washington: SPIE –The International Society for Optical Engineering, 1992).
16. William W. Hines, and Douglas C. Montgomery, *Probability and Statistics in Engineering and Management Science*. 2d ed., (New York: John Wiley & Sons, Inc. 1980).
17. Douglas C. Montgomery, *Design and Analysis of Experiments*. (New York: John Wiley & Sons, Inc. 1976).

18. Raymond H. Myers, *Classical and Modern Regression with Applications*. 2d ed., (PWS-KENT Publishing Company, 1990).
19. Shibata Toshiharu, and Yamaguchi Kenji, "Shift X, Y-coordinate Direction of Line Figures and the Extraction of Particle Shape Information." *Powder Technology*, vol. 81, no. 2 (1994).
20. O.R. Mitchell, K. Fukunaga, TP. Wallace, "Three-dimensional Shape Analysis Using Local Descriptors." *IEEE Trans. Pattern Analy. and Mach. Intellig.*, vol. 3, no. 3 (1981).
21. Luc Vincent, "Applied Morphological and Nonlinear Image Analysis Techniques." Short Course Notes, Xerox Scansoft, Palo Alto, CA, 1998.
22. S. R. Krogh, "Crushing Characteristics." *Powder Technology*, vol. 27 (1980): 171-181.
23. R. P. King, "Linear Stochastic Model for Mineral Liberation." *Powder Technology*, vol. 81 (1994): 217-234.
24. Alexander V. Potapov, and Charles S. Campbell, "Computer Simulation of Impact-Induced Particle Breakage." *Powder Technology*, vol. 87 (1996): 207-216.
25. Norbert H. Maerz, and Wei Zhou, "Optical Digital Fragmentation Measuring Systems – Inherent Sources of Error." *FRAGBLAST, The International Journal for Blasting and Fragmentation*, vol. 2, no.4 (1998): 415-431.
26. N. H. Maerz, "Aggregate Sizing and Shape Determination Using Digital Image Processing." International Center for Aggregate Research (ICAR) 6th Annual Symposium Proceedings, St. Louis, Missouri, April 19-20, 1998, pp. 195-203.

27. N. H. Maerz, "Reconstructing 3-D Block Size Distribution from 2-D Measurements on Sections." Proceedings of the FRAGBLAST 5 Workshop on Measurement of Blast Fragmentation, Montreal, Quebec, Canada, 23-24 Aug., 1996, pp. 39-43.
28. L. Vincent, and P. Soille, "Watersheds in Digital Spaces: An Efficient Algorithm Based on Immersion Simulation." *IEEE Trans. Pattern Anal. Machine Intell.*, vol. 13, no. 6 (1991): :583-598.
29. George W. Snedecor, and William G. Cochran, *Statistical Methods*. 6th ed., (Iowa: The Iowa State University Press, Ames, Iowa, 1967).
30. "VDG-40 Measurement of Particle Size Distribution of Granular Mixtures." Commercial Catalogue for Laboratory Central Des Ponts and Chaussees (LCPC); also in VDG 40 Technical Bulletin, Ministere de l'Equipment, July 1995.
31. R. L. Weingart, and B. D. Prowell, "Specification Development Using the VDG-40 Videograder for Shape Classification of Aggregates." Proceedings of the 7th Annual Symposium, International Center of Aggregate Research, University of Texas, Austin, April 19-21, 1999.
32. Chetana Rao, and Erol Tutumluer, "A New Image Analysis Approach for Determination of Volume of Aggregates." Transportation Research Board, 79th Annual Meeting, Washington, D.C , January 9-13, 2000.
33. H. Kim, C. Browne, A. Rauch, and C. Haas, "Technical Aspects of Implementing Rapid Aggregate Gradation." Proceedings of the 8th Annual ICAR Symposium, International Center for Aggregates Research, University of Texas at Austin, April 12-14, 2000.
34. Chetana Rao, and Erol Tutumluer, "Flat and Elongated Ratio Determination Using the University of Illinois Image Analyzer." Proceedings of the 8th Annual ICAR

Symposium, International Center for Aggregates Research, University of Texas at Austin, April 12-14, 2000.

35. WipWare Inc. web site: <http://wipware.com>, July, 2000.

36. Micromeritics Corporation website: http://www.Micromeritics.com/ps_optisizer.html, July, 2000.

37. N. H. Mearz, and W. Zhou, "Flat and Elongated: Advances Using Digital Image Analysis." Proceedings of the 7th Annual ICAR Symposium, International Center for Aggregates Research, University of Texas at Austin, April 19-21, 1999.

38. N. H. Mearz, "Online Fragmentation Analysis: Achievements in the Mining Industry." Proceedings of the 7th Annual ICAR Symposium, International Center for Aggregates Research, University of Texas at Austin, April 19-21, 1999.

39. A. Rauch, C. Hass, and H. Kim, "State of the Art in Aggregate Classification." Proceedings of the 7th Annual ICAR Symposium, International Center for Aggregates Research, University of Texas at Austin, April 19-21, 1999.

40. T. C. Palangio, and N. H. Maerz, "Case Studies Using the Wipfrag Image Analysis System." FRAGBLAST 6th International Symposium for Rock Fragmentation By Blasting, Johannesburg, South Africa, August 8-12, 1999, pp. 117-120.

41. B. M. K. Bocoum, "Hatch Sieving of Cylindrical Particles Cascadography." (master's thesis, West Virginia University, n.d.).

APPENDIX I

Modeling Sample Statistics (Total of 501 particles)

Area : Projected area (mm^2)
Aps. : Aspect ratio
D_{maj} : Major diameter (mm)
D_{min} : Minor diameter (mm)
MN_{sig} : Non-normalized signature mean (mm)
VR_{sig} : Non-normalized signature variance (mm^2)
Mass : Particle actual mass (g)

<i>Area</i>	<i>Aps.</i>	<i>D_{maj}</i>	<i>D_{min}</i>	<i>MN_{sig}</i>	<i>VR_{sig}</i>	<i>Mass</i>
79.7623	1.0797	9.0093	8.3439	4.3932	0.3751	0.4110
43.6570	2.1019	8.8433	4.2073	3.1808	0.9354	0.2040
50.7597	1.0618	6.8671	6.4672	3.3289	0.2773	0.2940
63.7812	1.2011	8.7778	7.3084	3.8873	0.3601	0.3900
37.1462	1.2040	5.5286	4.5919	2.6133	0.1777	0.2640
50.1678	1.4524	8.0294	5.5286	3.4113	0.4535	0.2600
44.8408	1.2620	7.4402	5.8956	3.0841	0.2023	0.2780
53.1272	2.1019	8.8433	4.2073	3.5668	0.9646	0.2720
33.0030	1.0697	4.9120	4.5919	2.4312	0.1575	0.2420
22.3490	2.5000	3.2755	1.3102	1.7460	0.2320	0.2360
36.5543	1.3173	5.7814	4.3889	2.6613	0.1340	0.3060
31.2273	2.4512	6.4672	2.6384	2.4935	0.7110	0.2220
56.0867	2.9265	10.8826	3.7186	3.8627	1.8787	0.6000
31.8192	2.0487	6.4672	3.1568	2.5225	0.5574	0.1640
45.4327	1.4717	7.7661	5.2769	3.1783	0.3998	0.1650
37.1462	1.4626	6.2992	4.3068	2.7250	0.3054	0.1880
57.2705	1.1776	7.4180	6.2992	3.5148	0.2784	0.3100
49.5759	1.2620	7.4402	5.8956	3.3514	0.3253	0.3820
62.5975	1.6759	8.8433	5.2769	3.9591	0.8836	0.4890
36.5543	1.4626	6.2992	4.3068	2.7048	0.3180	0.2820
40.6975	2.5546	8.0644	3.1568	3.0127	0.7156	0.2510
44.2489	2.1019	8.8433	4.2073	3.1931	0.7903	0.1920
69.7001	1.3119	8.8990	6.7834	4.1040	0.3806	0.4270
76.8028	1.8238	11.5149	6.3136	4.4950	1.3156	0.5300
74.4353	1.0000	8.0294	8.0294	4.1791	0.2462	0.3160
41.2894	1.9585	7.3573	3.7567	2.9718	0.6607	0.2520
48.9840	1.1667	7.6806	6.5834	3.2703	0.2611	0.4100
36.5543	1.2040	5.5286	4.5919	2.6008	0.1789	0.3190
60.8218	1.2184	7.6747	6.2992	3.7048	0.4201	0.4940
67.3326	2.3898	11.7388	4.9120	4.2317	1.6890	0.5170
47.8002	1.4000	7.6806	5.4861	3.2664	0.3090	0.4040
51.3516	1.2287	8.0888	6.5834	3.3832	0.3439	0.3460
57.2705	1.3723	8.5279	6.2145	3.6654	0.5241	0.3990
50.7597	2.6974	10.0305	3.7186	3.6012	1.5517	0.3100
47.8002	1.6245	8.5723	5.2769	3.3323	0.7259	0.3520
50.7597	1.7544	8.0559	4.5919	3.2774	0.5542	0.2630
33.5949	1.5000	6.5834	4.3889	2.5218	0.1847	0.2130
41.8813	2.8190	8.8990	3.1568	3.2486	1.4370	0.3920
70.2920	1.6189	10.2212	6.3136	4.2535	0.7799	0.3850
54.3110	1.3723	8.5279	6.2145	3.4875	0.3252	0.3290
40.6975	2.1593	8.0294	3.7186	3.0389	0.9985	0.2570
47.8002	1.6759	8.8433	5.2769	3.3514	0.6560	0.3140
52.5353	1.0769	6.7834	6.2992	3.3669	0.1805	0.3740
37.7381	1.4626	6.2992	4.3068	2.8003	0.3753	0.2700
46.6164	1.6196	7.4372	4.5919	3.0853	0.3686	0.2120
43.6570	1.1204	6.3136	5.6350	3.0026	0.2523	0.3320

33.0030	1.2174	5.1220	4.2073	2.4590	0.1752	0.1760
63.1894	1.3674	8.6136	6.2992	3.7665	0.2506	0.5550
43.0651	1.0000	6.2992	6.2992	2.9938	0.1465	0.3910
43.0651	1.0000	6.2992	6.2992	2.9713	0.1298	0.2550
46.0246	1.4744	8.0888	5.4861	3.2029	0.4393	0.3420
30.0435	1.4047	5.2769	3.7567	2.2732	0.1943	0.3060
53.1272	2.2686	9.7704	4.3068	3.6921	1.2996	0.5570
41.8813	1.2476	6.5834	5.2769	2.9295	0.2953	0.2260
30.6354	1.5854	5.8956	3.7186	2.3848	0.2750	0.2000
32.4111	1.4633	5.4413	3.7186	2.4596	0.2747	0.2770
37.7381	1.2040	5.5286	4.5919	2.6308	0.1916	0.2800
36.5543	1.0000	5.4413	5.4413	2.6446	0.1123	0.3500
51.9434	3.4473	10.8826	3.1568	3.7306	2.0425	0.2010
60.8218	1.3344	8.9341	6.6955	3.7582	0.4630	0.3450
35.9624	1.8005	6.6955	3.7186	2.6568	0.4279	0.2670
48.3921	1.6347	8.0294	4.9120	3.3379	0.6171	0.2570
49.5759	2.4697	9.1838	3.7186	3.4110	1.0659	0.2140
67.9245	2.6033	12.3273	4.7352	4.2931	2.2148	0.5150
26.4922	1.3333	4.3889	3.2917	2.1192	0.2644	0.1270
33.0030	1.4633	5.4413	3.7186	2.4967	0.1826	0.1600
44.2489	1.4582	7.1625	4.9120	3.1100	0.3364	0.3870
36.5543	1.3084	5.6350	4.3068	2.7054	0.3693	0.2610
18.7976	1.0709	3.1568	2.9478	1.5118	0.1485	0.1700
30.6354	1.0000	4.5919	4.5919	2.2942	0.1235	0.2220
40.6975	1.0000	5.4413	5.4413	2.8456	0.2836	0.3210
57.8623	1.6096	8.8990	5.5286	3.7418	0.6895	0.2470
64.9650	2.0420	10.0305	4.9120	4.0201	0.9648	0.5710
54.9029	1.0769	6.7834	6.2992	3.4535	0.1838	0.1860
30.0435	1.4633	5.4413	3.7186	2.3338	0.2424	0.1620
46.6164	1.5296	7.5134	4.9120	3.2138	0.3943	0.3240
35.3705	1.1182	5.9007	5.2769	2.5878	0.1315	0.1350
38.9219	1.4626	6.2992	4.3068	2.7973	0.3025	0.2180
55.4948	2.0046	9.6398	4.8088	3.6847	0.9862	0.2860
42.4732	1.3850	7.3084	5.2769	2.9755	0.2836	0.1770
38.3300	1.0000	5.4413	5.4413	2.7366	0.1815	0.2730
69.7001	1.2922	8.8433	6.8436	4.1182	0.5430	0.2860
35.9624	1.2476	6.5834	5.2769	2.6198	0.1478	0.4200
52.5353	1.4524	8.0294	5.5286	3.4573	0.4545	0.3340
47.2083	1.7474	8.4031	4.8088	3.3484	0.7351	0.3450
38.9219	2.1949	8.1619	3.7186	2.9864	1.0482	0.1800
31.2273	1.9954	6.2992	3.1568	2.4774	0.6235	0.1510
57.2705	2.0420	10.0305	4.9120	3.8060	1.1974	0.3820
31.2273	1.0000	4.5919	4.5919	2.3441	0.1667	0.1780
48.9840	1.0000	6.2992	6.2992	3.2433	0.2002	0.3010
69.7001	2.0832	11.5174	5.5286	4.3162	1.6979	0.3750
66.1488	1.6551	10.4496	6.3136	4.0515	0.8678	0.5930
76.8028	2.8774	12.3923	4.3068	4.5885	2.2085	0.3260
60.8218	1.5982	8.6963	5.4413	3.6759	0.5610	0.3850
60.8218	1.0000	7.1625	7.1625	3.7306	0.2956	0.2880
53.7191	1.6616	8.1619	4.9120	3.6038	0.7141	0.3610
24.7165	1.0000	3.5812	3.5812	1.9372	0.1008	0.2080
43.0651	1.5546	6.6955	4.3068	3.0421	0.4013	0.2820
67.3326	1.5217	10.4496	6.8671	4.1082	0.8122	0.4110
79.7623	1.0033	8.0559	8.0294	4.4157	0.4360	0.4070
33.0030	1.0697	4.9120	4.5919	2.4179	0.1533	0.1650
33.5949	1.9954	6.2992	3.1568	2.5905	0.5235	0.1510
36.5543	1.0000	5.4413	5.4413	2.6449	0.1179	0.2780
57.2705	1.8697	9.1838	4.9120	3.7085	0.6413	0.2920
61.4137	1.8143	10.0305	5.5286	3.9523	1.0023	0.2100
60.8218	1.0000	7.5134	7.5134	3.7840	0.3584	0.3200
47.2083	2.0663	8.8990	4.3068	3.3933	1.0446	0.1650
46.6164	2.3931	8.8990	3.7186	3.3300	1.1587	0.1860
44.2489	1.6631	7.1625	4.3068	3.0881	0.3955	0.3050
35.3705	1.1182	5.9007	5.2769	2.5878	0.1315	0.2060
56.6786	1.2059	8.4147	6.9779	3.6144	0.4927	0.3510
44.8408	1.0709	6.3136	5.8956	3.0628	0.2454	0.4020
41.8813	1.9261	7.1625	3.7186	3.0241	0.5558	0.3260
54.3110	1.4524	8.0294	5.5286	3.5507	0.4853	0.3670
61.4137	1.0357	7.4180	7.1625	3.6906	0.1546	0.3200
54.9029	2.0663	8.8990	4.3068	3.6390	0.9993	0.3190

34.7786	1.0697	4.9120	4.5919	2.5139	0.1827	0.2710
35.9624	2.0487	6.4672	3.1568	2.7046	0.4961	0.2830
64.3731	1.0434	8.4147	8.0644	3.8273	0.2905	0.3370
52.5353	1.8117	8.8990	4.9120	3.5763	1.0077	0.3250
46.0246	1.4876	8.7778	5.9007	3.1620	0.5225	0.2760
47.2083	2.0358	9.6398	4.7352	3.4471	1.1268	0.2760
67.3326	1.7163	9.3388	5.4413	3.8948	0.6192	0.4980
58.4542	2.6742	11.5174	4.3068	4.0483	2.1783	0.5730
83.9055	3.1126	14.7389	4.7352	5.0951	3.2102	0.8110
54.9029	1.9395	9.1838	4.7352	3.6570	0.8641	0.3090
33.5949	2.2689	7.1625	3.1568	2.6538	0.8001	0.2760
51.9434	2.2912	9.6398	4.2073	3.5747	1.1322	0.4320
48.3921	2.4348	10.2441	4.2073	3.4401	1.2769	0.3730
41.8813	2.2438	8.3439	3.7186	3.1032	0.9808	0.3240
57.8623	1.6313	9.0187	5.5286	3.7141	0.5357	0.3490
53.1272	1.0256	6.8671	6.6955	3.4124	0.1597	0.3260
43.6570	1.0709	6.3136	5.8956	2.9910	0.2679	0.3280
59.0461	1.9316	10.2212	5.2916	3.8183	0.9765	0.4050
37.7381	1.4626	6.2992	4.3068	2.7547	0.3194	0.1860
62.0056	2.0420	10.0305	4.9120	3.9066	1.0494	0.5120
66.1488	1.7673	9.7704	5.5286	4.0812	0.9401	0.5220
38.9219	1.0000	5.4413	5.4413	2.7532	0.1187	0.2040
40.6975	1.3690	6.5834	4.8088	2.8889	0.2770	0.3460
40.1057	1.2040	5.5286	4.5919	2.8185	0.2356	0.2820
44.8408	1.4773	6.7834	4.5919	3.0272	0.2606	0.3270
97.5190	1.3237	10.6284	8.0294	4.9230	0.6314	1.0380
122.3783	3.1299	18.3675	5.8685	6.2892	5.2102	1.2680
72.6596	1.0000	8.0644	8.0644	4.2074	0.3274	0.7870
54.3110	1.8938	8.6963	4.5919	3.4368	0.8696	0.5170
128.2972	1.5572	14.3007	9.1838	5.8036	1.0903	0.8830
98.1109	1.1434	10.1751	8.8990	5.0490	0.6294	0.6040
45.4327	1.1608	6.8436	5.8956	3.1137	0.2472	0.2860
73.2515	1.0000	8.3439	8.3439	4.2068	0.3146	0.8790
95.1514	3.5566	15.3177	4.3068	5.3553	3.8780	1.1410
54.9029	1.3708	8.0888	5.9007	3.5325	0.3817	0.4320
122.9702	1.8231	14.6214	8.0202	5.9582	2.2441	1.0310
82.7217	1.4051	10.4496	7.4372	4.5683	0.5869	0.9590
93.9676	1.2036	9.8240	8.1619	4.8075	0.3008	1.1830
53.1272	1.4238	7.5134	5.2769	3.4675	0.5402	0.5170
118.2351	1.7139	14.3007	8.3439	5.6099	1.4745	1.0670
69.1083	1.0000	8.0294	8.0294	4.0068	0.1911	0.2800
98.1109	1.5763	12.7118	8.0644	5.1119	1.1307	0.9050
157.2998	3.3876	21.9086	6.4672	7.1604	8.2957	1.3560
72.0677	1.9533	10.6284	5.4413	4.1481	1.1642	0.6600
105.2135	1.3094	12.6220	9.6398	5.1861	0.5905	0.5620
82.7217	1.0000	8.8990	8.8990	4.4716	0.3329	0.5060
124.1540	1.1827	12.0890	10.2212	5.7300	0.5339	0.6500
72.6596	1.0120	8.4437	8.3439	4.1994	0.4167	0.8430
99.8865	1.0000	10.6434	10.6434	5.0043	0.4043	1.2490
80.3542	1.8718	11.5174	6.1531	4.6089	1.3237	0.6800
80.3542	1.9163	12.0989	6.3136	4.7217	1.8847	0.6550
62.5975	1.0357	7.4180	7.1625	3.7537	0.3230	0.5900
48.9840	1.1101	7.3084	6.5834	3.2388	0.2388	0.3540
59.6380	1.0000	7.1625	7.1625	3.6795	0.1713	0.5200
111.7243	1.0000	12.0989	12.0989	5.3546	0.3968	0.7970
63.7812	1.6056	9.8796	6.1531	4.0123	0.6731	0.5050
80.9460	1.0000	8.8990	8.8990	4.4364	0.2540	0.6450
98.7027	3.5680	17.5257	4.9120	5.8114	5.6451	0.8890
56.6786	1.5167	9.6398	6.3559	3.6931	0.7591	0.7870
76.2109	1.3768	10.2441	7.4402	4.3723	0.6003	0.8580
72.6596	2.5648	12.5983	4.9120	4.5287	2.2169	0.5890
52.5353	1.3633	7.4180	5.4413	3.3213	0.3117	0.5370
92.1920	1.9680	12.7275	6.4672	4.9321	1.5020	0.9380
81.5379	2.0505	12.0890	5.8956	4.5949	1.2627	0.5450
169.1376	1.6615	17.3625	10.4496	6.8799	1.8186	1.0680
75.6190	1.5690	10.6434	6.7834	4.3507	0.7751	0.4840
91.0082	1.0034	9.2154	9.1838	4.7871	0.4857	0.8820
115.8675	2.1039	15.0692	7.1625	5.5192	2.5726	1.0780
80.9460	1.5741	11.0096	6.9943	4.5338	0.8869	0.4130
56.0867	1.0000	7.1625	7.1625	3.5215	0.1204	0.4120

80.3542	1.2605	9.2154	7.3107	4.4068	0.5238	0.8500
86.8649	1.7530	11.7369	6.6955	4.6776	1.0261	0.4640
88.6406	1.3237	10.6284	8.0294	4.6686	0.5023	0.9980
84.4974	1.4229	11.0504	7.7661	4.6623	0.8694	1.0230
72.0677	1.0033	8.0559	8.0294	4.1272	0.3597	0.7750
153.1566	2.4466	20.5592	8.4031	6.9945	4.2900	1.7210
127.1135	1.5792	16.1776	10.2441	5.9888	1.9654	1.4900
147.8296	2.5211	18.4308	7.3107	6.4370	4.3321	1.0570
57.2705	2.0535	9.8750	4.8088	3.6762	0.9261	0.4060
67.9245	1.0000	8.5723	8.5723	4.0060	0.3476	0.7900
86.8649	1.4728	10.7670	7.3107	4.6960	0.7470	0.5360
55.4948	1.8938	8.6963	4.5919	3.4895	0.9060	0.5340
112.3162	1.1317	11.0571	9.7704	5.3243	0.3272	0.6100
95.7433	2.4849	13.5210	5.4413	5.0637	2.6781	0.9050
67.3326	1.7163	9.3388	5.4413	3.9201	0.7698	0.4730
54.9029	2.4713	10.6434	4.3068	3.7807	1.6268	0.5260
44.8408	1.6196	7.4372	4.5919	3.0625	0.4546	0.5050
69.1083	1.0357	7.4180	7.1625	3.9841	0.1912	0.4710
116.4594	2.8925	17.7980	6.1531	6.0134	4.7829	0.8650
85.0893	1.5438	11.0571	7.1625	4.5573	0.8167	0.6690
85.6812	2.0060	13.7757	6.8671	4.9237	2.0698	0.6700
105.2135	1.6851	11.9022	7.0632	5.3080	1.1652	0.8640
76.2109	1.3337	10.0209	7.5134	4.3029	0.3980	0.6930
70.2920	2.9252	12.5983	4.3068	4.5139	2.6451	0.6220
63.7812	2.3290	10.0305	4.3068	4.0035	1.1576	0.3670
120.0108	2.4082	15.1698	6.2992	5.6529	2.8124	1.0490
63.7812	1.3674	8.6136	6.2992	3.7999	0.3973	0.5770
118.8270	1.6250	14.2640	8.7778	5.6956	1.5141	0.6620
87.4568	1.5318	11.2700	7.3573	4.7695	1.0591	0.4430
73.2515	1.8544	10.8826	5.8685	4.3136	1.0369	0.3310
67.3326	2.3296	12.3273	5.2916	4.3325	2.1516	0.4060
128.2972	1.9826	14.2005	7.1625	5.7744	2.2621	1.2750
69.1083	1.1651	8.5723	7.3573	4.0988	0.4765	0.7530
68.5164	1.5615	10.2796	6.5834	4.1483	0.6278	0.5820
53.7191	1.0221	6.8436	6.6955	3.4504	0.2299	0.6650
65.5569	1.4119	9.8750	6.9943	3.9971	0.4907	0.4850
127.7053	1.5318	12.9345	8.4437	5.9032	1.1644	0.9290
120.6027	1.4357	12.9345	9.0093	5.8036	1.6456	0.4750
108.7649	1.7631	13.9559	7.9153	5.4734	1.4735	0.6470
129.4810	2.1013	16.9278	8.0559	6.2150	3.0732	0.5330
101.0703	1.3750	12.0695	8.7778	5.1958	0.8500	0.9400
95.1514	1.0000	9.8796	9.8796	4.8781	0.3659	1.1040
160.8512	1.4083	14.4265	10.2441	6.9231	3.3571	1.1130
112.3162	1.7557	14.1440	8.0559	5.5926	1.6225	1.0800
141.9107	1.4601	15.2575	10.4496	6.3162	1.3339	1.7830
114.6838	1.1245	11.1603	9.9249	5.5244	0.5555	0.7640
83.9055	1.0831	8.6963	8.0294	4.5996	0.7168	0.6710
72.0677	1.0033	8.0559	8.0294	4.0961	0.2893	0.4330
73.8434	1.7298	10.6434	6.1531	4.3595	0.9276	0.2720
77.9866	1.5848	9.9829	6.2992	4.2729	0.5188	0.6050
145.4620	1.4168	14.2751	10.0753	6.3505	1.3536	1.6020
69.1083	1.0000	8.1619	8.1619	4.0320	0.2186	0.7120
136.5837	1.8083	14.5193	8.0294	5.9676	1.9360	1.8280
85.0893	1.6873	10.6284	6.2992	4.4682	0.9145	0.4890
160.2593	1.7087	17.9611	10.5114	6.8611	2.9235	1.3810
86.8649	1.7618	12.0989	6.8671	4.8367	1.5427	0.6270
86.8649	1.0284	10.5114	10.2212	4.6554	0.3932	0.7240
136.5837	2.1622	17.3411	8.0202	6.3827	3.4223	0.6100
134.8080	1.0439	13.1384	12.5857	5.9650	0.5768	1.2600
120.6027	1.5383	12.3923	8.0559	5.7234	1.0930	0.6210
156.1160	1.0000	12.9345	12.9345	6.5020	0.6826	1.6040
238.3887	2.7158	24.1677	8.8990	8.3593	7.8828	2.0820
105.2135	1.7631	13.9559	7.9153	5.4010	2.0249	1.1520
80.3542	1.5690	10.6434	6.7834	4.5243	0.7366	0.7510
182.7511	1.2655	15.3107	12.0989	7.1217	1.3136	3.8620
156.7079	2.5239	20.2421	8.0202	7.0573	5.0621	1.5620
86.8649	1.3938	9.9829	7.1625	4.5482	0.5018	0.8300
157.2998	1.1924	15.3490	12.8722	6.6275	1.4381	2.4470
76.2109	1.7899	11.2750	6.2992	4.2974	1.0705	0.6260
86.8649	1.7093	10.7670	6.2992	4.6279	1.0659	0.6360

72.6596	1.3806	8.6963	6.2992	4.1058	0.4990	0.3330
108.1730	1.0000	11.7388	11.7388	5.2987	0.4603	1.2190
83.3136	1.1477	9.2154	8.0294	4.4895	0.4281	0.6760
64.9650	1.4546	9.1838	6.3136	4.0058	0.8988	0.6020
122.9702	1.9311	14.3249	7.4180	5.9500	2.3281	1.2670
151.9728	1.4082	14.7147	10.4496	6.4686	1.3254	1.6760
89.8244	1.1535	10.5942	9.1840	4.8459	0.8047	0.8080
88.0487	1.1350	9.4705	8.3439	4.6632	0.2890	0.9320
75.0271	1.0000	8.0294	8.0294	4.2545	0.3175	0.3860
135.3999	1.2171	12.8947	10.5942	6.1248	0.9791	1.2350
73.8434	1.8075	10.4496	5.7814	4.3545	1.0245	0.3710
106.9892	2.7984	15.4710	5.5286	5.6280	3.2864	0.8800
103.4379	1.5116	13.8828	9.1840	5.3700	2.0040	1.3090
55.4948	1.6428	8.4147	5.1220	3.6611	0.7764	0.5750
112.9081	1.4087	12.5857	8.9341	5.4463	0.6789	1.4170
147.2377	1.2629	13.9559	11.0504	6.3830	1.1420	0.8820
104.0297	1.1724	10.7670	9.1838	5.1168	0.6026	1.0210
133.0323	1.3361	13.6872	10.2441	5.9262	1.0655	1.0970
135.3999	1.3689	15.5176	11.3361	6.0934	1.3459	1.0030
125.9297	1.8997	15.3661	8.0888	5.8985	1.8637	0.4500
94.5595	1.3938	9.9829	7.1625	4.8026	0.8350	1.1420
44.8408	1.4582	7.1625	4.9120	3.1474	0.4339	0.5360
111.7243	1.3075	11.5628	8.8433	5.3552	0.4970	1.3400
146.0539	2.0132	17.3411	8.6136	6.5336	3.0532	1.1470
143.0945	1.3097	14.6168	11.1603	6.2917	1.3589	1.5340
280.4129	1.4872	19.7317	13.2678	8.7393	1.7457	3.0610
304.6804	1.2095	20.3264	16.8063	9.4210	1.5487	4.1600
262.0643	1.1998	18.2270	15.1911	8.4743	0.8011	5.0950
256.1454	1.5802	19.7183	12.4785	8.4284	2.3970	4.3470
291.0669	1.5797	24.2664	15.3612	9.4516	4.3773	5.4410
193.9970	1.0000	16.7750	16.7750	7.3451	1.0168	1.9110
228.3266	2.4813	24.8890	10.0305	8.4393	7.7350	1.9320
138.9512	1.4337	14.0082	9.7704	6.0090	0.7346	1.9450
295.8020	1.4380	19.0793	13.2678	9.0719	2.6343	3.5680
416.5476	1.5943	27.3336	17.1445	11.1546	4.3778	6.3480
299.9453	1.6840	22.3429	13.2678	9.1885	4.3493	2.8850
279.8210	1.3292	19.9659	15.0207	8.8602	1.4852	3.4930
199.3240	1.3636	17.9545	13.1667	7.5776	1.4872	3.0340
339.6019	1.0000	19.5409	19.5409	9.8057	0.7566	4.9470
183.3430	2.0245	18.5929	9.1838	7.2541	3.4912	1.8700
156.1160	1.6469	16.1786	9.8240	6.6206	1.6480	3.1620
231.8779	1.2636	19.2795	15.2575	8.1593	1.5376	4.2230
200.5078	2.0375	20.3398	9.9829	7.7205	3.5845	2.8950
263.8400	1.5252	20.6226	13.5210	8.8221	2.8419	2.8310
299.9453	1.2684	21.1665	16.6879	9.2899	1.9715	3.8300
147.8296	1.8638	16.5857	8.8990	6.3042	2.4060	1.5020
176.8322	1.2881	14.8360	11.5174	6.8609	0.5728	1.7210
128.2972	1.0647	12.0695	11.3361	5.9320	0.7837	1.4950
186.3024	1.0725	15.1698	14.1440	7.0951	0.3969	1.3030
143.6864	1.4582	14.3249	9.8240	6.3319	1.2873	1.0850
143.0945	1.1478	13.2197	11.5174	6.1067	0.6325	1.1470
325.3965	1.0940	20.5308	18.7673	9.7433	1.1664	5.6810
214.1212	1.4107	18.6006	13.1852	7.8445	1.5786	1.9300
214.1212	1.6435	18.5306	11.2750	7.8287	1.9900	3.1500
173.8727	1.6667	16.4584	9.8750	7.1676	2.4274	2.2430
159.6674	2.4812	19.9000	8.0202	7.1265	5.5197	1.6130
398.7909	1.8503	29.0713	15.7114	11.1853	6.0729	9.0520
230.1023	1.0239	16.8875	16.4939	8.0816	1.0446	4.7610
167.9538	1.2941	16.3346	12.6220	6.8399	1.5287	1.3050
268.5751	1.2373	18.5929	15.0267	8.8129	2.2491	2.2800
127.1135	1.0593	11.2750	10.6434	5.7089	0.2168	1.7100
124.1540	1.7636	15.1911	8.6136	5.9472	2.1015	0.8450
176.2403	1.8642	17.1795	9.2154	7.1428	2.7149	2.5200
245.4914	1.1267	16.2913	14.4596	8.4939	2.2017	4.0500
289.2912	2.5732	25.1415	9.7704	9.3025	8.6492	3.7100
284.5561	1.0329	17.3927	16.8389	8.9552	1.1641	2.2700
286.3318	1.0326	18.7847	18.1915	9.0178	0.7478	3.8030
237.2049	1.7153	21.2568	12.3923	8.2121	3.9021	2.9000
240.7563	1.2500	19.3971	15.5176	8.3865	2.3694	4.3000
333.0911	1.2251	19.1725	15.6503	9.7797	1.6583	7.6170

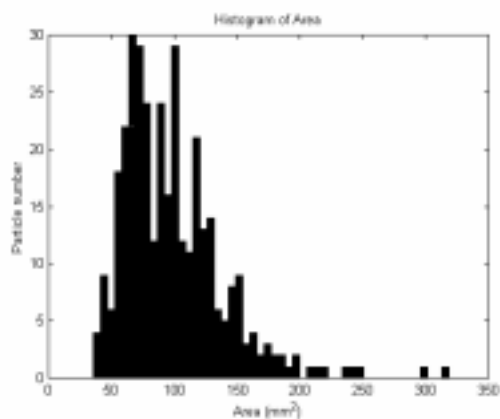
160.8512	1.0668	13.2197	12.3923	6.5257	0.3560	2.5230
227.7347	1.0000	15.5323	15.5323	7.9923	0.6492	4.0220
254.9616	1.5853	23.1716	14.6168	8.7629	3.1614	3.5210
193.4051	1.6755	17.7327	10.5833	7.4357	2.2669	2.6130
167.3620	1.2042	13.8693	11.5174	6.6220	0.6591	1.6630
148.4215	1.8160	17.2172	9.4811	6.6099	2.6152	2.1730
238.9806	1.4551	17.6054	12.0989	8.2170	2.2423	2.2680
224.7753	1.0000	18.4793	18.4793	7.9968	1.2383	1.8400
109.9486	1.0217	9.9829	9.7704	5.2791	0.2405	1.7200
207.6105	1.7000	18.6529	10.9723	7.9201	3.7296	2.1400
307.0479	1.1176	19.3807	17.3411	9.3653	1.5228	5.4370
273.9021	1.0000	19.2128	19.2128	8.8108	0.9249	4.0450
156.7079	1.0941	14.4265	13.1852	6.5729	0.8417	2.2480
315.9263	1.1885	22.3384	18.7953	9.6034	2.1346	5.3280
386.3612	1.1834	21.7367	18.3675	10.5406	1.5157	3.5830
169.7295	1.2421	13.2197	10.6434	6.6895	0.6965	1.5230
282.7805	1.5265	22.0720	14.4596	8.9958	2.8131	3.3370
193.4051	1.8609	19.4455	10.4496	7.5777	3.8607	2.0920
165.5863	2.2949	18.4271	8.0294	6.6796	4.0206	2.3270
217.0807	1.4458	18.6435	12.8947	8.0630	2.6901	4.0610
196.9564	1.6341	17.3927	10.6434	7.3104	2.4078	1.5760
288.6994	1.8557	22.9960	12.3923	9.0316	4.7178	5.1130
312.9668	1.0000	18.5306	18.5306	9.4348	0.6829	4.2080
247.8590	1.8456	21.2568	11.5174	8.2473	3.0892	3.8650
353.8072	1.4054	22.3429	15.8977	9.9314	2.2130	5.2430
379.2585	1.5553	26.2917	16.9051	10.6514	5.6575	8.5850
146.6458	1.4553	15.1911	10.4382	6.4036	1.3961	2.3370
124.1540	1.3398	11.9225	8.8990	5.6337	1.0788	1.4420
130.6648	1.3530	13.2197	9.7704	5.8048	0.6729	1.8940
139.5431	1.0000	12.0989	12.0989	6.0535	0.4864	2.3600
236.0212	1.7784	20.8764	11.7388	8.1456	3.2111	2.1000
215.3050	1.3002	16.1118	12.3923	7.6033	0.9857	1.5310
175.6484	1.0738	13.8884	12.9345	6.9363	0.6916	2.2800
133.6242	1.0000	11.6101	11.6101	5.9559	0.5937	2.1780
227.7347	1.2226	16.6315	13.6032	7.9427	1.1907	3.1700
190.4457	1.3387	16.5890	12.3923	7.1802	1.5797	2.0180
216.4888	2.2352	22.1839	9.9249	8.2164	6.2157	2.9910
181.5673	1.3958	16.8875	12.0989	7.0841	1.3517	2.1810
204.6510	1.6017	17.2080	10.7437	7.4279	1.4859	3.4400
151.3809	1.3444	14.4439	10.7437	6.3516	1.1559	2.0000
121.7864	1.3829	12.3062	8.8990	5.6292	1.0629	1.7790
105.2135	1.6127	12.9345	8.0202	5.3522	1.4913	0.8350
273.3102	1.0539	18.1451	17.2172	8.8755	1.2537	3.2320
166.7701	1.0256	12.9204	12.5983	6.7010	0.5924	2.5890
214.7131	1.1646	16.4718	14.1440	7.6406	1.1268	1.9530
170.3214	1.5629	16.3320	10.4496	6.9448	1.9633	1.8770
150.1972	1.0000	12.3923	12.3923	6.3671	0.6300	0.9730
142.5026	1.0000	10.6434	10.6434	6.1383	0.5685	1.8620
250.8184	1.0000	17.6527	17.6527	8.3805	0.4271	4.3330
238.9806	1.4870	18.4271	12.3923	8.0286	1.8552	2.0250
310.0074	1.2102	19.3214	15.9650	9.4680	2.8160	5.0120
255.5535	1.2948	20.0926	15.5176	8.6937	2.4521	4.7230
225.9590	1.2888	17.9865	13.9559	8.0995	2.3585	4.5100
196.9564	1.4958	16.2784	10.8826	7.2874	1.3673	3.3020
166.1782	1.4860	14.5193	9.7704	6.5866	1.2616	1.5310
311.7831	1.4941	22.7768	15.2447	9.7369	3.7023	5.9860
177.4241	1.5526	15.1698	9.7704	6.8190	1.4753	2.0470
214.1212	1.0145	15.2447	15.0267	7.7412	0.9347	3.7950
140.7269	1.2573	13.1384	10.4496	6.2192	1.6679	1.3900
186.8943	1.9974	17.7751	8.8990	7.1123	3.6970	2.2530
186.3024	2.2173	19.7317	8.8990	7.1011	3.7621	1.3630
167.3620	1.5112	16.4459	10.8826	6.7301	1.5265	1.0970
130.0729	1.0000	11.5174	11.5174	5.7904	0.1674	0.9300
296.9858	1.0675	20.0335	18.7673	9.2277	1.2493	4.5110
204.0591	1.1639	16.8293	14.4596	7.6064	1.7898	1.7980
305.2723	1.3733	22.0771	16.0759	9.4974	2.2703	5.8780
170.9133	1.7426	17.4054	9.9881	7.0173	2.5224	2.4000
141.9107	1.4296	15.0267	10.5114	6.3161	1.8291	2.2870
287.5156	1.5023	23.6029	15.7114	9.2533	3.0566	3.3020
141.3188	1.6671	15.3107	9.1838	6.2074	1.9438	1.1530

233.6536	1.6942	20.1643	11.9022	8.0649	2.8011	4.6500
273.3102	1.5766	21.2222	13.4605	8.7381	2.4405	5.5050
163.8106	2.3838	17.9100	7.5134	6.9738	4.8760	2.0500
314.7425	1.0439	18.4271	17.6527	9.3812	1.0481	4.7070
581.09	1.49	31.75	21.28	13.27	5.59	10.7100
544.40	2.04	32.89	16.11	13.11	11.85	11.8720
452.06	1.00	22.16	22.16	11.44	0.89	10.5750
465.67	1.37	26.08	19.03	11.85	4.06	13.1580
556.83	1.64	30.59	18.67	12.69	6.37	12.0200
572.81	1.26	29.04	22.97	12.89	3.22	18.1270
558.60	1.02	26.09	25.66	12.80	1.47	13.8900
669.28	1.36	30.31	22.25	13.93	4.96	12.0110
748.60	1.41	32.21	22.92	14.74	5.74	10.1970
597.67	1.19	26.26	22.04	13.10	2.26	9.5780
427.20	1.89	29.43	15.53	11.33	7.59	8.0010
688.22	1.40	33.77	24.20	14.33	6.45	16.2100
587.01	2.04	36.54	17.95	14.30	20.35	15.9500
674.61	1.00	29.07	29.07	14.16	2.50	14.8450
676.98	1.48	35.64	24.11	14.68	11.41	14.9550
784.70	1.33	34.42	25.80	15.48	4.87	16.1830
532.56	1.31	27.40	20.91	12.43	2.72	12.7140
809.56	1.99	43.73	21.93	16.51	19.12	18.6390
399.38	1.00	23.99	23.99	10.83	3.80	13.5690
389.91	1.07	21.74	20.24	10.66	1.69	7.1320
483.43	1.15	25.95	22.51	12.08	4.09	14.3340
509.47	1.00	25.72	25.72	12.37	2.79	14.1000
472.78	1.00	26.20	26.20	11.87	2.15	10.3300
669.28	1.21	29.04	24.09	13.93	2.29	11.1010
548.54	1.40	29.81	21.22	12.64	5.12	13.8000
072.36	2.10	46.99	22.35	17.98	20.13	26.2380
682.31	1.00	28.39	28.29	14.18	1.58	16.4900
637.91	1.03	24.64	23.91	13.68	2.82	14.3610
671.06	1.34	37.31	27.83	14.39	6.17	16.3100
630.22	1.66	31.31	18.90	13.55	6.84	18.1430
631.40	1.68	34.11	20.29	13.56	7.21	16.2000
367.42	1.29	23.02	17.91	10.41	3.00	8.9150
620.16	1.47	31.39	21.38	13.53	6.67	16.2880
524.27	1.03	27.33	26.53	12.55	2.64	6.2300
515.99	1.19	25.79	21.62	12.21	2.26	11.0210
547.95	1.35	29.50	21.93	13.07	6.69	15.2630
533.74	1.69	31.93	18.90	12.80	8.01	12.2820
852.77	2.25	45.79	20.38	17.03	23.80	23.1000
467.45	1.02	24.18	23.60	11.85	4.15	12.1200
507.70	1.04	23.11	22.16	12.19	2.84	13.0680
534.33	1.05	24.38	23.22	12.44	1.01	8.0100
382.81	1.82	26.08	14.30	11.20	8.37	9.0010
542.62	1.33	31.42	23.60	12.83	4.63	16.5500
727.29	1.38	34.11	24.68	14.45	3.89	10.5530
605.95	1.22	28.55	23.48	13.26	2.10	13.7730
640.28	1.20	27.57	22.92	13.60	2.04	10.2980
427.79	1.00	23.30	23.30	11.29	2.96	11.4800
436.67	1.00	20.41	20.41	11.22	1.66	10.7130
520.13	1.34	27.09	20.29	12.26	3.35	10.1970
525.46	1.00	25.50	25.50	12.49	2.71	9.4190
456.20	1.31	26.78	20.50	11.73	3.14	6.8400
468.6339	1.7363	30.3822	17.4982	12.0923	7.0839	9.4850
459.7555	1.3033	26.4395	20.2870	11.4271	1.8524	6.1390
671.0602	1.0000	29.7762	29.7762	14.1421	1.6282	11.1570
504.7391	1.1253	26.7298	23.7537	12.2484	2.4358	10.9750
514.2094	1.0841	25.3312	23.3670	12.3166	2.2577	12.4230
446.1420	1.0000	22.3533	22.3533	11.5191	2.3569	11.2200
426.0178	1.0721	20.2609	18.8975	11.1532	2.1963	5.7050
423.0583	1.6708	28.1178	16.8293	11.4429	5.9909	8.1560
737.9437	1.9448	38.4287	19.7593	14.8512	11.5347	18.5320
504.1472	1.0375	25.7893	24.8580	12.2096	2.1089	6.9000
562.1524	1.0926	25.5004	23.3401	12.7735	1.5068	10.4440
626.0765	1.7723	37.7268	21.2867	14.0071	11.9240	15.5310
444.9583	1.0000	23.0347	23.0347	11.4245	1.5698	8.4590
427.7935	1.0000	21.2867	21.2867	11.1655	1.6755	12.0010
415.3638	2.0687	31.0859	15.0267	11.3523	9.2711	7.7910

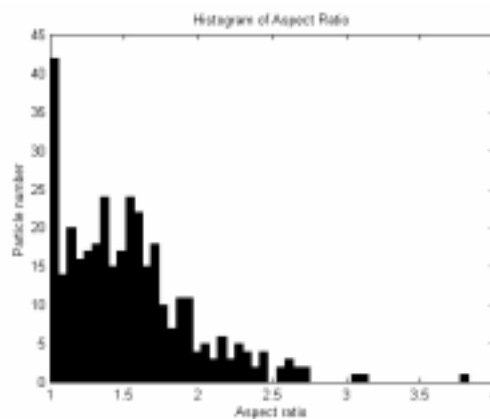
534.9255	1.0310	25.2444	24.4858	12.7001	2.8860	10.9510
691.1844	1.3684	35.5063	25.9477	14.6260	5.8700	16.2770
514.2094	1.4102	27.5567	19.5409	12.1605	4.1793	6.3610
444.9583	1.0738	22.7511	21.1884	11.5378	2.8463	8.5550
475.1446	1.3893	27.6462	19.9000	11.9212	4.3961	10.9650
494.6770	1.0000	25.0686	25.0686	12.0026	0.9314	8.9800
479.2879	1.1763	24.2584	20.6226	11.8091	2.4841	9.7150
584.0524	1.1339	26.9886	23.8015	13.0513	2.6182	12.9830
678.1628	1.1289	30.1384	26.6969	14.0391	1.7422	13.1530
856.3217	1.5543	37.0638	23.8465	15.8469	8.2670	10.8610
582.8686	1.5518	31.5810	20.3517	13.2787	6.2631	4.8260
630.2198	1.6099	32.8632	20.4135	13.5947	7.1258	14.4650
443.7745	1.0000	23.9929	23.9929	11.6009	3.3615	7.7630
552.0903	1.0000	25.3410	25.3410	12.8485	3.1034	10.9800
496.4527	1.0000	25.1713	25.1713	12.1781	2.3412	10.8150
501.1878	1.0000	24.0883	24.0883	12.1034	1.3417	13.1830
454.4285	1.0000	25.5594	25.5594	11.5097	1.0172	7.5730
671.6520	1.3153	30.6987	23.3401	14.2797	6.9476	14.9100
662.7737	2.4538	40.8097	16.6315	14.8398	17.7264	14.3110
659.2224	1.2428	31.3146	25.1967	14.0829	5.5969	13.7600
337.2343	1.5692	22.4792	14.3249	10.0383	5.1795	13.5030
692.9601	1.3256	35.9730	27.1377	14.4843	4.6877	13.3720
464.4906	1.8380	28.4393	15.4732	12.1970	7.8637	7.4730
388.1368	1.4175	27.9771	19.7370	10.8048	3.3067	11.0270
640.2819	1.7518	36.0891	20.6014	14.3510	12.2876	11.2180
397.0152	1.5948	26.5235	16.6315	10.9940	4.9561	5.4000
537.8850	1.0211	24.3025	23.8015	12.5737	3.4042	10.4600
550.3146	2.7791	38.4114	13.8214	14.0220	22.9717	6.9080
661.5899	1.1436	28.2243	24.6804	13.8712	2.6678	10.2410
597.0739	1.4657	30.8348	21.0370	13.4677	4.0772	10.4360
415.9557	2.0901	28.3562	13.5668	11.3975	7.2165	4.7590
544.3957	1.0804	27.3999	25.3614	12.7614	2.9944	12.0180
453.8366	1.9514	31.3006	16.0404	12.1155	9.9215	11.0930
513.0256	1.1578	24.8785	21.4874	12.1806	1.5118	11.2600
329.5398	1.4352	24.9653	17.3953	10.0674	4.4330	5.6810

APPENDIX II

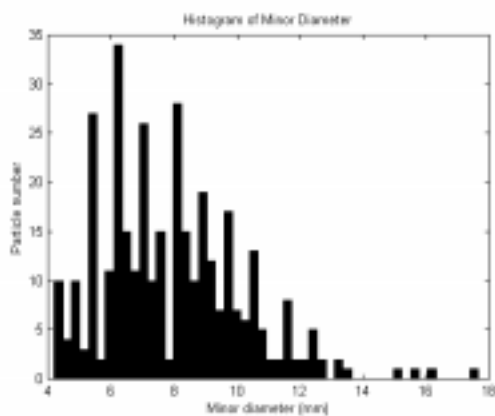
Histogram of Model Testing Samples (Total of 8 batches)



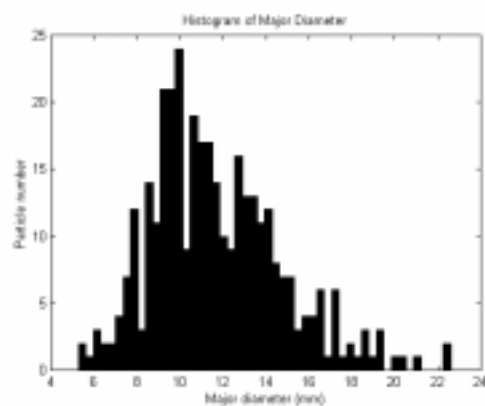
(a) projected area (mm^2)



(b) aspect ratio

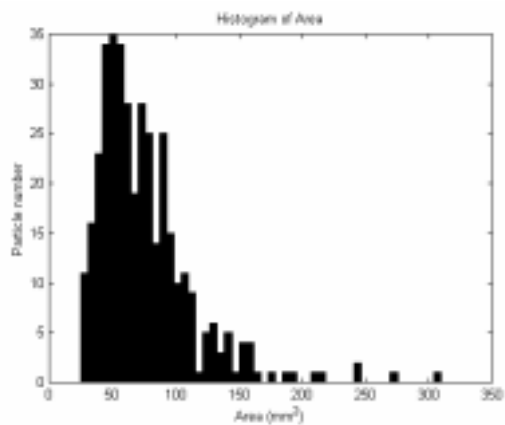


(c) minor diameter (m)

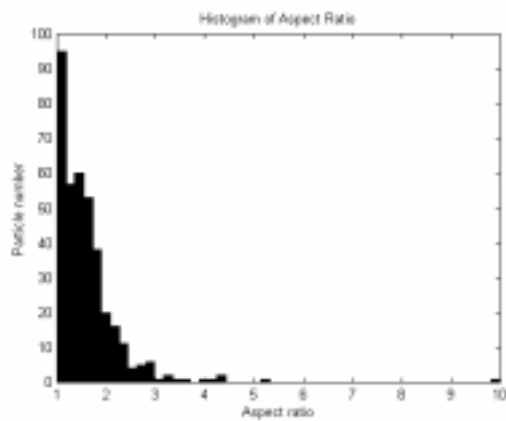


(d) major diameter (m)

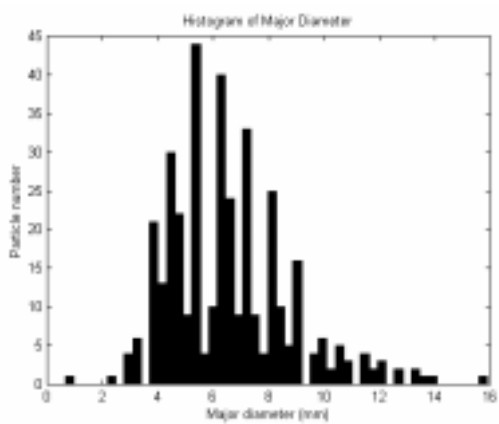
APPENDIX II-1 For Sample Batch #1, Image *a*, 345 particles



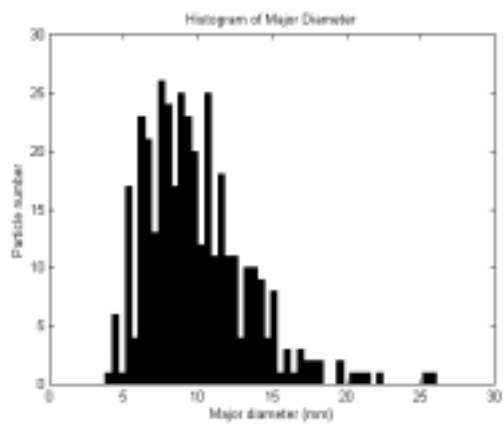
(a) projected area (mm^2)



(b) aspect ratio

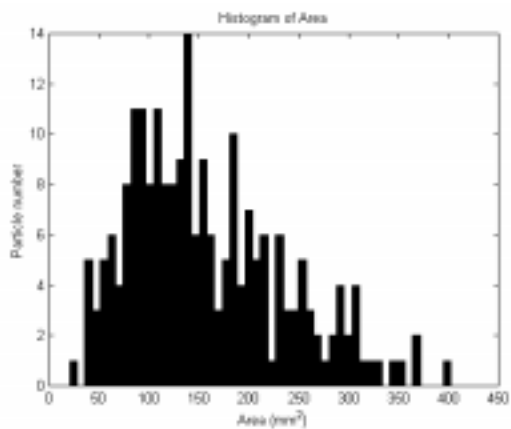


(c) minor diameter (m)

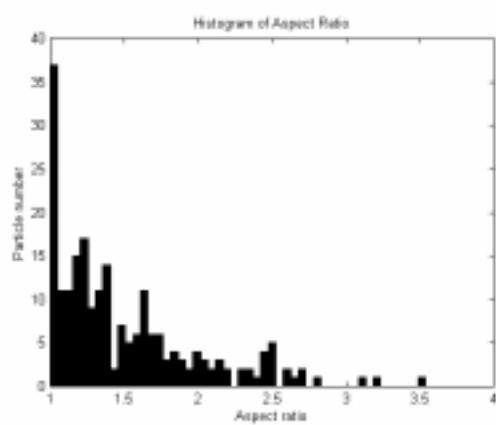


(d) major diameter (m)

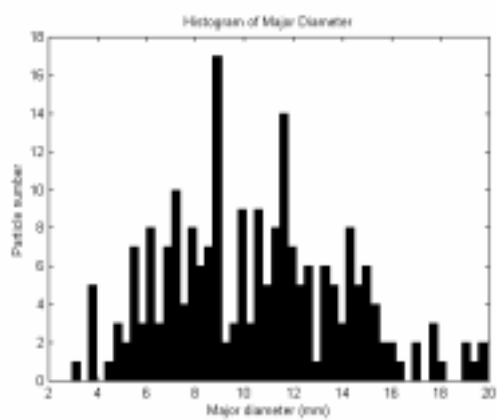
APPENDIX II-2 For Sample Batch #2, Image *a*, 376 particles



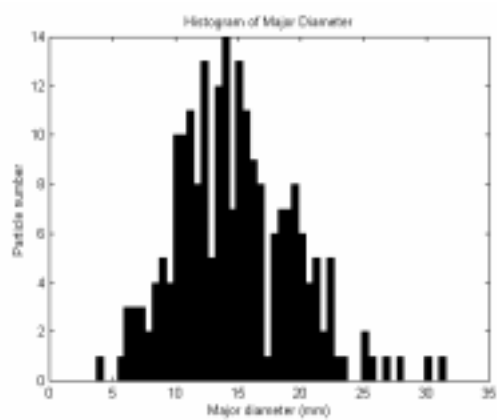
(a) projected area (mm^2)



(b) aspect ratio

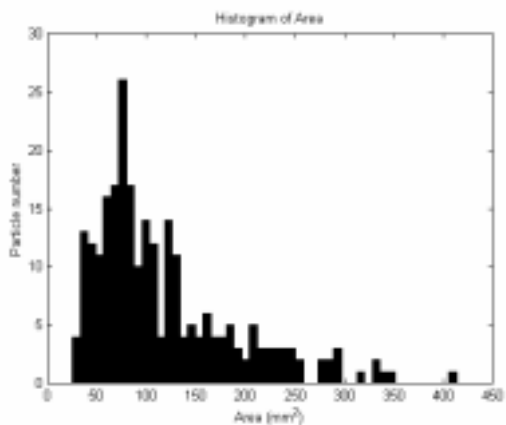


(c) minor diameter (m)

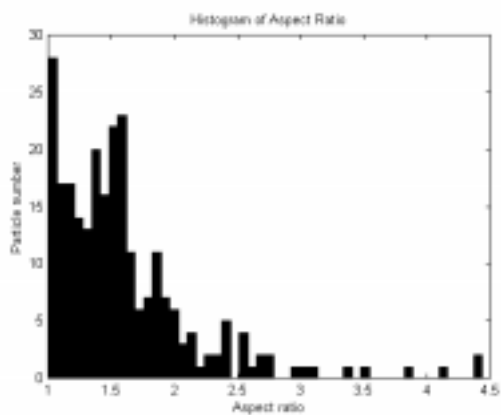


(d) major diameter (m)

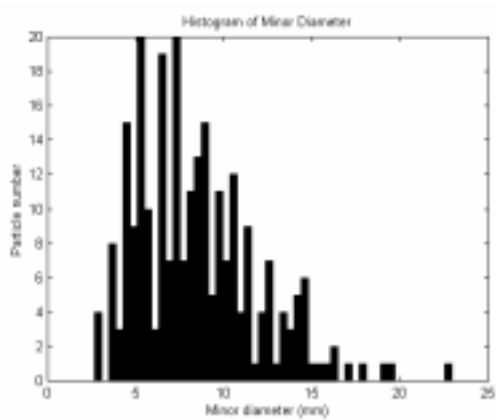
APPENDIX II-3 For Sample Batch #3, Image *a*, 215 particles



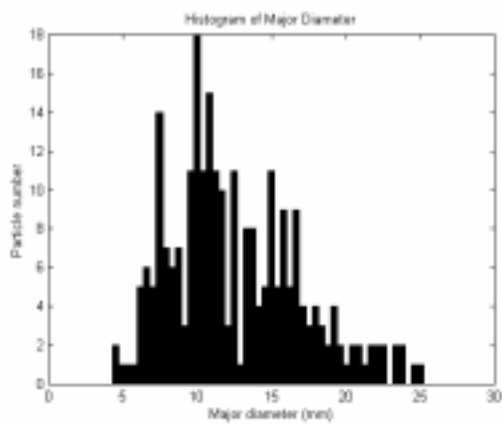
(a) projected area (mm^2)



(b) aspect ratio

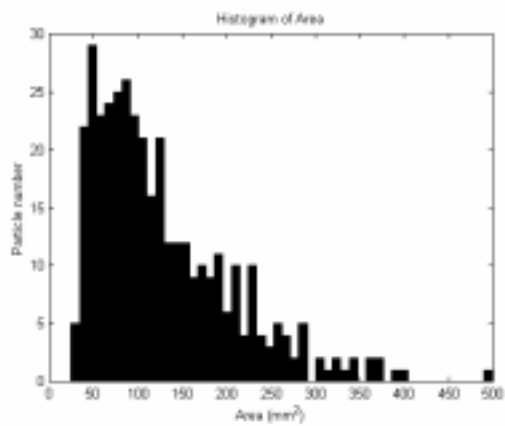


(c) minor diameter (m)

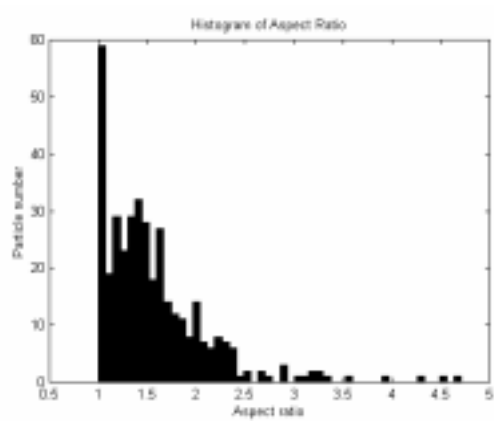


(d) major diameter (m)

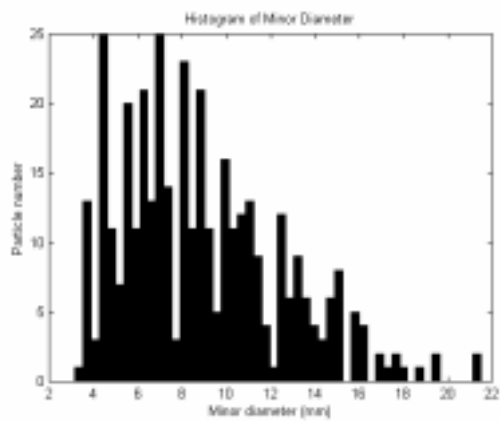
APPENDIX II-4 For Sample Batch #4, Image *a*, 251 particles



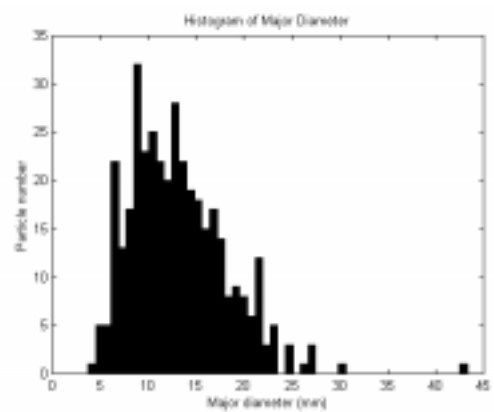
(a) projected area (mm^2)



(b) aspect ratio

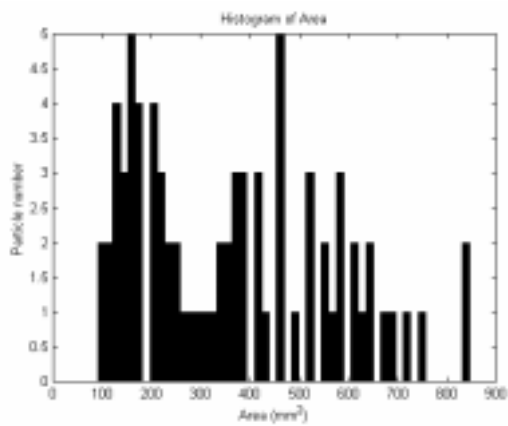


(c) minor diameter (m)

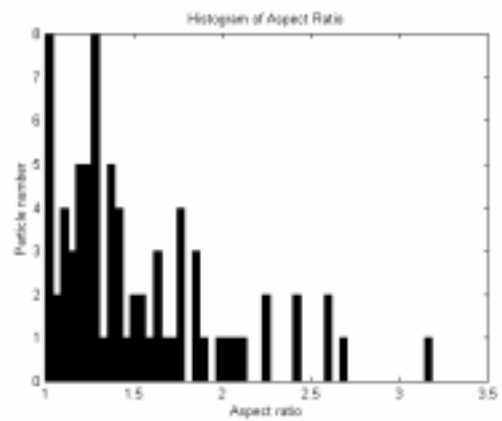


(d) major diameter (m)

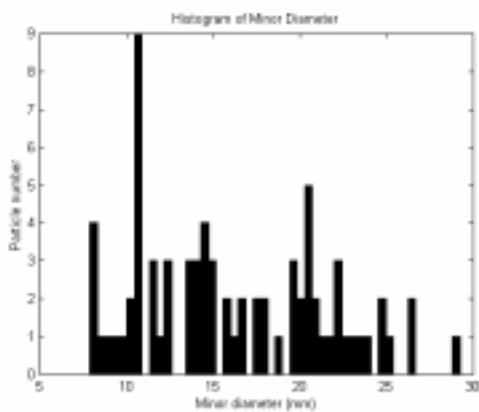
APPENDIX II-5 For Sample Batch #5, Image *a*, 378 particles



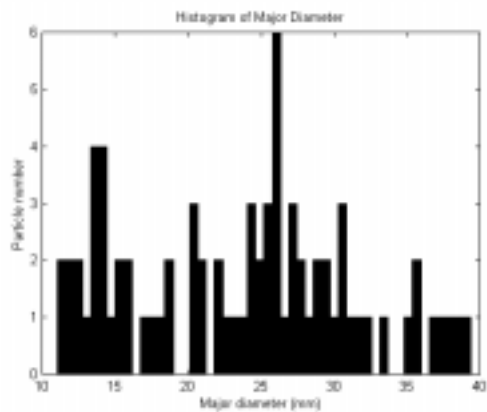
(a) projected area (mm^2)



(b) aspect ratio

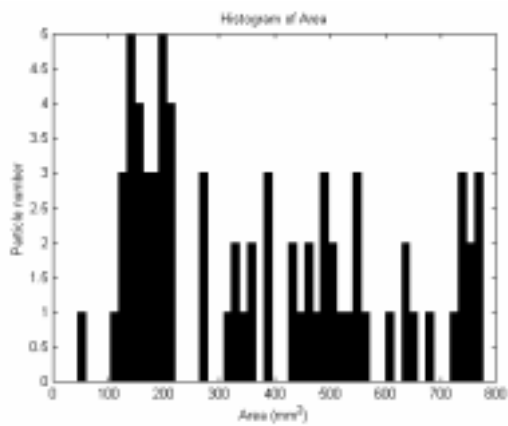


(c) minor diameter (m)

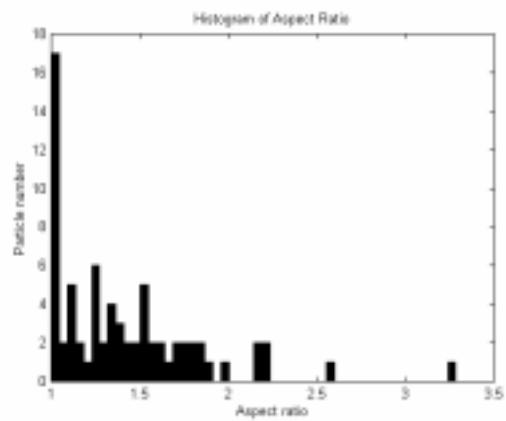


(d) major diameter (m)

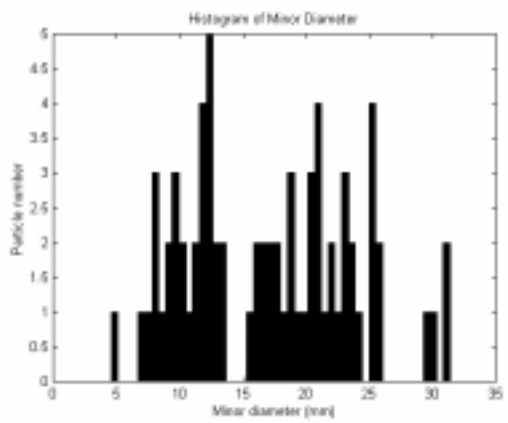
APPENDIX II-6 For Sample Batch #6, Image *a*, 76 particles



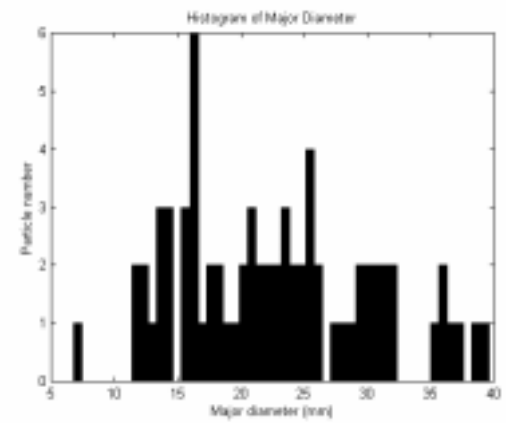
(a) projected area (mm^2)



(b) aspect ratio

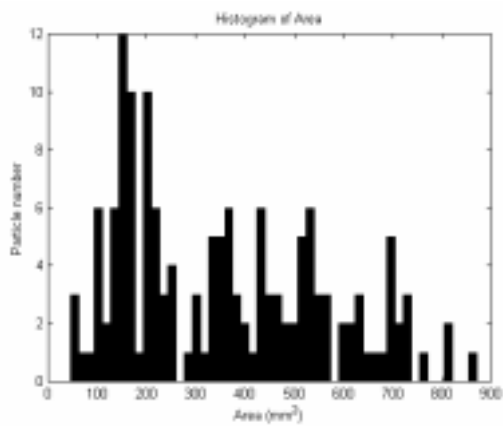


(c) minor diameter (m)

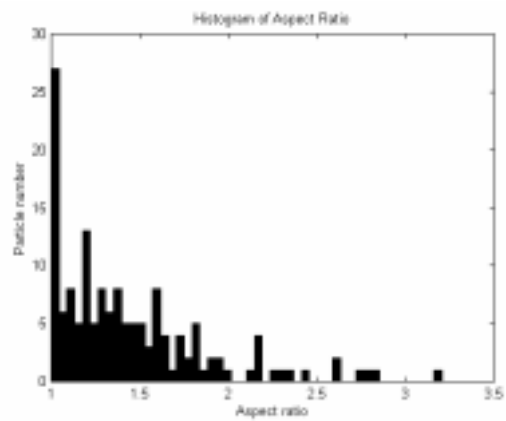


(d) major diameter (m)

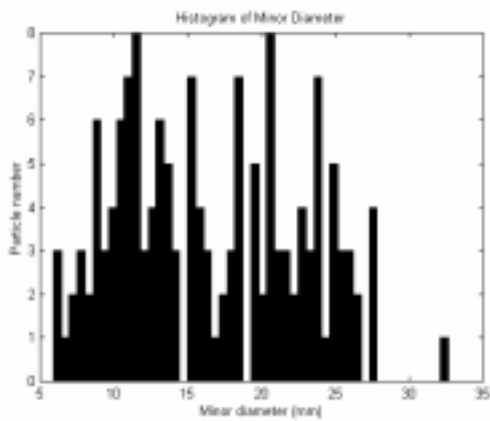
APPENDIX II-7 For Sample Batch #7, Image *a*, 71 particles



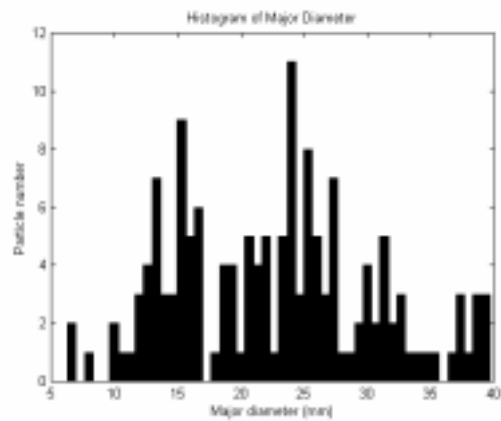
(a) projected area (mm^2)



(b) aspect ratio

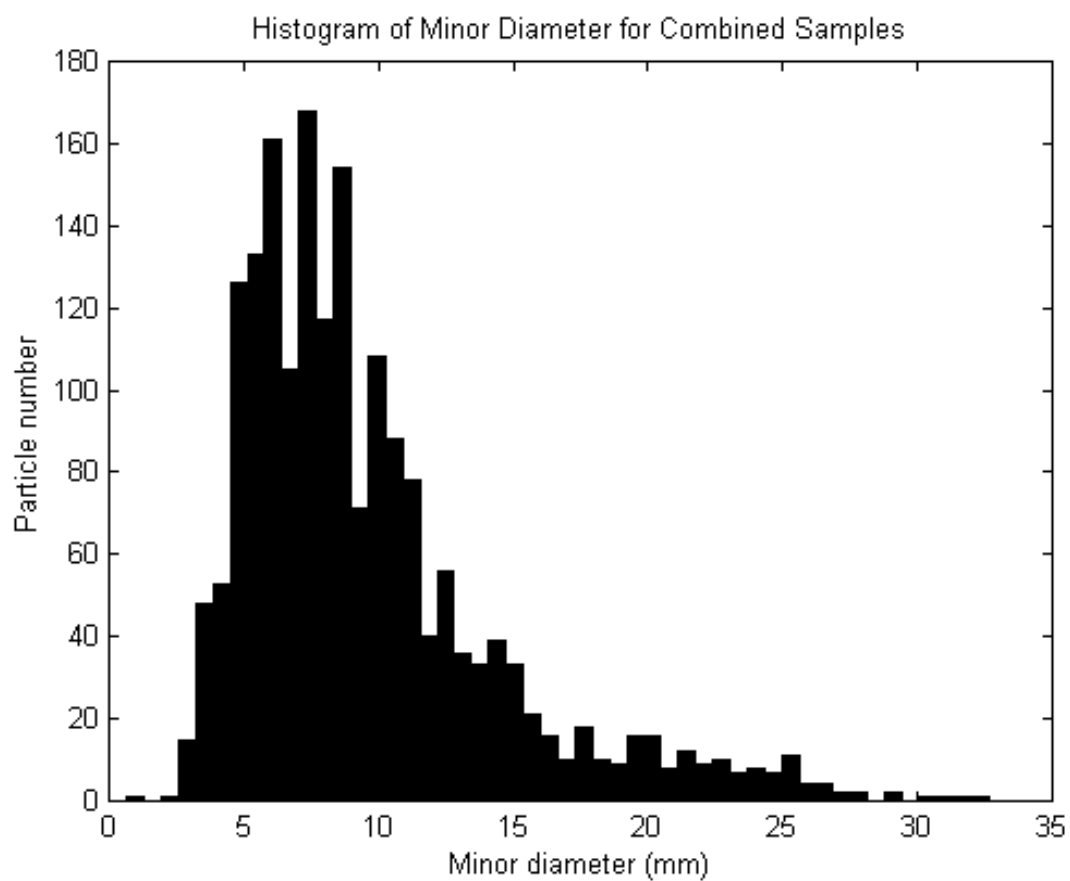


(c) minor diameter (m)



(d) major diameter (m)

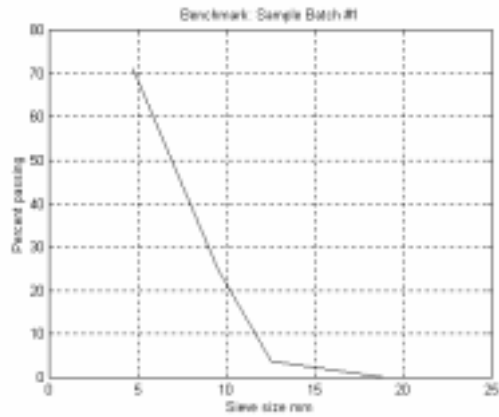
APPENDIX II-8 For Sample Batch #8, Image *a*, 150 particles



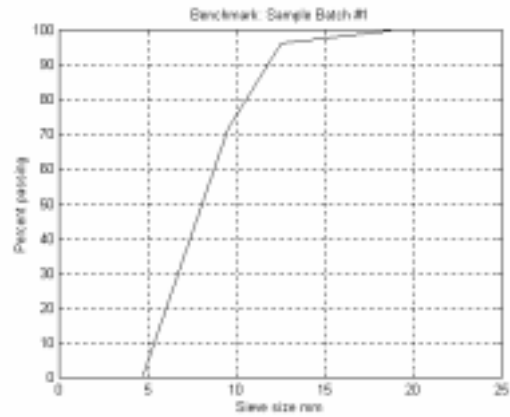
**APPENDIX II-9 Histogram of Minor Diameter For Combined
Sample Batches, Image *a*, 1862 particles**

APPENDIX III

Benchmark of Samples (Total of 8 batches)

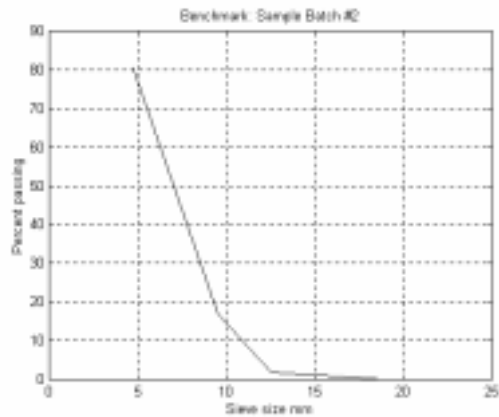


(a) percent retained

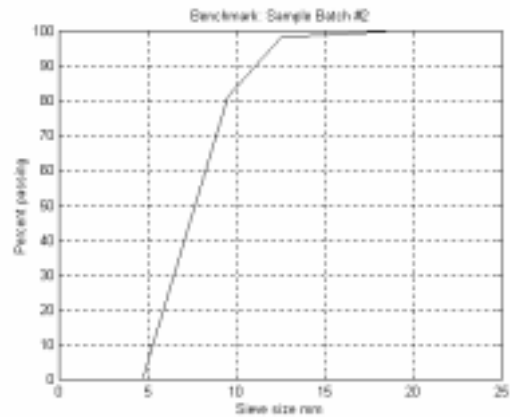


(b) percent passing

APPENDIX III-1 Benchmark for Sample Batch #1

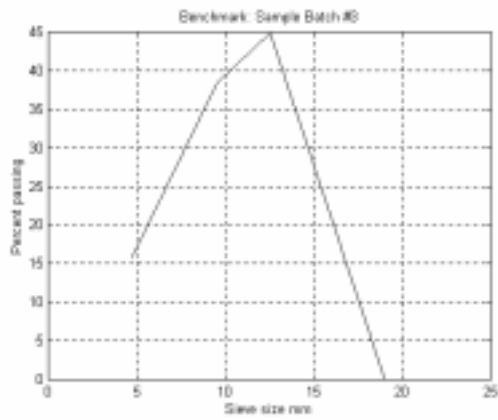


(a) percent retained

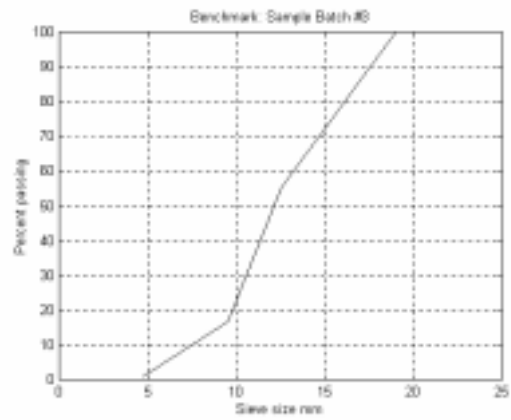


(b) percent passing

APPENDIX III-2 Benchmark for Sample Batch #2

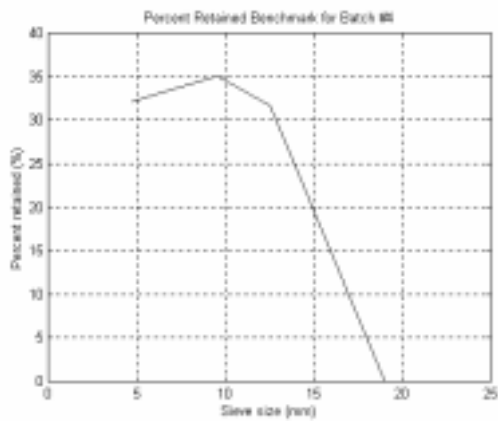


(a) percent retained

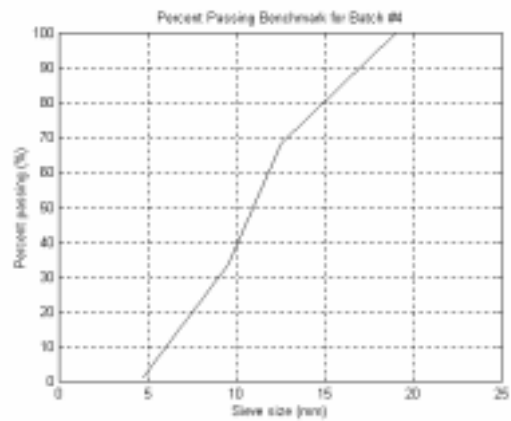


(b) percent passing

APENDIX III-3 Benchmark for Sample Batch #3

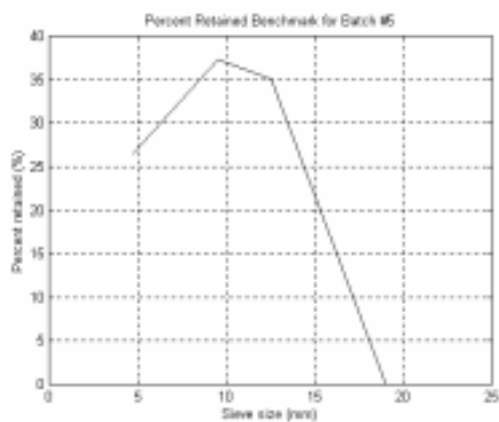


(a) percent retained

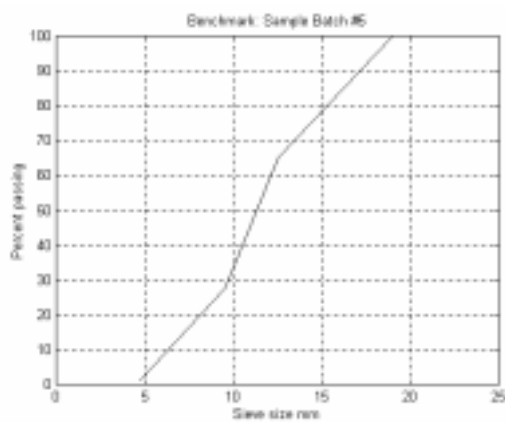


(b) percent passing

APENDIX III-4 Benchmark for Sample Batch #4

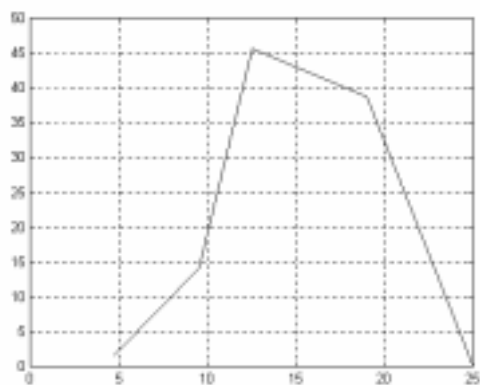


(a) percent retained

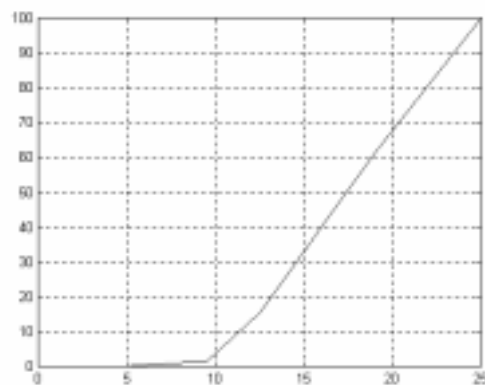


(b) percent passing

APENDIX III-5 Benchmark for Sample Batch #5

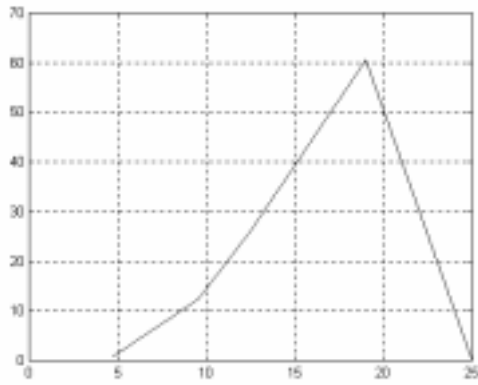


(a) percent retained

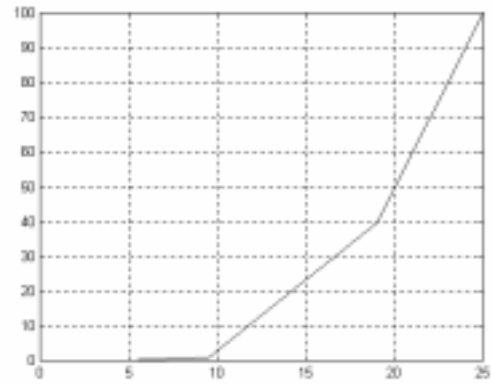


(b) percent passing

APENDIX III-6 Benchmark for Sample Batch #6

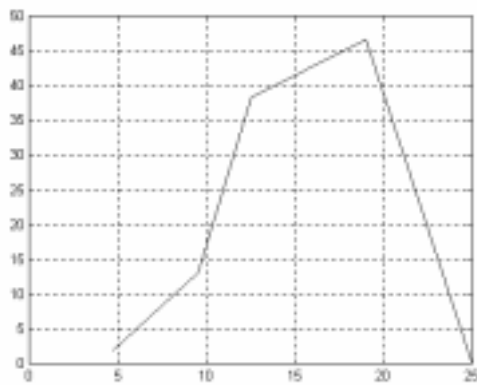


(a) percent retained

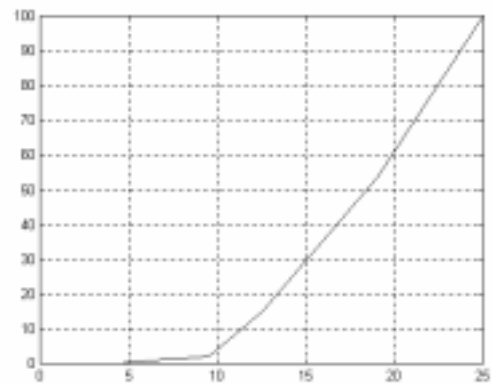


(b) percent passing

APENDIX III-7 Benchmark for Sample Batch #7



(a) percent retained

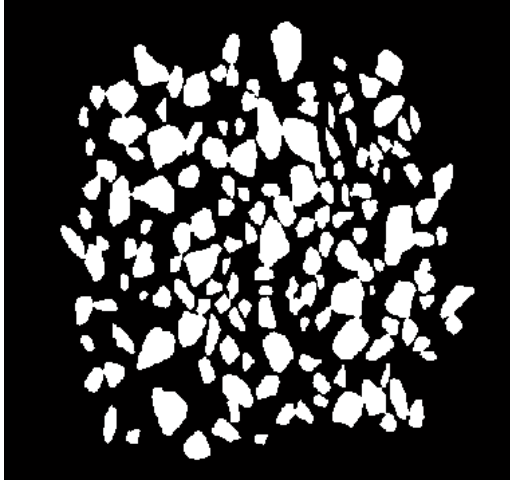


(b) percent passing

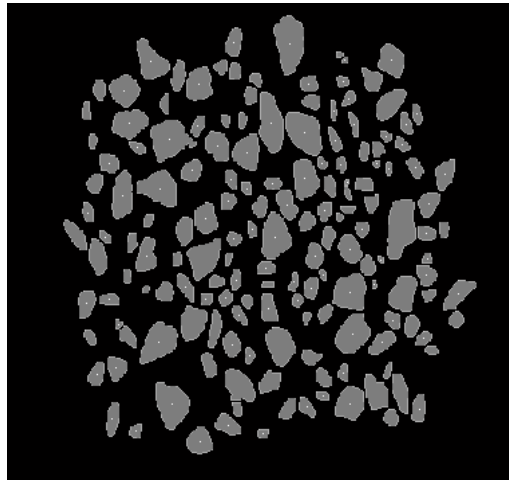
APENDIX III-8 Benchmark for Sample Batch #8

APPENDIX IV

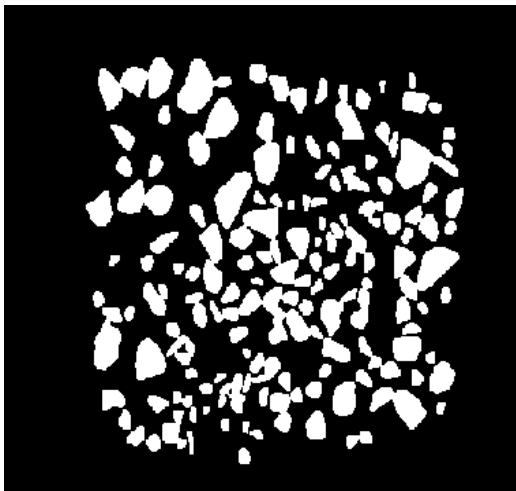
Samples for Testing System Performance (Total of 10 Groups)



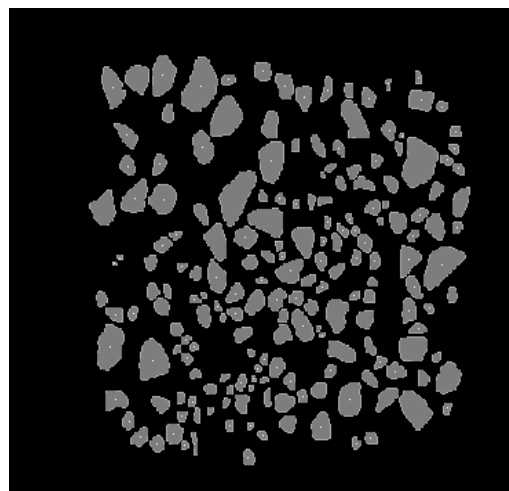
(a-1) group #1



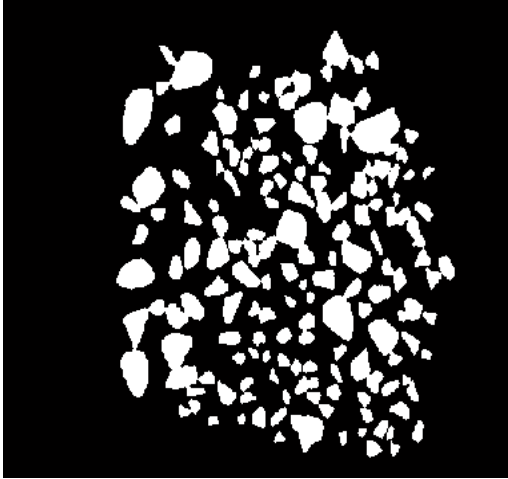
(a-2) processed with $N_I=162$



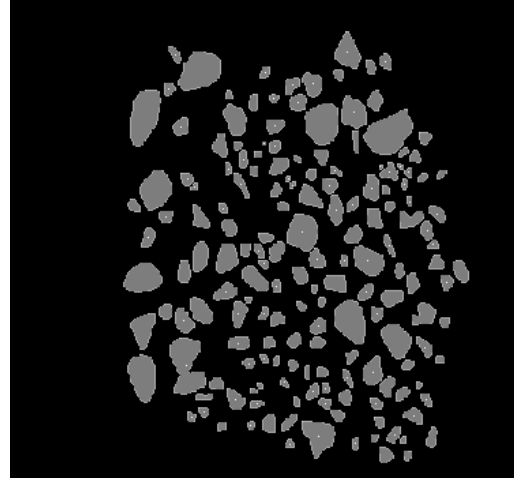
(b-1) group #2



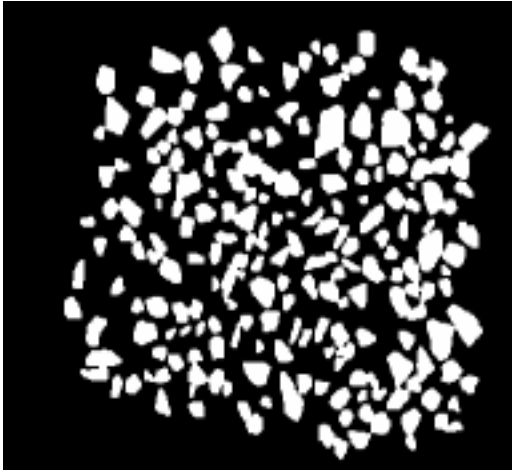
(b-2) processed with $N_2=188$



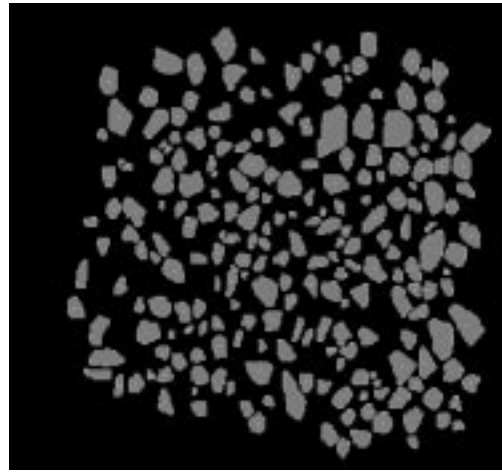
(c-1) group #3



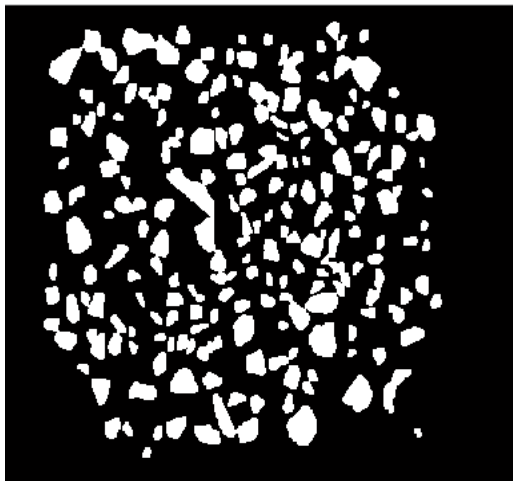
(c-2) processed with $N_3=170$



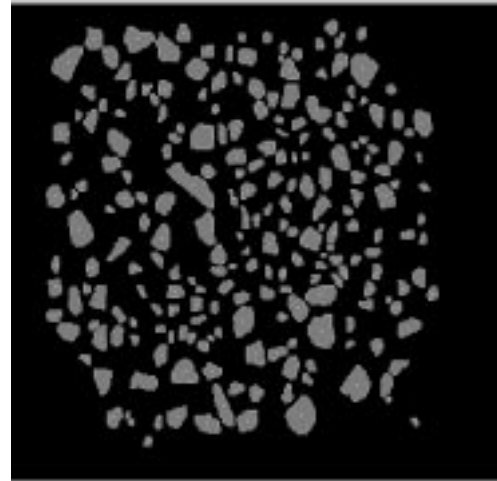
(d-1) group #4



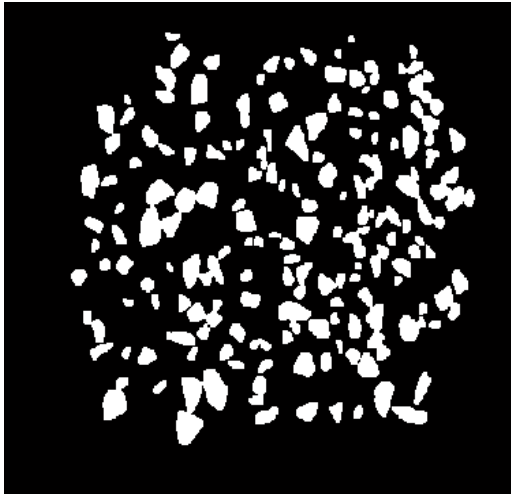
(d-2) processed with $N_4=227$



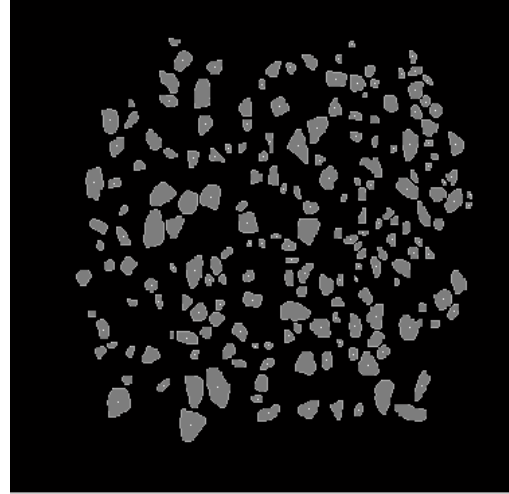
(e-1) group #1



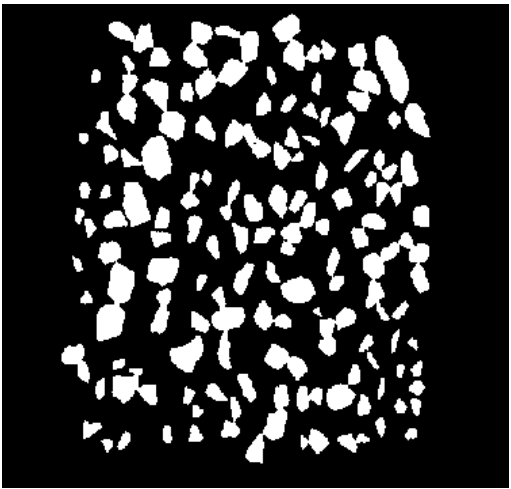
(e-2) processed with $N_5=227$



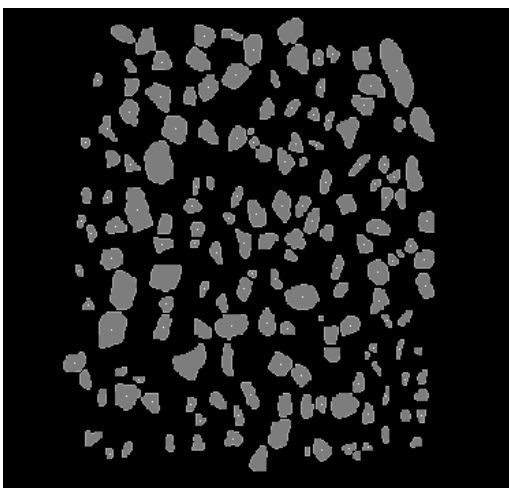
(f-1) group #6



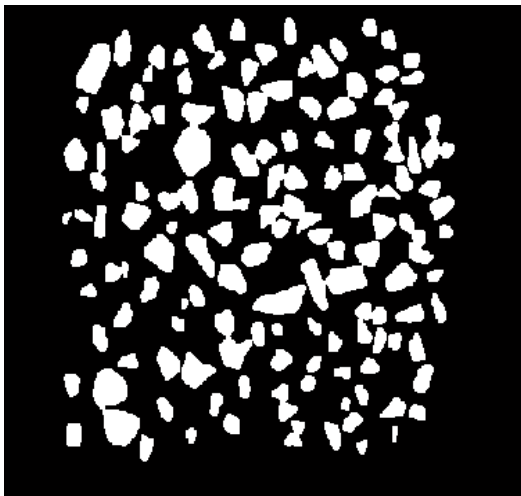
(f-2) processed with $N_6=194$



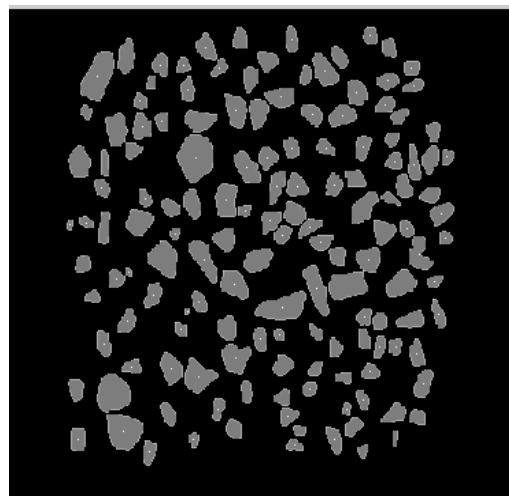
(g-1) group #7



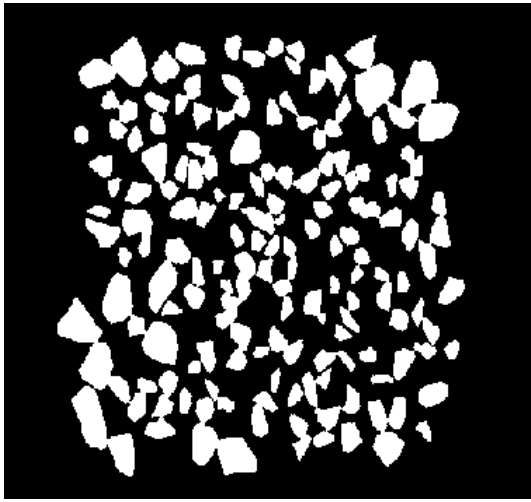
(g-2) processed with $N_7=166$



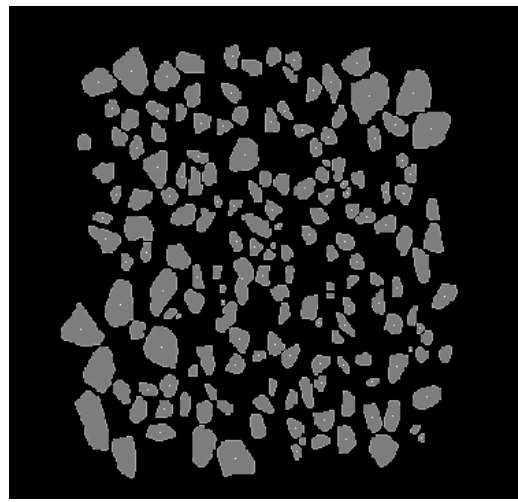
(h-1) group #8



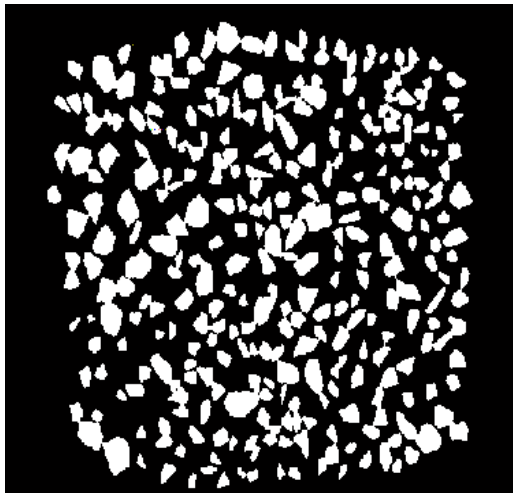
(h-2) processed with $N_8=145$



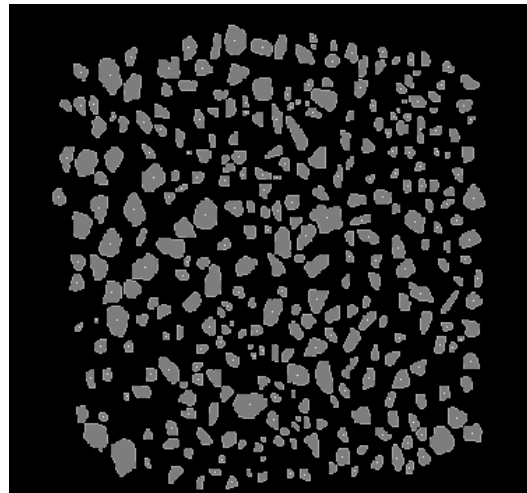
(i-1) group #9



(i-2) processed with $N_0=174$



(j-1) group #10



(j-2) processed with $N_{I0}=321$

VITA

Ken Cheng was born September 12, 1962 in Wuhan, Hubei, P.R. China. He entered Xiangtan University in 1981, where he studied Mechanical Engineering, graduating with a BSME in 1985. He then worked as a production engineer in Chengdu Seamless Steel Tube Manufacturing Company, Sichuan, until March 1992 when he got a chance to travel to Canada.

In western Canada, Ken lived on a farm and attended Canadian Lutheran College where he improved his English skills and earned a Bachelor of Arts degree. In 1994, Ken enrolled in a MSME program at the University of Akron, Ohio and graduated in 1996. From there, he came immediately to West Virginia University to pursue a Ph.D degree in engineering. Upon graduation from WVU, Ken plans to pursue a research or teaching position in automatic controls or machine vision.